High-power, Highly-efficient Thulium-doped Potassium Double Tungstate Channel Waveguide Lasers

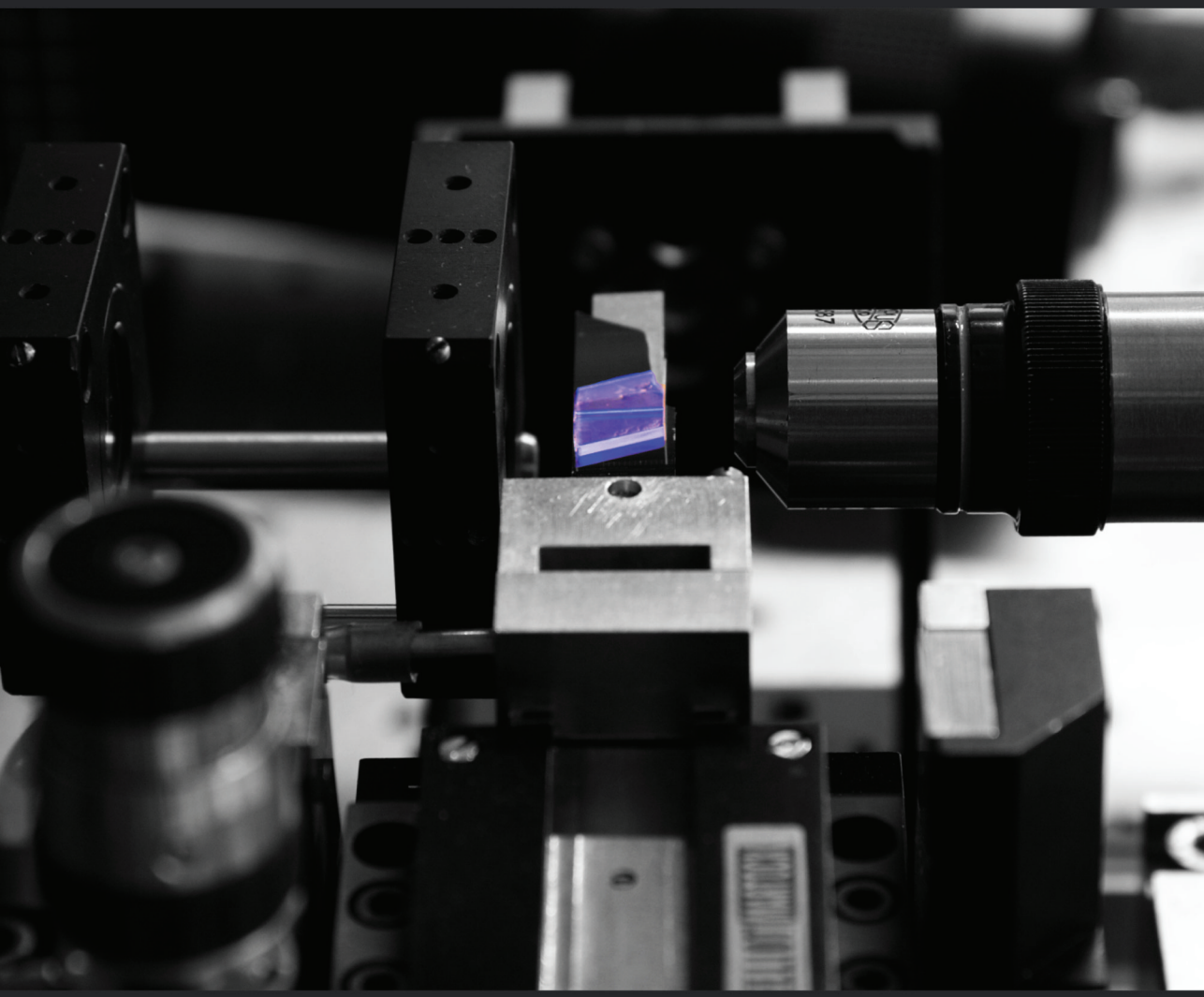

Marko K. van Dalfsen

High-Power, Highly-Efficient Thulium-Doped Potassium Double Tungstate Channel Waveguide Lasers

Koop van Dalfsen

Graduation committee:

Chairman and Secretary:

Prof.dr.ir. J.W.M. Hilgenkamp	University of Twente

Promotors:

Prof.dr. M. Pollnau	University of Twente
Prof.dr. J.L. Herek	University of Twente

Members:

Prof.dr. K.-J. Boller	University of Twente
Dr. S. Manohar	University of Twente
Prof.dr. A.P. Mosk	University of Utrecht
Prof.dr. A. Fiore	Technical University of Eindhoven
Dr. C. Grivas	University of Southampton

The research described in this thesis was performed at the Integrated Optical MicroSystems (IOMS) group, which was a part of:

Faculty of Electrical Engineering, Mathematics and Computer Science
MESA$^+$ Institute for Nanotechnology
University of Twente, P.O. Box 217
7500 AE Enschede, the Netherlands.

This research was financially supported by Agentschap NL of the Dutch Ministry of Economic Affairs under project PD-55.

Front cover: Much time was spent in a blinded optics laboratory. The dark days in the lab were often brightened by the blue fluorescence of excited thulium ions in a channel waveguide.

Printed by: Gildeprint - Enschede

ISBN: 978-94-6233-566-0

High-Power, Highly-Efficient Thulium-Doped Potassium Double Tungstate Channel Waveguide Lasers

DISSERTATION

to obtain
the degree of doctor at the University of Twente,
on the authority of the rector magnificus,
prof.dr. T.T.M. Palstra,
on account of the decision of the graduation committee,
to be publicly defended
on Thursday the 23rd of February 2017 at 16:45h

by

Koop van Dalfsen

born on the 29th of May 1984
in Zwolle, the Netherlands

This dissertation is approved by the promotors:

Prof.dr. M. Pollnau
Prof.dr. J.L. Herek

Contents

1 Introduction **1**
- 1.1 Integrated optics and micro-lasers . . . 1
- 1.2 Integrated optics on potassium double tungstates . . . 3
- 1.3 State-of-the-art in 2-µm rare-earth lasers . . . 6
- 1.4 Applications of 2-µm lasers . . . 7
- 1.5 The human trace gas sensing project . . . 9
- 1.6 Overview of this thesis . . . 10

2 Waveguide design and fabrication **11**
- 2.1 Crystal properties . . . 11
- 2.2 Liquid-phase epitaxy of monoclinic double tungstates . . . 19
- 2.3 Waveguide design . . . 27
- 2.4 Waveguide micro-structuring . . . 31

3 Theoretical analysis **39**
- 3.1 Interaction between light and rare-earth-doped media . . . 39
- 3.2 Rare-earth lasers . . . 50

4 Highly efficient lasers **61**
- 4.1 Efficient lasers in low-loss buried channel waveguides . . . 61
- 4.2 Laser efficiencies - toward the theoretical limit . . . 71
- 4.3 Tunable lasers via an extended cavity in Littrow configuration . . . 93

5 Summary and Outlook **97**
- 5.1 Summary . . . 97
- 5.2 Outlook . . . 99

Abstract **101**

Nederlandse samenvatting **103**

Bibliography **105**

List of publications **115**

Dankwoord **122**

Voor mijn vrouw Esther en onze kinderen

List of symbols

Symbol	Units	Description
ρ	J s m^{-3}	radiation density
ν	s^{-1}	optical frequency
λ	m	wavelength
n	–	refractive index of an optical medium
h	J s	Planck's constant
c	m s^{-1}	speed of light in vacuum
k_B	J K^{-1}	Boltzmann's constant
T	K	temperature
E	J	energy
g	–	degeneracy of a Stark level
N	m^{-3}	population density
N_T	m^{-3}	total dopant concentration
B	m^3 J^{-1} s^{-2}	Einstein coefficient
B_{al}	–	ratio of reabsorption loss over total cavity loss
A	s^{-1}	decay rate constant
A_{cr}	cm^2	active medium cross-section
τ	s	level lifetime
τ_c	s	resonator photon lifetime
I	J s^{-1} m^{-2}	irradiance
α	m^{-1}	optical absorption coefficient
f_i	–	Stark level population fraction of the total manifold population
σ	m^{-2}	atomic cross-section
$\sigma_{\mathrm{a,eff}}$	m^{-2}	effective absorption cross-section
$\sigma_{\mathrm{e,eff}}$	m^{-2}	effective emission cross-section
η_p	–	pump absorption efficiency
η_s	–	laser slope efficiency
η_q	–	pump quantum efficiency
η_{St}	–	Stokes efficiency
η_t	–	transversal efficiency
η_{out}	–	out-coupling efficiency
β	–	branching ratio

ω	rad s^{-1}	relaxation-oscillation frequency
ν_{ph}	s^{-1}	phonon frequency
r_p	m^{-3}	distribution function for the pump energy
ϕ_0	m^{-3}	distribution function for the laser energy
w_l	m	laser beam radius
w_p	m	pump beam radius
W_{CR}	cm^3 s^{-1}	cross-relaxation rate parameter
W_{ETU}	cm^3 s^{-1}	energy-transfer up-conversion rate parameter
R_p	m^3 s^{-1}	pump rate
Φ	–	photon number (in a resonator)
V	m^3	mode volume in a resonator
V_a	m^3	mode volume in active medium
l_{opt}	m	single-pass optical length of a resonator
l_{res}	m	physical length of a resonator
l_{cr}	m	physical length of an active medium
δ	–	logarithmic cavity round-trip loss
δ_{out}	–	logarithmic out-coupling coefficient
R	–	mirror reflectivity
T_{out}	–	out-coupling transmission
L	–	intrinsic roundtrip loss of a resonator
f_σ	–	absorption over emission ratio
P_P	W	pump power
$P_{\mathrm{thr.}}$	W	threshold pump power
P_{out}	W	laser output power

CHAPTER 1

Introduction

1.1 Integrated optics and micro-lasers

In 1959, Richard Feynman delivered a famous outlook on the shrinkage of devices toward their physical limits, and ultimately down to the atomic level [1]. His talk sparked the interest of many, whose interest was further stimulated by his offering of prizes of $1000 to the first scientist to shrink the page of a book by 1/25000 or the first engineer to create a 1/64 inch rotary motor. Whether it was this talk that initiated the field of micro- and nanotechnology or not, nowadays it is hard to find products that do not in some way rely on nano- and microtechnology. Perhaps the best example is the abundance of electrical chips in almost any every-day device; no such an electrical chip could have existed without micro- and nanotechnology.

The advances in the electrical chips are apparent because of our ever-increasing use of devices that rely on these chips. However, a less apparent, but similar development as in electrical chips is ongoing in the world of optical and electro-optical chips: the field of integrated optics. This field has opened up new possibilities that electronic chips and circuits are not (easily) capable of. Examples are high-speed long-haul telecommunication lines (fibres), or quantum cryptography by exploiting a small number of photons [2]. The coupling of electronic and optical circuits allows a best-of-both-worlds approach [3, 4].

The counterpart to metallic lines in electrical circuits is the waveguide on optical chips. In such a waveguide, light is confined within a layer of high refractive index contrast with its surroundings, and guided via the principle of total internal reflection. Confinement of light in a planar core between two planar claddings yields a planar waveguide, whereas fibre waveguides consist (predominantly) of a circular core surrounded by a cladding, yielding a cylindrical geometry. Many different channel waveguide geometries are known, but in this thesis buried, ridge-type channel waveguides are used. The coupling of light into and out of channel waveguides can prove challenging, but several tricks such as adiabatic tapering of waveguides, using ultra-high-numerical aperture in- and out-coupling fibres or fabrication of on-chip lenses [5], can mitigate this problem.

Optical waveguides are small structures which allow the guiding of optical energy in the form of an optical mode. The dimensions of such a waveguide are tai-

lored to the optical wavelength of interest and can be integrated on optical chips with further functionality such as gain enhancement and sensing principles. The ongoing enhancement of fabrication techniques allows for better quality structures which reduces the amount of defects and, consequently, less optical mode distortion [6, 7].

Optical waveguides can be combined on-chip with various other active and passive components in order to create integrated on-chip sensors, tuneable lasers and filters, for example. In the Integrated Optics and MicroSystems (IOMS) group at the University of Twente, a great variety of passive and active optical chips have been realised. Active chips, such as high-bit-rate amplifiers and tunable ring-lasers in the telecom C-band, based on Al_2O_3:Er^{3+} [8–10] and amplifiers on Al_2O_3:Nd^{3+} [11], as well as efficient, narrow-linewidth Bragg-grating-based lasers and sensors on Er^{3+}- and Yb^{3+}-doped Al_2O_3 [12–14] have been realised. The first continuous-wave polymer laser has also been demonstrated [15, 16]. As passive optical chips and sensors, opto-fluidic chips were realised that combine micro-fluidic channels with femto-second-written optical waveguides on a glass substrate, for the purpose of on-chip DNA analysis [17, 18]. Sensors exploiting arrayed-waveguide gratings were used to provide applications in on-chip optical coherence tomography [19], and Raman spectroscopy [20].

Waveguides can be made active by doping these with rare-earth ions to create amplifiers and lasers. The strongly reduced form-factor of integrated, waveguide lasers compared to bulk lasers has several additional benefits: the high overlap between pump and oscillating laser beams, combined with a high intensity allows for high population inversion densities and high out-coupling efficiency, yielding highly efficient lasers. Besides, these high intensities and population inversion densities are typically reached for pump thresholds on the order of milliwatts. Micro-lasers on dielectric, amorphous Al_2O_3, with Bragg-grating-based integrated reflectors were realised in Al_2O_3:Yb^{3+} with a maximum of 47 mW (10 mW) of output (threshold) power and a slope efficiency of 67% [21] and up to 75 mW in Al_2O_3:Er^{3+} [22]. The strong intensities and confinement in channel waveguides can even be exploited for the realisation of on-chip super-continuum light sources, realised on extremely low-loss Si_3N_4 (TriPleX) [23, 24]. Integrated optics can even improve line-width and tunability of existing lasers, for example by using ring-resonator cavities [25].

The laser host material and geometry partly determines the output performance of the laser, for example via its properties such as absorption and emission coefficients, level lifetimes, ability to dissipate heat and the ease with which the material can be modified, by for example etching. In geometries such as fibres, made from materials with low absorption cross-sections (and a low dopant concentration), for example, a lot of length is required to build-up sufficient gain. However, as a result of the long length and surface area, heat is dissipated easier and high powers can be obtained. In crystals with higher absorption

cross-sections on the other hand, much shorter lengths are required for the same amount of gain, but as a consequence must be cooled in order to prevent fracture at higher output levels. In rare-earth-ion-doped crystals, impurity ions are located at well-defined positions inside a lattice, resulting in very defined crystal field strengths, strong wavelength-selective gain, and relatively weak ion-ion interaction due to their larger separation distance. In amorphous hosts on the other hand, clustering of impurity ions significantly affects the available gain, even to the point where significant fractions of ions are strongly quenched [26]. Typically, the transition probability in crystals is a bit lower than in glasses, but this can be compensated by a higher dopant concentration. The highest efficiency and output powers are oftentimes reported for crystal materials. For example, record-high slope efficiencies of over 92% (optical-optical) were reported recently in a resonantly-pumped YAG:Er^{3+} planar waveguide laser [27]. Also in this work, a crystalline laser host material will be employed for the realisation of very efficient, powerful, and compact lasers.

1.2 Integrated optics on potassium double tungstates

1.2.1 Merits of the potassium double tungstate crystals

The potassium double tungstate crystals form the basis of the research presented in this thesis, since they are widely recognised as very promising materials for a variety of laser types and operating regimes. Table 1.1 shows a comparison of potassium double tungstate versus popular laser host materials such as YAG and YLF. The high potential of the rare-earth-ion-doped potassium double tungstate crystals is partly due to it exhibiting among the highest absorption and emission cross-sections compared to other host materials. The absorption cross-section of Yb^{3+}, for example, in potassium double tungstate crystals is approximately 15 times larger than in YAG, while its quantum defect is the lowest among many host materials [32]. In addition, the relatively large ion-ion separation distance in tungstate materials allows very high dopant concentrations without significant quenching effects which adversely affects the gain performance in many cases [33]. The combination of these factors allows very compact lasers resulting from the short absorption length and therefore short heat dissipation lengths and low overall heat generation. In this way, very efficient ytterbium thin-disk lasers have been demonstrated [34], despite the fact that the thermal conductivity of potassium double tungstate is four times lower than YAG [28]. More recently, the high absorption and emission was further highlighted with the demonstration of over 1000 dB/cm of gain in Yb^{3+}-doped amplifiers [35, 36]. Another interesting feature of the potassium double tungstates is simulated Raman scattering, which

Table 1.1 Comparison of properties of potassium double tungstate (K[RE]W), YAG, and YLF crystals. These host materials (an many other not shown in this table) support co-doping with thulium for the realisation of 2 µm lasers. In potassium double tungstate host materials, [RE] can mean Y, Gd, Lu, for example, or a combination of these. Optical properties are specified for thulium in the different host materials at the optical wavelength range of interest: $0.8-2$ µm, and the absorption cross-sections of Tm^{3+} between the ground level and the $^3H_6$ level around 800 nm.

Parameter	K[RE]W	YAG	YLF	Ref.
Chemical formula	$K[RE](WO_4)_2$	$Y_3Al_5O_{12}$	$YLiF_4$	
Crystal structure	monoclinic	cubic	tetragonal	
Mass density [g/cm^3]	6.5	4.5	4	
Moh's hardness	$4-5$	$8-8.5$	$4-5$	
Thermal conductivity [W/m K]	3	$10-14$	6	[28]
Melting point [°C]	1070	1970	819	
Doping concentration (1at.%) [10^{20} cm^{-3}]	0.63	1.36	1.40	
Birefringence	biaxial	-	uniaxial	
Transparency window [µm]	$0.34-5$	$0.24-5$	$0.18-6.7$	[29]
Refractive index	2	1.8	1.46	
Abs. cross-section at 800 nm [10^{-20} cm^2]	< 10	< 0.8	< 0.8	[30]
Fluorescence lifetime ($^3F_4$) [ms]	$1-1.5$	$8-12$	$9-15$	[30]
dn/dT [10^{-6} K^{-1}]	±-10	$7-10$	3	[29, 31]

allows the use of these crystals as frequency converters [37, 38].

For bulk lasers, the monoclinic potassium double tungstate crystals have been used to demonstrate thulium lasers operating close to 2 µm [39, 40] with slope efficiencies up to 69%, and thulium-holmium co-doped lasers operating well beyond 2 µm, in continuous-wave (cw) and passive mode-locked operating mode [41]. For ytterbium, lasing has been achieved in the stoichiometric $KYb(WO_4)_2$ crystal, with up to 44% of slope efficiency [42].

1.2.2 On-chip integrated devices on potassium double tungstates

Integrated devices rely for their operation on the refractive index contrast between a core (guiding) layer and the surrounding layers, such as the substrate and a cladding layer. In the case of potassium double tungstates, the addition of rare-earth ions increases the refractive index of the doped material, by replacing (part of) the Y^{3+} ions in the lattice. For example, refractive index changes on the order of 10^{-4} have been demonstrated in Yb-doped tungstate for typical dopant concentrations on the order of a few percent, which has lead to the demonstration of a planar waveguide laser in an external cavity with an output power of 290 mW and a slope efficiency of 80% [43], and more recently to a record slope efficiency of over 82% in a crystal with attached butt-coupled mirrors [44].

Epitaxial growth and the demonstration of planar waveguide lasers is the first step toward monolithic integration of lasers in these crystals. Whereas one-dimensional confinement is realised in planar waveguides, yielding strong elliptical mode shapes, two-dimensional lateral confinement can be realised in channel waveguides. The optical beam quality and intensity obtained from these channel waveguides is superior to that of planar waveguides. The first channel waveguides in potassium double tungstate were fabricated by femtosecond laser irradiation, but the propagation losses at 1 µm were rather high at $2 - 2.5$ dB/cm, and the optical confinement was weak compared to micro-structured ridge channel waveguides [45]. The first Yb channel waveguide laser was demonstrated by strip-loading a fibre with index-matching fluid [46], but the lateral confinement was rather poor. The first real monolithic waveguide laser in Yb-doped tungstate was demonstrated by Bain in femtosecond-laser-irradiation-written channel waveguides, but the performance was rather poor with an output power of 18.6 mW, and a slope efficiency of 13.8 % owing to the high propagation loss of 1.9 dB/cm [47].

A key development for the realisation of monolithic waveguide lasers in tungstate was the co-doping of Gd^{3+} and Lu^{3+} together with optically active ions [48]. One huge benefit is a strong reduction of the lattice mismatch, which allows a much higher dopant concentration of optically active ions, up to over 50at.% in case of Yb^{3+} [35]. The second benefit is the strong increase of the refractive index contrast by two orders of magnitude (from 10^{-4} [43] in case of no co-doping with Gd^{3+} and Lu^{3+}, to 10^{-2} in case of high co-doping with Gd^{3+} and Lu^{3+} [35]), which allows a much more compact channel waveguide cross-section and optical mode size [44].

The micro-structuring by Geskus and overgrowth by Aravazhi of channel waveguides was a next major step toward high-performance monolithic waveguide lasers, and has lead to the demonstration of Yb-doped channel waveguide lasers up to 76% of slope efficiency, hundreds of milliwatts of output power and low

thresholds [49–52]. This technique, which will be discussed in detail in chapter 2, uses argon-beam etching of the active layer for the definition of the channels. A variant to this technique employs etching of the substrate followed by overgrowth of the active layer onto the substrate, yielding triangular-shaped buried channels [53].

1.3 State-of-the-art in 2-µm rare-earth lasers

Though the potassium double tungstate material was first described by Borisov and Klevtsova in 1968 [54], it took until 1997 for the first demonstration of a erbium/ytterbium-sensitized thulium laser operated near 2 µm in this material, using a Xe flash lamp under cryogenic conditions [55]. Later, several bulk lasers operated in cw-mode were demonstrated in Ti:Sapphire-laser-pumped thulium-doped $KY(WO_4)_2$ [56], and in the same material, pumped with a diode laser [57]. In 2004, $KGd(WO_4)_2$ [58], and in 2006, $KLu(WO_4)_2$ [40] thulium bulk lasers were demonstrated, the latter of which had a maximum slope efficiency of 69% and an output power of 4 Watt. High slope efficiency up to 68% and output powers in the hundreds of Watts have also been generated in thulium-doped fibre lasers [59], or with lower power but the highest reported efficiency of 74% in another thulium-doped fibre laser [60]. In a holmium-doped fibre laser, resonantly pumped with a thulium laser, up to 6 Watts of output power and a slope efficiency of 80% was demonstrated at 2 µm [61]. With the ever-increasing quality of laser host materials, very high slope efficiency up to 65% and output powers of several Watts have also been generated in ceramic YAG:Tm lasers [62].

Very recently, compact, efficient and powerful microchip lasers in potassium double tungstates have been demonstrated with 71% of slope efficiency and Watt-level output power from a thulium-doped $KLu(WO_4)_2$ microchip laser [63, 64]. Such a thulium-doped microchip laser was subsequently used for in-band pumping of a holmium-doped $KLu(WO_4)_2$ microchip laser [65], yielding a slope efficiency of 84% for the holmium laser (45% optical-to-optical) and hundreds of milliwatts of output power. These microchip lasers are compact because of butt-coupling of planar mirrors to a bulk chip, eliminating the need for an external cavity.

Presently, much effort is made towards pulsed lasers. Recently demonstrated diode-pumped micro-chip lasers in thulium-doped $KLu(WO_4)_2$ operating at 2.1 µm are coupled with single-walled carbon-nanotube-based saturable absorbers to demonstrate a Q-switched laser with a power output of 0.7 W, with a slope efficiency of 29%, or in continuous-wave mode 1.17 W and 39% of slope efficiency [66]. Alternatively, a diode-pumped, thulium-doped $KY(WO_4)_2$ microchip laser is coupled with an InGaAs semiconductor saturable absorber to obtain pulses at a repetition rate of 1.2 MHz and an average output power of 130 mW at 1.9 µm. In continuous-wave mode, the output power of this laser reaches 2.6 W, with a

slope efficiency of 74% versus absorbed pump power [67].

The first dielectric planar waveguide laser operating at 2 µm was demonstrated in 1994 in a thulium-doped lead-germanate glass [68]. The first planar thulium waveguide laser in a potassium double tungstate material was demonstrated by Rivier in 2007, which delivered 32 mW of output power and up to 13% of slope efficiency [69]. Thulium-doped YAG planar waveguide lasers achieved very high slope efficiency of up to 68% [70], and output powers of over 10 W in a diode-side-pumped YAG laser [71]. Recently, 560 mW of output power and very high slope efficiency up to 76% has been demonstrated in a YLF:Tm planar waveguide laser [72].

Since planar waveguide lasers provide confinement only along one axis, the output beam is usually of elliptical shape and the intensities are lower than in channel waveguide lasers (by at least an order of magnitude, assuming that the lateral beam size is at least 10 times smaller in channel waveguides than in planar waveguides, for identical amounts of launched pump power). Channel waveguide lasers benefit from an enhanced overlap between pump and laser modes, for end-pumped configurations. Thulium-doped channel waveguide lasers operating at 2 µm have been demonstrated in Zn-in-diffused oxide materials [73], ion-exchanged glass channel waveguides [74], as well as in femtosecond-written channels in glass materials with slope efficiencies up to 67% [75]. Buried channel waveguide lasers in a co-doped potassium double tungstate host with butt-coupled mirrors yielded slope efficiencies of up to 13% and several milliwatts of output power [53].

In this work the realisation is reported of buried, channel waveguide lasers in a co-doped potassium double tungstate host with an efficiency of 81% and watt-level output powers at 2 µm. To the best of our knowledge, this is the most efficient 2-µm channel waveguide laser to date, which produces very respectable output power and benefits from a very low threshold.

1.4 Applications of 2-µm lasers

Thulium lasers operating near 2 µm are used for the optical pumping of holmium lasers, that also emit near 2 µm, but at a slightly longer wavelength. The emission of thulium and holmium combined spans an optical bandwidth between $1.7 - 2.2$ µm [76]. Thulium can conveniently be pumped at 800 nm using diode lasers, but holmium is lacking an atomic transition at this wavelength. Holmium can be resonantly pumped by the thulium emission at 2 µm, either intra-cavity or with separate resonators for the thulium and holmium gain media. Alternatively, co-doping of holmium and thulium into one gain medium facilitates energy-transfer from thulium to holmium and allows pumping at 800 nm. The latter approach allows for a more compact system, but the efficiency of such a system is not as high as the combination of separate thulium and holmium lasers due to a

combination of detrimental up-conversion processes that are not contributing to the holmium laser gain [77].

The spectral region in which the thulium (and holmium) lasers operate is called the 'eye-safe' spectral region. This is because the absorption spectrum of water increases by orders of magnitude from the visible region until its peak value between $2 - 3$ µm. The penetration depth of optical radiation at 2 µm in biological tissue, of which the main constituent is water, is therefore only a few tens to a few hundreds of micrometers. Laser radiation at this wavelength is therefore largely absorbed in the vitreous body of the eye before reaching the delicate retina, which greatly increases the damage threshold for untreatable eye damage. On the other hand, since radiation energy at this wavelength is absorbed over only micrometers of lengths, powerful 2-µm lasers are being used as laser cutting tools for medical surgery, including ophthalmology and dentistry [78].

Besides water (vapor), other atmospheric gases such as CO_2 and N_2O exhibit strong absorption lines at 2 µm, which allows detection and analysis of these gases in this spectral region. This, in combination with the eye-safe characteristics, is the reason for using 2-µm thulium/holmium lasers for LIDAR (LIght Detection And Ranging, 'optical radar') systems [79], which work in a similar way as radar systems through the detection of back-scattered signals. LIDAR is for example being used in precision agriculture, to map the lay of the vegetation, the quality of the soil or elevation differences, or for preservation of forests by measuring the biodiversity. Other examples of LIDAR systems include measurements of wind speed and vortices at airports, traffic speedlimit radars, and specifically at 2 µm the ability to measure the concentration of greenhouse gases such as CO_2.

There has been considerable interest in the application of gas sensors for medical purposes. Of exhaled breath, 99.99% is a mixture of N_2, CO_2, O_2, water vapor and inert gases. However, more than 500 different compounds constitute the remainder (less than 100 ppm) of exhaled breath [80]. It is these compounds that are very interesting as indicators, or biomarkers, of for example: diabetes, liver and kidney diseases, bacterial infections or dental diseases. Being a non-invasive measurement technique, breath analysis is very convenient and rather safe for both the patient and the person taking samples. The difficulty in breath analysis lies with the fact that concentrations of biomarkers vary between different persons, and over time between cycles of breath exhalation. Nevertheless, if fast-scanning and sensitive detectors can be developed, gas sensing is a very attractive field for diagnostics and monitoring in medicine [81, 82]. For example, exhaled NH_3 is a suitable biomarker for detection of kidney disorders, bacterial stomach infections, and levels of fatigue [83, 84].

Because optical detection has applications in so many different fields, the development of sensors and light sources has accelerated. For detection of gases in low concentrations by means of absorption spectroscopy, either high optical power, or using detection cells with very high Q-factor cavities, or a combina-

tion of both is necessary. Powerful, tunable laser sources are available in the form of large, table-top solid-state pump lasers and OPO's in the wavelength range between $3 - 5$ µm [85, 86]. However, the form factor and cost of these systems poses a problem for mobile applications. The shrinking of light sources has benefits for mobility of these systems and in addition could allow a reduction of price. Various compact systems have been developed for that reason, such as DFB diode, VECSEL, and interband-cascade lasers in the mid-infrared wavelength range [87–89]. In the telecom wavelength range of $1.5 - 1.65$ nm the molecular absorption strength of gases is much lower than in the mid-infrared wavelength range, but light sources are more mature in terms of compactness, cost, and availability. Gas detection systems using diode lasers to detect NH_3 and CO_2 down to ppb levels in this wavelength range have also been demonstrated [90–94], but either fiber amplifiers had to be used to increase the optical intensity or the use of very high finesse optical cavities to create long optical pathlengths. Detecting NH_3 and CO_2 around 2 µm has the advantage of absorption strength increasing by factors of 3 and 100, respectively, compared to the absorption line strengths around 1.5 µm [95]. At 2 µm, the detection of NH_3 and CO_2 with ppm concentration levels has successfully been demonstrated with fiber-coupled, distributed-feedback diode lasers having output powers of several tens of milliwatts [95–97]. The combination of increased absorption strength at 2 µm with even more powerful lasers would improve the limit of detection of gases such as NH_3 and CO_2 even further.

1.5 The human trace gas sensing project

In 2009, an IOP Photonics Devices project was initiated to develop a compact sensor in the 2 µm wavelength range. This sensor has potential applications for the detection of kidney failure by detection of the NH_3 levels in human exhaled breath. Since fatigue is a commonly expressed complaint at medical practices, the development of a measuring device by detecting the amount of CO_2 is desirable, as the CO_2 pressure in exhaled air and in blood is related to the efficacy of the elimination of CO_2 from the human body. The development of a compact laser source and sensor at 2 µm could satisfy the goal to deliver a laser source for the detection of these gases at 2 µm.

The project was a joint project between the Molecular and Laser Physics group at the Radboud University in Nijmegen, The University Medical Center in Utrecht, the companies LioniX from Enschede and Sensor Sense from Nijmegen, and the Integrated Optics and MicroSystems group from the University of Twente, Enschede. The laser source for this project was developed at the Optics and MicroSystems group.

The laser source for this project, being the subject of this thesis, had the

requirements of delivering 100 mW of laser output power at 2 µm, and tuneability over a nanometer. The resulting laser of this work was developed in a thulium-co-doped potassium double tungstate host material and delivered up to 1.6 W of continuous-wave output power at 81% slope efficiency from a compact channel waveguide laser. This is far more than the desired 100 mW the laser source was needed to deliver. In addition, tuneability of this laser over several hundreds of nanometers has been demonstrated, albeit with the use of an external cavity.

1.6 Overview of this thesis

This thesis is about the design, fabrication and characterisation of thulium-co-doped channel waveguide lasers in a monoclinic potassium double tungstate host material. The thesis starts in this chapter 1 with giving an overview of the benefits of integrated optics in general, and more specifically about the benefits of integrated optics on potassium double tungstates. The state-of-the-art in 2-µm lasers is presented, as well as a brief overview of some applications of 2-µm lasers.

Chapter 2 concerns the fabrication of the buried, channel waveguides in potassium double tungstate. An explanation of the properties of this particular host material is given, and the method of growing, (co-)doping and processing of the material is explained. The optimum waveguide parameters obtained via simulations are given and explained.

Chapter 3 is dedicated to the properties of the thulium ion in relation to the potassium double tungstate host material. Spectroscopic properties are detailed, such as the energy-transfer and gain properties of thulium. The theory of this chapter is used in chapter 4 to discuss the obtained results.

In chapter 4, the main results of this thesis are presented. The characterisation method of several buried, channel waveguide lasers is explained and properties such as output power, efficiency, and tuneability are reported and compared to theory.

Finally, in chapter 5, general conclusions based on the work in this thesis are presented. Some preliminary results on resonant structures and a discussion of further future work is also presented.

CHAPTER 2

Waveguide design and fabrication

This chapter gives an overview of the steps required to fabricate monoclinic double tungstate channel waveguides for laser applications. The design considerations such as geometry and refractive index contrast of the channel waveguides are discussed. The growth of epitaxial layer on substrates via liquid-phase epitaxy, with the aspects of lattice matching and obtaining the desired refractive index contrast is then explained. Finally, the processes of lapping and polishing of grown epitaxial layers, followed by etching of the channel waveguides and their overgrowth is discussed.

Table 2.1 gives an overview of the required steps for the fabrication of buried channel waveguides in double tungstate layers.

2.1 Crystal properties

In order to fabricate compact and efficient waveguide lasers in double tungstate crystals, one must understand the various physical and optical properties of this material. Aspects such as the polarisation of the laser output, the amount of pump light that is absorbed and laser light that is generated and their efficiency is strongly dependent on the composition and orientation of the crystal.

2.1.1 Crystallographic and optical axes

The double tungstate crystals are strongly anisotropic biaxial crystals which belong to a family of crystals having a structure formula of [A][TM]$(WO_4)_2$, where [A] is a monovalent alkali-metal cation and [TM] is a trivalent metal or a rare-earth cation. The type of double tungstate crystals described in this thesis are compositions of $KY(WO_4)_2$, $KLu(WO_4)_2$, $KGd(WO_4)_2$ and $KTm(WO_4)_2$; the family of potassium double tungstates with optically active and inactive ions. The crystal structure of the potassium double tungstates depends on the growth temperature, yielding a tetragonal β-$KY(WO_4)_2$ for the high temperature growth and monoclinic α-$KY(WO_4)_2$ for the low-temperature growth. The low-temperature α-$KY(WO_4)_2$ phase crystallises in the monoclinic centro-symmetric space group *C2/c* or *I2/c*. Both space groups belong to the $2/m$ point group and have Schönflies notation C_{2h}^6. This means that they describe the same crystal

structure but use different coordinates for the monoclinic unit cell. The *I2/c* notation is more intuitive to use than the *C2/c* notation, because the base angle of $\beta = 94°$ between the c*- and a*-axes aligns exactly to the crystal morphology as shown in Fig 2.1. In the *C2/c* notation, the angle between the a- and c-axes is approximately $\beta = 134°$. The c*- and c-axes of both notations run parallel, but in opposite directions. The b*- and b-axes are parallel to each other and at right angles with the $a^{(*)}/c^{(*)}$-plane.

The optical axes N_g and N_m of the monoclinic double tungstates do not align with the crystallographic axes defined by the *C2/c* or *I2/c* notations. Instead, N_g is rotated approximately 17.5° with respect to the c-axis in the $a^{(*)}/c^{(*)}$ plane. N_g and N_m are at right angles with respect to each other within the $a^{(*)}/c^{(*)}$-plane, while N_p is at right angles with the $a^{(*)}/c^{(*)}$-plane and runs parallel to b(*).

Table 2.1 Process flow for the fabrication of buried channel waveguide lasers in co-doped double tungstate crystals in eight consecutive steps.

Step	Process description	Paragraph
1	Determination of the active layer composition in terms of dopant concentration of the optically active ions, based on their absorption and emission coefficients and expected channel length.	2.1.1
2	Simulation and optimisation of the waveguide modal overlap, while making realistic variations on the channel geometry and refractive index contrast.	2.1.2 and 2.3
3	Determination of the solvent/solute mixture that yields a lattice-matched active layer after liquid-phase epitaxy and fulfils the refractive index requirements.	2.2.1
4	Growth of the active double tungstate layer onto an undoped 010-oriented double tungstate substrate, by liquid-phase epitaxy.	2.2.3
5	Lapping and polishing of the active layer to the required thickness.	2.4.1
6	Micro-structuring of channel waveguides into the planar, active layer, using standard lithography and argon-beam etching.	2.4.2
7	Overgrowth of the channel waveguides by liquid-phase epitaxy, to symmetrise and protect the waveguide.	2.2.3
8	Dicing and end-facet polishing of the crystal containing the buried channel waveguides.	2.4.1

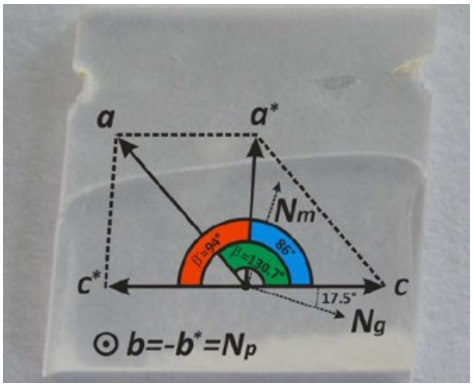

Figure 2.1 The crystallographic and optical axes of monoclinic potassium double tungstate crystals. The crystal axes are indicated according to the Schönflies notation, *C2/c* (without asterisk) and *I2/c* (with asterisk). The optical axes N_g, N_m and N_p are indicated by dashed arrows. Figure adapted from Geskus [98].

2.1.2 Refractive indices

As a result of the anisotropic nature of the monoclinic double tungstates, these crystals are birefringent. The asymmetric nature of the unit cell causes a biaxial behaviour. The three axes of the optical indicatrix, N_g, N_m and N_p, correspond to the maximum, intermediate and minimum refractive indices, n_g, n_m and n_p, respectively (g = 'grand', m='medium', p='petit'). Data on the dispersion curves for the three polarisations are available in the literature for the pure compounds $KY(WO_4)_2$ [99], $KLu(WO_4)_2$ [100], and $KGd(WO_4)_2$ [101], and are presented in table 2.2. The available data are presented using non-infrared-corrected and infrared-corrected Sellmeier equations, but the most commonly used form in the literature is the single-term (non-infrared-corrected) Sellmeier equation used by Kaminskii for pure $KY(WO_4)_2$ [99]:

$$n^2 = A + B\lambda^2/(\lambda^2 - C^2), \tag{2.1}$$

with λ the optical vacuum wavelength in micrometers.

The dispersion curves for the different polarisations of the different crystals are plotted in figure 2.2, using the Sellmeier equations and data from table 2.2. In the figure, the solid sections of the curves represent the wavelength range over which the dispersion curves have been measured, while the dashed sections represent the extrapolation up to 2 µm. It becomes clear from the solid sections of the dispersion curves that $KY(WO_4)_2$ exhibits the lowest, $KGd(WO_4)_2$ the intermediate, and $KLu(WO_4)_2$ the highest refractive index for all polarisations. Gd^{3+} has a larger electron number, but also a larger ion radius than Y^{3+}. The latter effect partially compensates the former, resulting in only a small enhancement

Table 2.2 Sellmeier coefficients reported in the literature of pure potassium double tungstate crystals. The compounds $KY(WO_4)_2$, $KLu(WO_4)_2$ and $KGd(WO_4)_2$ have been indicated for the different polarisations N_g, N_m and N_p.

Compound	Polarisation	A	B	C [µm]	D [μm^{-2}]	Ref.
$KY(WO_4)_2$	Sellmeier eqn.: $n^2 = A + B\lambda^2/(\lambda^2 - C^2)$					[99]
	N_g	1	3.1278346	0.161512	-	
	N_m	1	2.9568303	0.1591855	-	
	N_p	1	2.8134935	0.1529056	-	
$KGd(WO_4)_2$	Sellmeier eqn.: $n = A + B/\left[1 - (C/\lambda)^2\right] - D\lambda^2$					[101]
	N_g	1.3867	0.6573	0.17002	0.2913×10^{-3}	
	N_m	1.5437	0.4541	0.18891	2.1567×10^{-3}	
	N_p	1.5344	0.4360	0.18618	2.0999×10^{-3}	
$KLu(WO_4)_2$	Sellmeier eqn.: $n^2 = A + B/\left[1 - (C/\lambda)^2\right] - D\lambda^2$					[100]
	N_g	3.58334	0.73512	0.26700	0.02953	
	N_m	3.36989	0.74309	0.26193	0.04331	
	N_p	3.21749	0.75382	0.25066	0.05076	

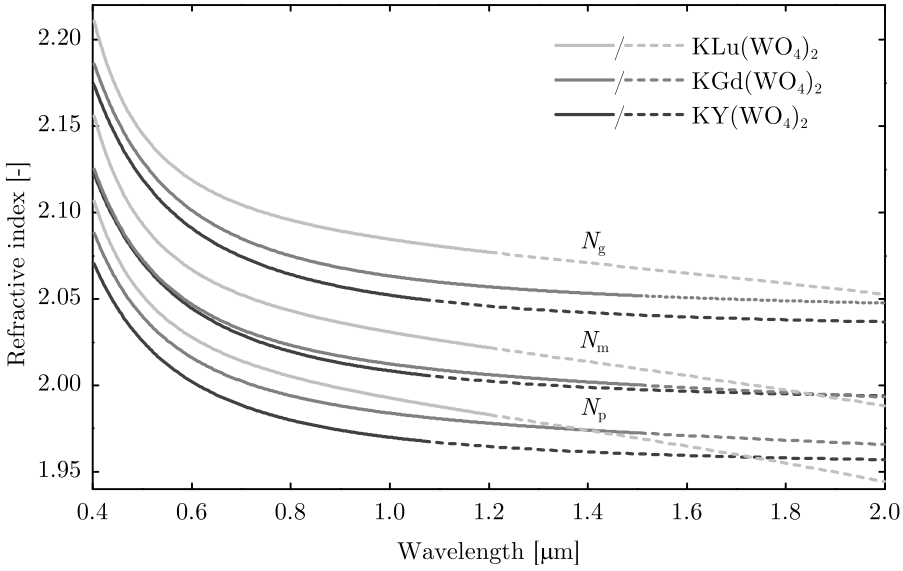

Figure 2.2 Dispersion curves of pure potassium double tungstate crystals. The dispersion curves are plotted using the Sellmeier equations and data of table 2.2, for the different polarisations. The solid section of the curves represent the wavelength range from which the data was obtained, while the dashed sections represents the extrapolation up to 2 µm via the Sellmeier equations.

of the electron density of Gd^{3+} compared to Y^{3+} and therefore only small increase of the refractive index of $KGd(WO_4)_2$ compared to $KY(WO_4)_2$. Lu^{3+} has an even higher electron number than Gd^{3+}, and combined with the lanthanide contraction which decreases the ion radius of Lu^{3+} with respect to Gd^{3+}, this leads to a significantly higher electron density and therefore highest refractive index of $KLu(WO_4)_2$ compared to the other two tungstate crystals. At wavelengths extrapolated beyond 1.2 µm, the plotted dispersion curve of $KLu(WO_4)_2$ exhibits a near-linear behaviour with a negative $dn/d\lambda$, crossing the dispersion curves of the other compounds. Since the refractive index is related to the electron density, which is highest for $KLu(WO_4)_2$, it is expected that the crossings of the $KLu(WO_4)_2$ dispersion curve with the dispersion curves of $KGd(WO_4)_2$ and $KY(WO_4)_2$ is erratic and caused by accumulation of extrapolation uncertainties.

The thulium lasers in this work are fabricated in crystal compositions from a combination of Y^{3+}, Gd^{3+}, Lu^{3+} and Tm^{3+}. The refractive index of these compounds can be estimated by the linear approximation

$$n_{\mathrm{g,m,p}} = \sum_i f_i n_{\mathrm{g,m,p}}(i). \tag{2.2}$$

Here, f_i is the fraction $1 - x - y - z$, x, y and z of the constituent ions $i = Y^{3+}$, Gd^{3+}, Lu^{3+} and Tm^{3+}, respectively, and $n_{g,m,p}$ the wavelength-dependent refractive index of the corresponding pure compounds. The sum of the fractions f_i equals unity. (In case the concentrations are given in at.%, the fractions can be calculated by dividing by 100.) In this way, it is possible to estimate the refractive index of co-doped compounds with low thulium concentrations and for wavelengths up to 1.2 µm, which lies within the characterisation range of the data in table 2.2.

Since the thulium lasers operate at wavelengths around 2 µm, knowledge of the refractive index at this wavelength is required for the optimisation of the waveguide dimensions. We have therefore measured the refractive index for a number of co-doped, $KY_{1-x-y}Gd_xLu_yTm_z(WO_4)_2$, layers with varied thulium concentrations. Dark m-line spectroscopy was carried out using a Metricon 2010M film prism coupler. A set of cross-polarisers was utilised to pre-orient the in-plane optical axes N_g and N_m with respect to the orientation of the prism. A series of measurements was then performed to ensure the propagation direction of the coupled light was running parallel to the optical axes, by correcting the incident angle of the incoupled light until a maximum or minimum index of refraction was found for the N_g or N_m polarisation, respectively. With the sample fixed in this position, subsequently, the measurement was carried out at wavelengths of 633, 830, 1300 and 1550 nm. The refractive index n_p along the N_p optical axis was characterised using transverse-magnetic-polarised light propagating along either the N_g or N_m optical axis, in both cases providing identical values for n_p. The refractive indices n_g and n_m were determined by coupling in transverse-electric-polarised light, propagating along the N_m or N_g optical axes, respectively. The single-term Sellmeier coefficients to equation 2.1 were derived from the measured data by means of a least-squares fit. The Sellmeier coefficients for the different compositions are presented in table 2.3. The measured data, along with the approximate, fitted, dispersion curves based on these data are plotted in figure 2.3. As expected, the dispersion curve of a pure $KY(WO_4)_2$ crystal, which was also measured, shows the lowest refractive index compared to the co-doped crystals. The series of four co-doped crystals is made up of two groups of vastly different Y^{3+} content. The first group has a Y^{3+} content of 40 at.% and a thulium content of 1.5 at.% and 3.0at.%, respectively, while in the second group all Y^{3+} has been replaced by Gd^{3+}, Lu^{3+} and Tm^{3+}, and with a thulium content of 1.5 at.% and 20.0 at.%, respectively. From the figure, it is clear that the difference of the refractive index is only due to the Y^{3+} content, as a large difference is observed between the two groups of different Y^{3+} content, but no difference is observed for the different thulium contents of 1.5 at.% versus 3.0 at.% and 1.5 at.% versus 20.0 at.%. While no information about the refractive index of $KTm(WO_4)_2$ is found in the literature, we conclude from this that the refractive index of $KTm(WO_4)_2$ must be almost identical to that of $KLu(WO_4)_2$, which is also to be expected

Table 2.3 Single-term Sellmeier coefficients for co-doped $KY_{1-x-y-z}Gd_xLu_yTm_z$ crystals, obtained by dark m-line spectroscopy at 633, 830, 1300 and 1550 nm. The concentrations of Y^{3+}, Gd^{3+}, Lu^{3+} and Tm^{3+} are in at.%.

Y^{3+}	Gd^{3+}	Lu^{3+}	Tm^{3+}	Polarisation	B	C^2 [µm^2]
100.0	0.0	0.0	0.0	N_g	3.11897	0.02761
				N_m	2.95349	0.02628
				N_p	2.80731	0.02485
40.0	29.5	29.0	1.5	N_g	3.14470	0.02764
				N_m	2.97916	0.02643
				N_p	2.84836	0.02510
40.0	29.3	27.7	3.0	N_g	3.14609	0.02770
				N_m	2.97860	0.02646
				N_p	2.84913	0.02503
0.0	49.3	49.2	1.5	N_g	3.16556	0.02781
				N_m	2.99826	0.02650
				N_p	2.88065	0.02541
0.0	47.0	33.0	20.0	N_g	3.16541	0.02792
				N_m	2.99883	0.02651
				N_p	2.88088	0.02533

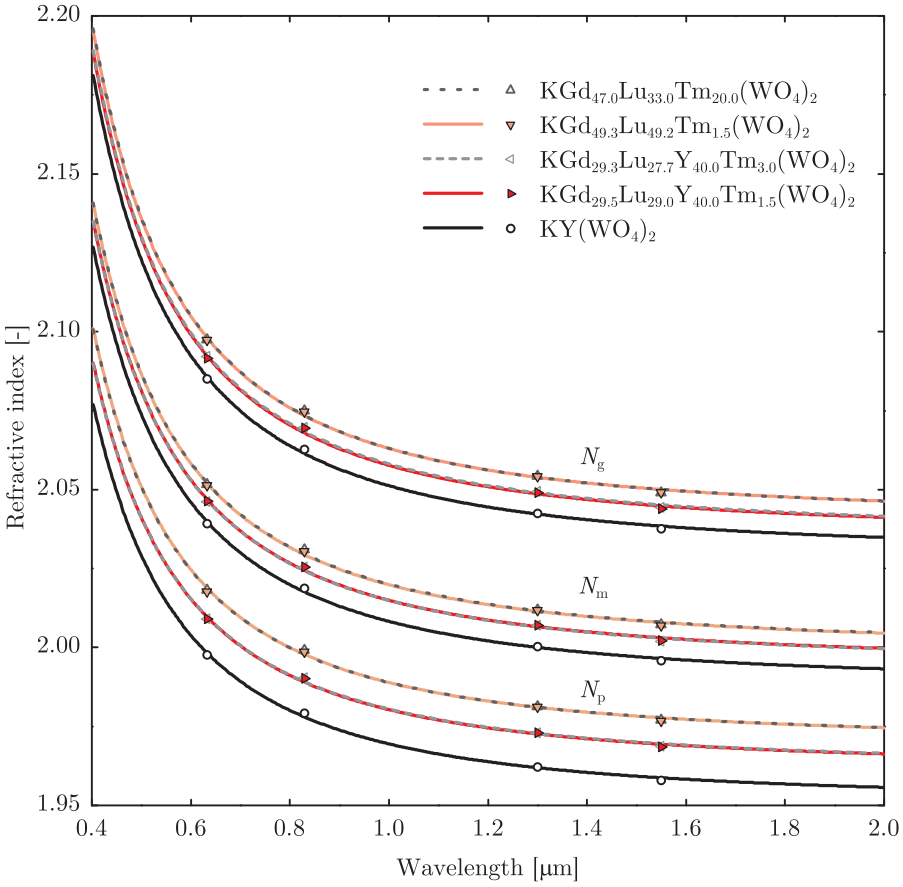

Figure 2.3 Dispersion curves of co-doped $KY_{1-x-y-z}Gd_xLu_yTm_z$ crystals. The dispersion curves are plotted using the single-term Sellmeier equation and data from table 2.3. The refractive indices at wavelengths of 633, 830, 1300 and 1550 nm, obtained by dark *m*-line spectroscopy are also indicated. The concentrations are all in at.%.

when looking at the atomic number of thulium (68) compared to yttrium (70) and their atomic radius and resulting lattice constants, which are similar.

2.2 Liquid-phase epitaxy of monoclinic double tungstates

Now that the optical properties of the crystals have been laid out in the previous paragraph, the growth of these crystal layers will be discussed. In order to create a crystal layer with sufficient thickness for further processing, it is vital to minimise the lattice mismatch between the pure substrate and the co-doped guiding layer, thereby minimising layer stress and related crack formation during further crystal sample processing, such as lapping, polishing and micro-structuring of channel waveguides. Besides the calculation aspect of the lattice mismatch, it also takes much experience in setting-up growth of these crystal layers by liquid-phase epitaxy. The growth of all layers used in this thesis were performed by Dr. S. Aravazhi in the Integrated Optics and MicroSystems group at the University of Twente.

2.2.1 Lattice matching

Optical waveguiding applications require elevated refractive indices for the guiding layer compared to the surrounding $KY(WO_4)_2$ substrate and cladding layers. Co-doping of the guiding layer with optically active ions such as Yb^{3+} or Tm^{3+} readily increases the refractive index of the layer, but only by small amounts in the order of 10^{-4} and for small dopant concentrations in the order of 1.2–2.4 at.% [43]. The adverse effect of co-doping of the active layer by a single ion such as Yb^{3+} or Tm^{3+} is the introduction of lattice mismatch with respect to the $KY(WO_4)_2$ substrate and optional cladding layer as a result of the different ionic radii of Yb^{3+} or Tm^{3+} as compared to the replaced Y^{3+} ions. A high degree of lattice mismatch and therefore lattice stress and potential crack formation can be prevented by limiting the dopant concentration in a nearly stoichiometric compound to a few at.%, which is typically enough for operating planar or channel waveguide lasers. Additional co-doping of the guiding layer with optically inert Gd^{3+} and Lu^{3+}, however, has been demonstrated to compensate for the lattice mismatch of the optically active ions, while at the same time providing a means to fine-tuning the layer refractive index [48]. This method is used in this thesis to prevent cracking of crystal samples with high amounts of Tm^{3+}. The lattice parameters of the stoichiometric compounds $KY(WO_4)_2$, $KGd(WO_4)_2$, $KLu(WO_4)_2$ and $KTm(WO_4)_2$ are presented in table 2.4. From this table it is clear that $KLu(WO_4)_2$ has the smallest, $KY(WO_4)_2$ the intermediate, and $KGd(WO_4)_2$ the largest lattice size. The lattice size of $KTm(WO_4)_2$ is expected

Table 2.4 Lattice parameters of monoclinic potassium double tungstates according to the Schönflies coordinate system. The number of significant digits given is identical to the original publications.

Material	a [Å]	b [Å]	c [Å]	β [°]	T [K]	Ref.
$KY(WO_4)_2$	10.63134	10.34526	7.55472	130.7522	298	[102, 103]
$KGd(WO_4)_2$	10.68906	10.44385	7.60364	130.7713	298	[102]
	10.6524	10.3746	7.5822	130.802	293	[104]
$KLu(WO_4)_2$	10.58985	10.23625	7.49623	130.74452	298	[100]
	10.5767	10.2147	7.4872	130.684	293	[100]
$KEr(WO_4)_2$	10.613	10.315	7.534	130.732	298	[105, 106]
$KTm(WO_4)_2$	10.60	10.29	7.510	130.70	298	[107, 108]
$KYb(WO_4)_2$	10.6003	10.2673	7.5066	130.766	298	[102]

to be similar to that of $KLu(WO_4)_2$, as already explained in sub-section 2.1.2, because of the similar ionic radii and lattice constants. The introduction of $KLu(WO_4)_2$ in a $KY(WO_4)_2$ crystal therefore leads to tensile strains, while the introduction of $KGd(WO_4)_2$ leads to compressive strains. By assuming a linear change of lattice parameters when gradually replacing ions of one stoichiometric compound for another, according to Vegard's law [109], the amounts of Y^{3+}, Gd^{3+}, Lu^{3+} and Tm^{3+} that lead to a minimum lattice mismatch can be calculated. Because of thermal expansion, it is important that lattice parameters of the different compounds used for the calculation are measured at the same temperature. The lattice parameters of table 2.4 corresponding to a temperature of 298 K were therefore used in the calculations. The layer lattice parameters a_{layer} and c_{layer} and the lattice mismatch Δa and Δc of the layer with respect to the $KY(WO_4)_2$ substrate along the a- and c-axis, respectively, are calculated as:

$$a_{\text{layer}} = \sum_i f_i a_i \tag{2.3}$$

$$c_{\text{layer}} = \sum_i f_i c_i \tag{2.4}$$

$$\Delta a = \frac{a_{\text{layer}} - a_{\text{KY(WO}_4)_2}}{a_{\text{KY(WO}_4)_2}} \tag{2.5}$$

$$\Delta c = \frac{c_{\text{layer}} - c_{\text{KY(WO}_4)_2}}{c_{\text{KY(WO}_4)_2}}, \tag{2.6}$$

where f_i is the fraction $1-x-y-z, x, y$ and z of the constituent ions $i = Y^{3+}$, Gd^{3+}, Lu^{3+} and Tm^{3+}, respectively and a_i and c_i the lattice cell param-

eters of the constituents from table 2.4 along the a- and c-axis, respectively. The calculated lattice mismatch for the a- and c-axis of $KY_{1-x-y-0.015}Gd_x$-$Lu_yTm_{0.015}(WO_4)_2$ and $KY_{1-x-y-0.2}Gd_xLu_yTm_{0.2}(WO_4)_2$ are plotted in figures 2.4a and 2.4c, respectively, using contour lines with a mismatch value of -0.2% up to 0.4% for the a-axis (solid black lines), and -0.6% up to 0.6% for the c-axis (solid gray lines). In these two figures, the dashed diagonal line represents the summed fraction of unity of the co-dopants Gd^{3+}, Lu^{3+} and Tm^{3+}, which happens when all of Y^{3+} is replaced by Gd^{3+}, Lu^{3+} and Tm^{3+}. The figures 2.4b and 2.4d display the remaining fractions of Y^{3+} (solid black lines) and the refractive index contrast at a wavelength of 800 nm (solid gray lines), which corresponds to the pump wavelength for pumping Tm^{3+} in this thesis. Since the lattice parameters vary differently along the crystal a- and c-axis from one stoichiometric compound to another, perfect lattice matching between the grown layer and the $KY(WO_4)_2$ substrate and cladding cannot be obtained simultaneously along both axes. For example, the mismatch along the a-axis has a stronger dependence on the gadolinium fraction, whereas the mismatch along the c-axis has a stronger dependence on the lutetium fraction, as can be derived from the orientation of the contour lines. From these figures it also becomes clear that the contour lines indicating 0% mismatch along the a- and c-axis become more divergent as the Gd^{3+} and Lu^{3+} fractions are increased. The optimum lattice mismatch for the a- and c-axis simultaneously therefore lies precisely between the 0% contour lines for the a- and c-axis. From equations 2.5 and 2.6, this optimum is found when the lattice mismatch along the a- and c-axis are equal in value but of opposite sign:

$$\Delta a = \frac{a_{\text{layer}} - a_{\text{KY(WO}_4)_2}}{a_{\text{KY(WO}_4)_2}} = -\frac{c_{\text{layer}} - c_{\text{KY(WO}_4)_2}}{c_{\text{KY(WO}_4)_2}} = -\Delta c \tag{2.7}$$

The compositions $KY_{0.4}Gd_{0.295}Lu_{0.29}Tm_{0.015}(WO_4)_2$, $KGd_{0.493}Lu_{0.492}Tm_{0.015}$-$(WO_4)_2$ and $KGd_{0.47}Lu_{0.33}Tm_{0.20}(WO_4)_2$ of table 2.3 were selected according to this rule, and also displayed in figure 2.4. Their lattice mismatch values $\Delta a = -\Delta c$ are 0.043%, 0.071% and 0.068%, respectively. The composition $KY_{0.40}$-$Gd_{0.293}Lu_{0.277}Tm_{0.03}(WO_4)_2$ is not shown in figure 2.4, as it is very similar to the 1.5at.% Tm-doped sample with the same Y^{3+} fraction and lattice mismatch values of $\Delta a = -\Delta c = 0.042\%$. From numerous growth experiments with these and other layer compositions it is estimated that for a crack-free growth the lattice mismatch should be kept below approximately 0.08% [52].

2.2.2 Dopant concentration of rare-earth ions in co-doped tungstates

It is common in the literature, and also in this thesis, to express the concentration of impurity ions in at.%, with respect to the amount of yttrium (or lutetium

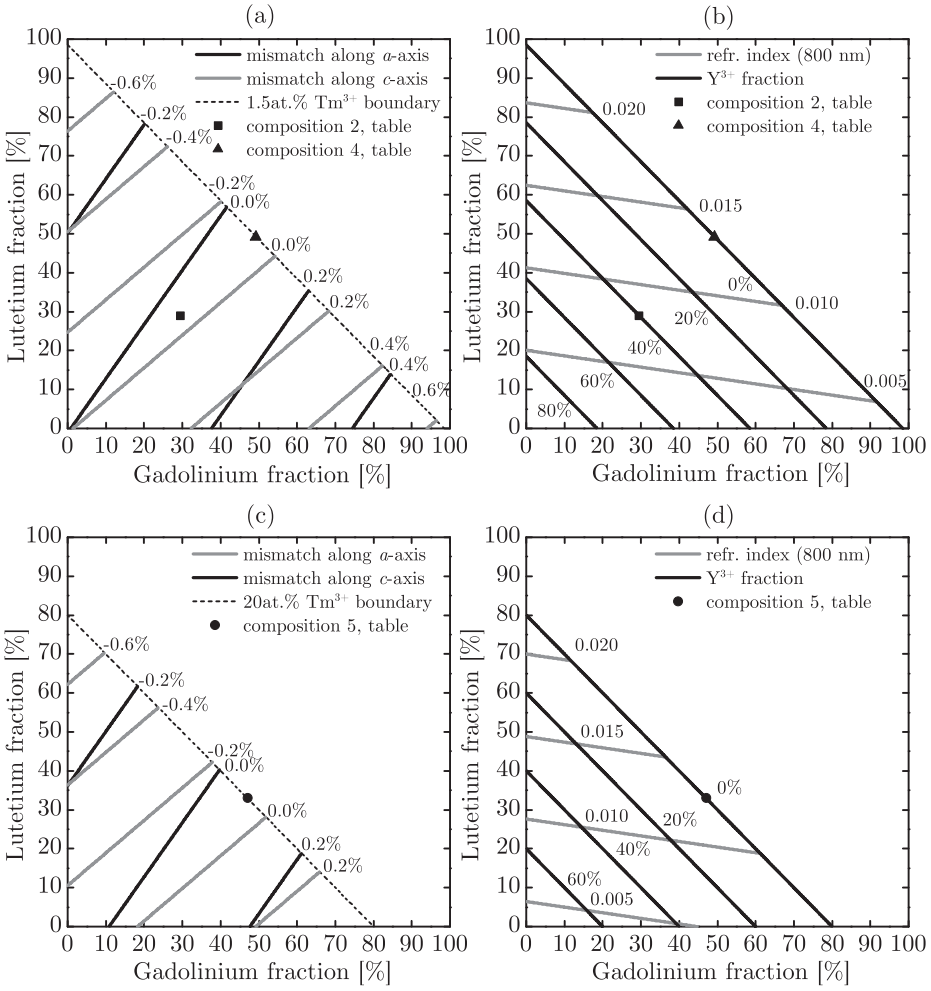

Figure 2.4 Lattice mismatch and refractive index contrast of $KY_{1-x-y-z}Gd_xLu_yTm_z(WO_4)_2$ thin layers with the undoped $KY(WO_4)_2$ substrate. The mismatch along the *a*- and *c*-axis, for (a) 1.5 at.%, and (c) 20 at.% thulium-doped samples. The refractive index contrast at the pump wavelength of 800 nm is displayed for (b) 1.5 at.%, and (d) 20 at.% thulium-doped samples. The numbered compositions in the figures are referring to the compositions in table 2.3.

or gadolinium) that is replaced by the respective ion. A concentration of 10 at.% of thulium impurities in $KY(WO_4)_2$ therefore means that compared to the concentration of 100 at.% of yttrium in a stoichiometric compound, 10% of the yttrium lattice sites contain a thulium ion in the non-stoichiometric (mixed) compound. This way of expressing the dopant concentration is convenient in crystal growth for determining the weight amount of the different compounds in a solvent/solute mixture. However, in laser physics it is mandatory to know the concentration density in units of ions per unit volume for the calculation of parameters such as the gain per unit length and for comparison of dopant concentrations between different host materials.

From the data in table 2.4, by using the length of the vertices a, b, c of the lattice unit cells and the angle β between the a- and c-axes for the monoclinic unit cells, the volume V_{uc} of a unit cell can be calculated by $V_{\mathrm{uc}} = abc \sin\beta$. Knowing that a double tungstate unit cell contains a number of 4 double tungstate molecules $KRE^{3+}(WO_4)_2$, the unit cell mass M_{uc} can be calculated from the summed molar mass of the separate elements divided by Avogadro's number. The density ρ of a double tungstate can be calculated by dividing the mass of a unit cell by its volume. In a double tungstate composition with fractions f_i of the stoichiometric compounds i, the compound density can be calculated as $\rho = \Sigma_i f_i \rho_i$. In this thesis we are concerned with the dopant concentration of thulium in a mixed compound consisting of fractions f_i of $KY(WO_4)_2$, $KGd(WO_4)_2$, $KLu(WO_4)_2$ and $KTm(WO_4)_2$. In a 1at.% thulium-doped tungstate such as $KY(WO_4)_2$, with a fraction $f_{\mathrm{Y}} = 0.99$ and a fraction $f_{\mathrm{Tm}} = 0.01$, the Tm^{3+} concentration in inverse cubic centimeters is calculated as $N_{\mathrm{Tm}} = 4 f_{\mathrm{Tm}} / \Sigma_i f_i V_{\mathrm{uc},i}$, where i refers to the fractions f_{Tm} and f_{Y} and $V_{\mathrm{uc},i}$ to the unit cell volumes, respectively. Analogously, the Tm^{3+} concentration for any composition and doping level can be calculated. The 1at.% Tm^{3+} doping levels for the (nearly) stoichiometric compositions, along with the density and mass and volume of a unit cell is given in table 2.5.

2.2.3 Growth by liquid-phase epitaxy

Bulk monoclinic double tungstate crystals are best grown from a solution using a technique called top-seeded solution growth (TSSG), also sometimes called 'modified Czochralski' growth. It does not differ much from the standard Czochralski growth method which employs a stoichiometric melt rather than a solution. The reason for growing the crystals from a solution is the crystal phase transition that occurs at a temperature of approximately 1025 °C, which is lower than the melting point of approximately 1080 °C: any attempt to grow a monoclinic, α-KYW crystal directly from a melt will result in an unstable crystal which disintegrates quickly [99]. Growing the crystals from a solution decreases the nucleation temperature below the transition point of α-KYW to β-KYW. The

Table 2.5 Calculation of thulium dopant concentration in double tungstates. The dopant concentration is derived from the mass and volume of a unit cell.

		Unit cell		Tm^{3+} concentration	
Compound	ρ	M_{uc}	V_{uc}		N_{Tm}
	[g cm^{-3}]	[10^{-21} g]	[10^{-22} cm^3]	[at.%]	[10^{19} cm^{-3}]
$KY(WO_4)_2$	6.581	4.143	6.294	1	6.356
$KGd(WO_4)_2$	7.150	4.597	6.428	1	6.225
$KLu(WO_4)_2$	7.657	4.714	6.156	1	6.497
$KTm(WO_4)_2$	7.402	4.674	6.210	-	-

nucleation temperature is reached when the temperature is low enough such that supersaturation occurs, which allows nucleates to precipitate and bind onto the crystal surface.

The different crystal axes discussed in paragraph 2.1.1 exhibit different growth speeds. The fastest growth speeds are related to unstable crystal faces and growth along these axes can provoke the formation of macro defects yielding a poor crystal quality. It has been found that the slowest, and most stable, growth direction is along the b-axis of the crystal (010 orientation), yielding the best crystal quality. All crystal layers that were used for the work reported in this thesis have been grown from b-oriented crystals, cut along this direction from TSSG-grown bulk crystals.

As a solvent, $K_2W_2O_7$ can be used for the crystal growth, or K_2O_4 with added WO_3 corresponding to $K_2W_2O_7$. A major advantage of using the tungsten-tungstate solvents is the absence of foreign ions which could otherwise significantly affect the laser performance of such crystals as a result of detrimental energy-transfer processes. The difference between the $K_2W_2O_7$ solvent and the K_2O_4 solvent with added WO_3 is that the former solvent has the lower melting temperature of 619 °C as opposed to 921 °C for the latter solvent [110]. The crystal growth speed is the highest for the K_2O_4 solvent, but the crystal growth quality is lower than obtained with the $K_2W_2O_7$ solvent. Therefore, the $K_2W_2O_7$ solvent is often used for bulk crystal growth using TSSG, and was also used for producing the crystal layers for the lasers in this work.

In figure 2.5a, a diagram of the liquid-phase epitaxy (LPE) oven is shown. The internal oven is clad with Al_2O_3 ceramic tiles that are able to withstand the high growth temperatures. A thermocouple, in combination with heating elements and a thermal controller is responsible for maintaining the correct growth temperatures. A 25-ml-volume platinum cup is placed inside the oven, containing

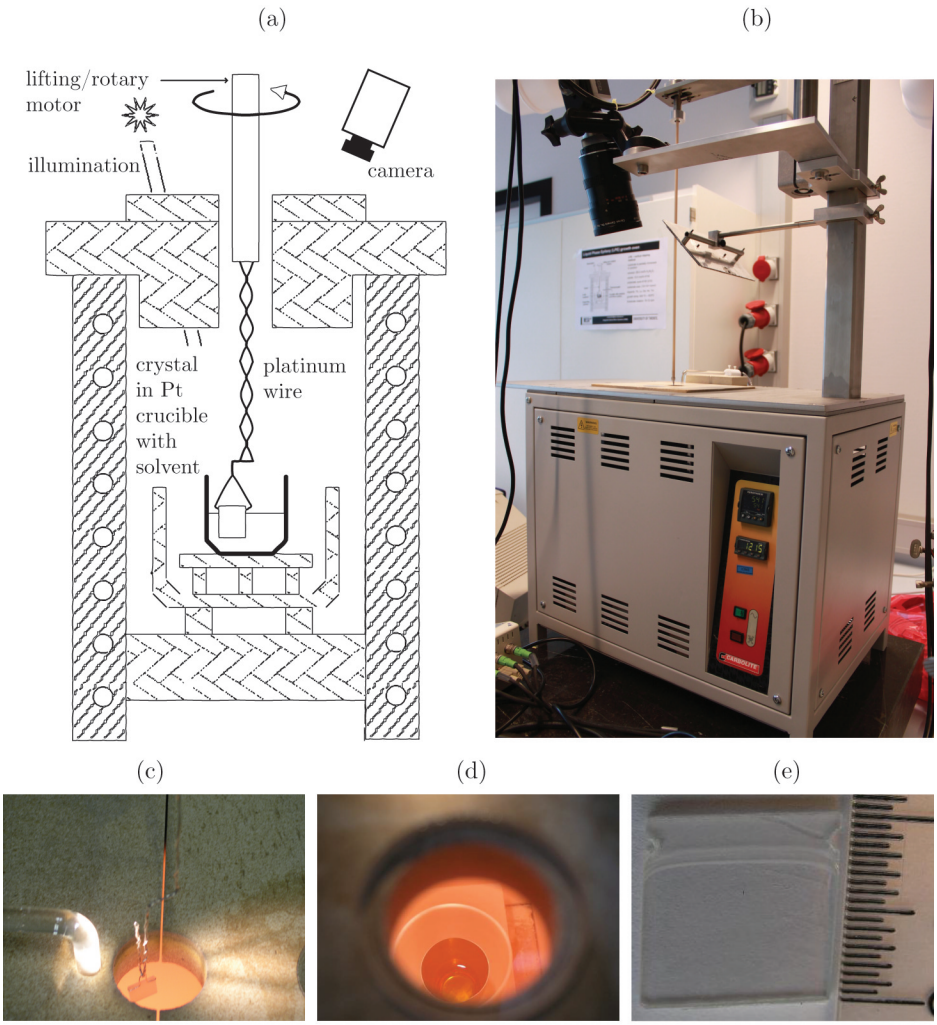

Figure 2.5 Diagram of the liquid-phase epitaxy set-up and growth process. (a) Cross-section of the liquid-phase epitaxy growth oven. The potassium double tungstate sample is suspended by a platinum wire into a platinum cup containing the solvent and solute. The sample is rotated during the growth process. (b) Photograph of the actual oven. (c) A sample is slowly lowered into the oven. (d) The platinum cup with the solvent and solute. (e) A potassium double tungstate crystal after the growth of a layer. The indents on the top of the sample are for the purpose of attaching the platinum wire.

the $K_2W_2O_7$ solvent and the potassium tungstate solute with the layer-specific rare-earth fractions. The solute/solvent ratio was $10.5 - 89.5$ mol%. To allow the solvent and solute to mix fully, the system is heated for several hours to a temperature well above the saturation temperature at which the formation of nucleates occurs. The system is then cooled to below the saturation temperature to obtain a supersaturated solution and left to stabilise for several hours more. The saturation temperature depends on the concentration of solute versus solvent. The growth temperature for the crystal layers used was between $920 - 923$ °C. As a result of the growth of a crystal layer and the high temperatures, solution is lost both to increased crystal weight and evaporation. However, since the solute $KY_{1-x-y-z}Gd_xLu_yRE_z(WO_4)_2$ is significantly less volatile than the solvent $K_2W_2O_7$, mostly the solvent evaporates. During a growth experiment the loss of solute is higher than the loss of solvent, which results in a decrease of the solute concentration and consequently a lower level of super-saturation during growth. In long growth experiments where a significant crystal weight increase is required, such as the formation of bulk crystals, the level of super-saturation is maintained by slowly lowering the temperature during the growth. For the layer growth experiments which require a layer thickness of only several tens of micrometers, the oven can be maintained at a constant growth temperature provided a sufficiently high level of super-saturation is present at the start to compensate the decreasing level of supersaturation during the growth.

To begin the layer growth, potassium tungstate substrates with a size of 1×1 cm^2 are suspended by a platinum wire, slowly lowered into the pre-heated oven, and finally dipped inside the platinum crucible once the oven has reached a stable condition of super-saturation. The oven, depicted in figure 2.5, is equipped with a stepper motor controlling the height of the substrate, as well as a rotary motor to rotate the substrate in the platinum cup during the growth to stimulate mixing of the solution and uniform layer growth. The dipping process is monitored by a camera. The sample is dipped into the solution to a maximum height of 8 mm (refer to figure 2.5e), preventing overgrowth of the platinum wires and cracking of the crystal. A typical growth rate between $15 - 18$ µm/h is obtained using this procedure, resulting in layer thicknesses of several tens of micrometers for growths up to several hours of duration. After the growth, the sample is raised 10 mm above the liquid surface, and cooled to room temperature with a rate of 25 K/h.

The layer quality has been investigated by Geskus, using X-ray diffraction techniques which confirmed the single crystalline nature of these grown layers. In addition, the concentration of the rare-earth ions in the layer was investigated using laser-ablation inductively coupled plasma mass spectrometry, indicating that the layer composition is close to that of the initial solution within 98% accuracy [44].

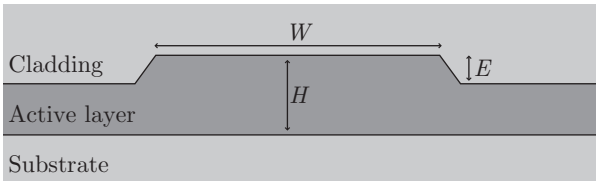

Figure 2.6 Geometry of a buried ridge-type channel waveguide. Parameters to vary are the thickness H of the doped layer, the channel width W and etch depth E. During the lithography and etching step, a slanted sidewall angle with respect to the surface appears, as a result of scattering of argon ions off the resist layer and the etched material.

2.3 Waveguide design

In the previous sections, the growth process of co-doped potassium double tungstates has been discussed and the effect of the concentration of co-dopants in the crystal layer on the refractive index has been investigated. By using the measured refractive index and combining this with the constraints on the fabrication process of buried channel waveguides, we will now investigate what the optimum channel waveguide dimensions should be to arrive at the best possible laser performance. The main considerations for designing the optimum channel waveguide dimensions are single transverse-mode operation of the laser and pump modes and the best possible mutual overlap between these modes and the gain medium. A good confinement of the pump and laser modes within the gain medium ensures the best possible energy transfer between the pump and laser light fields via the active rare-earth ions.

An overview of the channel waveguide geometry is presented in figure 2.6. The pure $KY(WO_4)_2$ substrate is covered with a (co-)doped potassium tungstate layer with a height H. A ridge-type channel waveguide with a width W is etched into the layer to a depth of E. The channels are covered with a pure $KY(WO_4)_2$ cladding layer to symmetrize the layer and optimise the optical mode overlap. The channel width, height and etch depth are parameters which influence the confinement and overlap of the optical modes, as well as the sidewall angle with respect to the surface that appears during the etching of the channels. The obtained sidewall angle during the etching of the channels in double tungstate layers via argon-beam etching is 85 degrees.

Optical mode simulations were performed using a commercial mode solver software package.[1] The polarisation-dependent refractive indices used in the simulation for the pump and laser wavelength are provided in table 2.6. The pump wavelengths used in the simulation are 794 nm for TM polarisation, and

[1] PhoeniX FieldDesigner, version 4.6.0 (www.phoenixbv.com)

802 nm for TE polarisation, since the absorption cross-sections are at a maximum at these wavelengths for a thulium laser in this double tungstate host. Since thulium has a very wide emission bandwidth and since the actual laser wavelength depends on factors such as the channel propagation loss which are not known beforehand, the optical modes corresponding to the laser were first simulated for the central line wavelength of 1840 nm, for both TE and TM polarisation. The layer thickness and channel width were varied between $4 - 16$ µm and $4 - 26$ µm, respectively. The etch depth was limited to a maximum of 2 µm, which was found to be a limitation in the etching procedure due to the maximum usable resist thickness, as will be discussed in the next section.

Figure 2.7 shows the results of the optical mode simulations. The overlap of the fundamental pump and laser modes with the active layer are calculated, as well as their mutual overlap. A high overlap of the pump and laser modes with the active layer promotes high pump power absorption and therefore a high gain on the laser transition, which is especially important for three-level laser schemes such as in the used thulium laser. The channel dimensions yielding the highest overlap exceeding 90% for both the pump and laser modes are for an active layer thickness beyond 10 µm. The channel width does not influence much the overlap of the optical modes with the active layer, however, the lateral confinement of the modes decreases as the channel width is decreased, as a result of the lowered channel effective index contrast. TM-polarised fundamental modes have a slightly better confinement than TE-polarised modes, due to the higher index contrast between the substrate/cladding and the active layer as seen from table 2.6. The difference however is only a few percent and therefore only the simulation results for the TE-polarisation are shown in figure 2.7. The gray and dashed areas in figure 2.7 represent channel waveguide dimensions which support not only the fundamental optical modes, but also higher order optical modes for the pump and laser, respectively. The existence of a higher-order laser mode has an adverse effect on the laser beam quality and therefore usability in applications which benefit from high-quality laser beams. The existence of

Table 2.6 Polarisation-dependent refractive indices used for optical mode simulations.

Layer	Pump		Laser	
	TE	TM	TE	TM
	802 nm	794 nm	1840 nm	1840 nm
$KY(WO_4)_2$	2.01973	1.98053	1.99414	1.95654
$KY_{40}Gd_{29}Lu_{28}Tm_3(WO_4)_2$	2.02642	1.99171	2.00052	1.96732

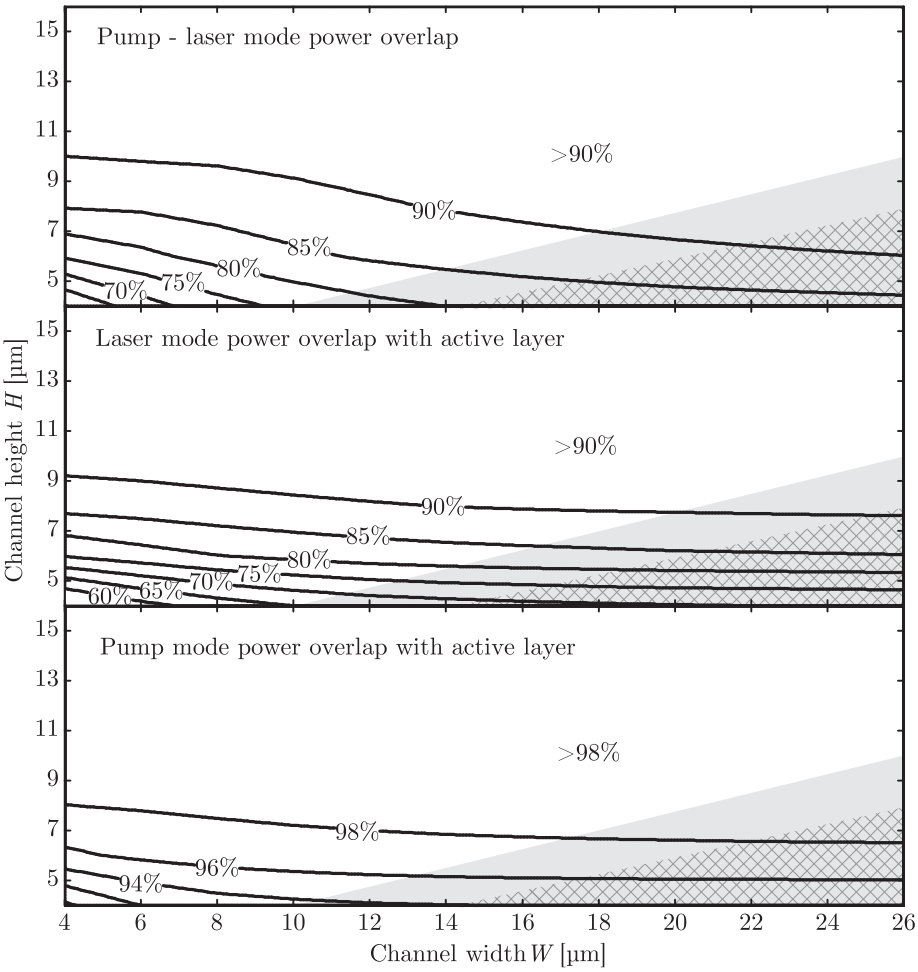

Figure 2.7 **Pump/laser/active region mode power overlap.** Calculated for a channel waveguide etched to a depth of $E = 1.9$ µm, and for TE polarisation. The gray areas on the lower righthand corners of the graphs designate multi-modal behaviour of the pump (undashed region) and laser modes (dashed region), whereas the white regions indicate purely fundamental-mode behaviour for the pump and laser.

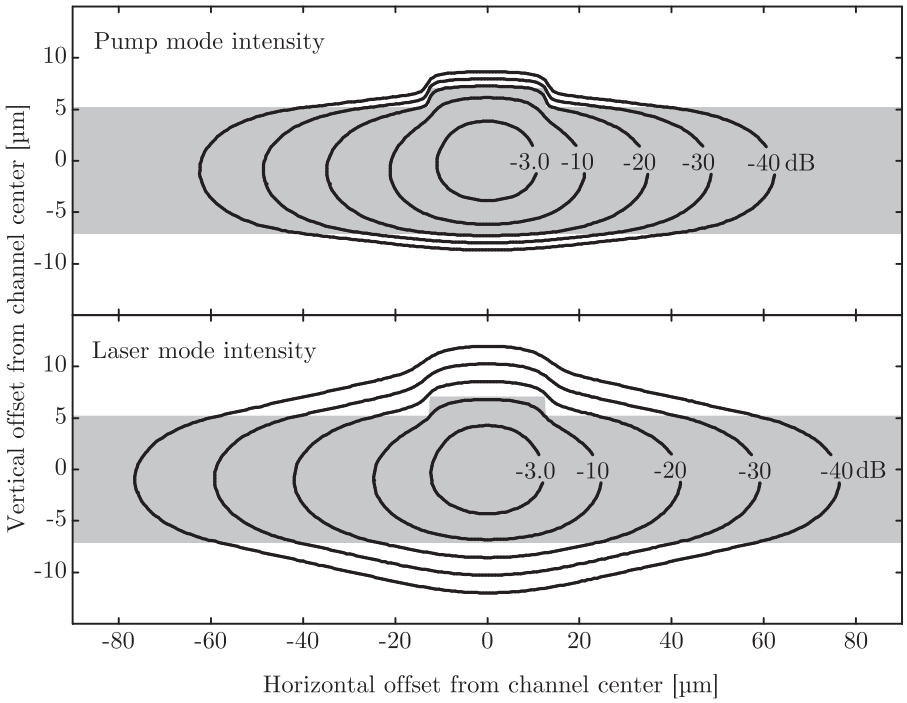

Figure 2.8 Fundamental pump and laser mode profiles. The intensity profiles were calculated at 794 nm in TM polarisation (pump) and 1840 nm in TM polarisation (laser), for a channel with a width of $W = 25$ µm, a height of $H = 14.3$ µm and an etch depth of $E = 1.9$ µm (gray area). The laser fundamental mode is wider than the pump fundamental mode as indicated by the intensity contours.

a higher-order pump mode in the channel waveguide has potentially an adverse effect on the extraction of pump power and conversion into laser power by the laser fundamental mode. Therefore, in the channel waveguides used in this work, the dimensions are selected with a safety margin such that multi-mode behaviour is not expected.

The resulting fundamental modes for the laser and pump were calculated for a channel waveguide with a height of $H = 14.3$ µm, a channel width of $W = 25$ µm and etch depth of $E = 1.9$ µm, and shown in figure 2.8. The intensity profiles confirm that the fundamental pump mode is tighter confined than the fundamental laser mode which has a longer wavelength. The $1/e^2$ intensity radii (horizontal, vertical) for the profiles shown in figure 2.8 are (19.7, 5.4) µm and (23.3, 6.1) µm for the pump and laser, respectively. The profiles for the TE-polarised fundamental modes are very similar to the ones in figure 2.8.

2.4 Waveguide micro-structuring

In sub-section 2.2.3, the growth of potassium double tungstate crystals by liquid-phase epitaxy has been discussed. The process of waveguide micro-structuring in double tungstates via argon-beam etching was primarily developed by Dr. D. Geskus for ytterbium-doped potassium double tungstate layers [98]. In the next sub-sections, the fabrication of buried, ridge-type channel waveguides for application for thulium-doped crystal layers will be discussed. The samples are first cleansed from growth residue, followed by lapping and polishing of a planar waveguide layer. A photo-lithography process followed by overgrowth and end-facet dicing and polishing concludes the process.

2.4.1 Lapping and polishing

Surface lapping and polishing

After LPE growth of the active layer onto the substrate, the sample is cooled and taken out of the oven. At this stage, the sample is still covered with residue as a result of the solvent-solute vapours that have precipitated onto the sample surface during the cooling cycle of the oven. This residue can easily be cleaned off the sample using demineralised water. The surface morphology of the grown layer is typically uneven: the thickness of the grown layer varies across the sample due to different growth speeds towards the edges of the sample, with height differences of over 10 µm. Since an even layer thickness is required for the fabrication of waveguide lasers, the grown layers have to be levelled to the desired thickness as calculated in the previous paragraph. The as-grown layer thickness between $20 - 60$ µm, provides ample room for lapping (levelling) and polishing of the sample to the right thickness of typically $5 - 15$ µm.

The 1×1 cm^2 samples are overgrown only to a maximum of 85% of the area (refer to figure 2.5e), to prevent the addition of material onto the platinum wires and cracking, and to facilitate alignment of the sample with respect to the substrate upon which the active layer has been grown. For surface polishing, the sample is mounted onto a stainless-steel chuck using soft wax with a melting temperature of around 70 °C, and mounted on the polishing jig (Logitech PP-5), as shown in figure 2.9a. An autocollimator (Logitech LG2), with a precision of 2 arc-seconds, was used to align the mounted sample with respect to the lapping disk surface. The sample is then lapped using a pre-conditioned cast-iron lapping disk on a Logitech PM-5 machine (figure 2.9d). As an abrasive, 3-µm-sized calcined aluminum-oxide particles are used to maintain correct lapping conditions and reproducible speed. The lapping speed and quality is strongly dependent on the pressure applied to the sample. For our 1×1 cm^2 samples, the typically applied weight is 0.2 kg, or a pressure of approximately 2 N/cm^2, resulting in a lapping speed of approximately 3 µm/minute. Because of the high lapping speed,

this is a critical step in the fabrication of waveguides requiring careful inspection and measuring of the thickness after each (few) minute(s) of lapping. The thickness of the layer is monitored by using a Michelson interferometric microscope: by focussing onto the junction region between the active and substrate layers a fringe pattern is displayed, which is shifted across the junction depending on the height difference (figure 2.9c). Therefore, by counting the amount of shift relative to a ruler pattern, and multiplying by half of the filter wavelength of 550 nm, the active layer thickness can easily be calculated.

After the lapping process, taking roughly an hour, a polishing process is initiated by replacing the cast-iron lapping disk with a soft polyurethane disk and by replacing the lapping abrasive with a polishing suspension (Struers OP-U). The disk is again pre-conditioned to ensure flatness of the disk before the polishing procedure is started (figure 2.9e). The polishing procedure is a slow process with a polishing speed of 2 µm/hour for an applied pressure of 4 N/cm^2. During a process lasting several hours, at least $3 - 4$ µm of layer material is removed. Meanwhile, the active layer thickness is measured several times to prevent the removal of too much material. The resulting laser-grade polished, active layer has a root-mean-square surface roughness of 1.5 nm, which was determined using atomic force microscopy, and a surface curvature in the order of several meters [111]. After this polishing process, the sample is removed from the chuck by melting and cleaning-off of the wax and ready to be micro-structured.

A more elaborate discussion on the intricacies of the lapping and polishing process is provided by Geskus, for example that micro-cracks can occur during the lapping and polishing processes if too much pressure is applied, due to chipping-off of crystal parts [111].

End-facet lapping and polishing

After the micro-structuring of channel waveguides into the crystal layer, the channel waveguides are diced to the required length. The end-facet is diced at right angles to the structured waveguides using a high precision dicing saw (LoadPoint Ltd.) equipped with a F1230 diamond blade. This dicing blade, with a thickness of 30 µm, was used to dice the end-facets to a depth 300 µm with a relatively smooth finish to provide sufficient reflection during end-facet alignment prior to the lapping/polishing process. The separating cut was made with a standard TC300 (Thermocarbon Inc.) dicing blade. After dicing both end-facets, lapping and polishing is required to allow in-coupling of pump light and to allow attachment of dielectric mirrors for the laser experiments. The sample is therefore squeezed between pieces of common soda microscope glass, cut to roughly the same size as the sample using a diamond-tipped pen. A stack consisting of the sample holder, two pieces of soda glass, the sample, and another two pieces of soda glass are glued together using a rigid, transparent phthalate

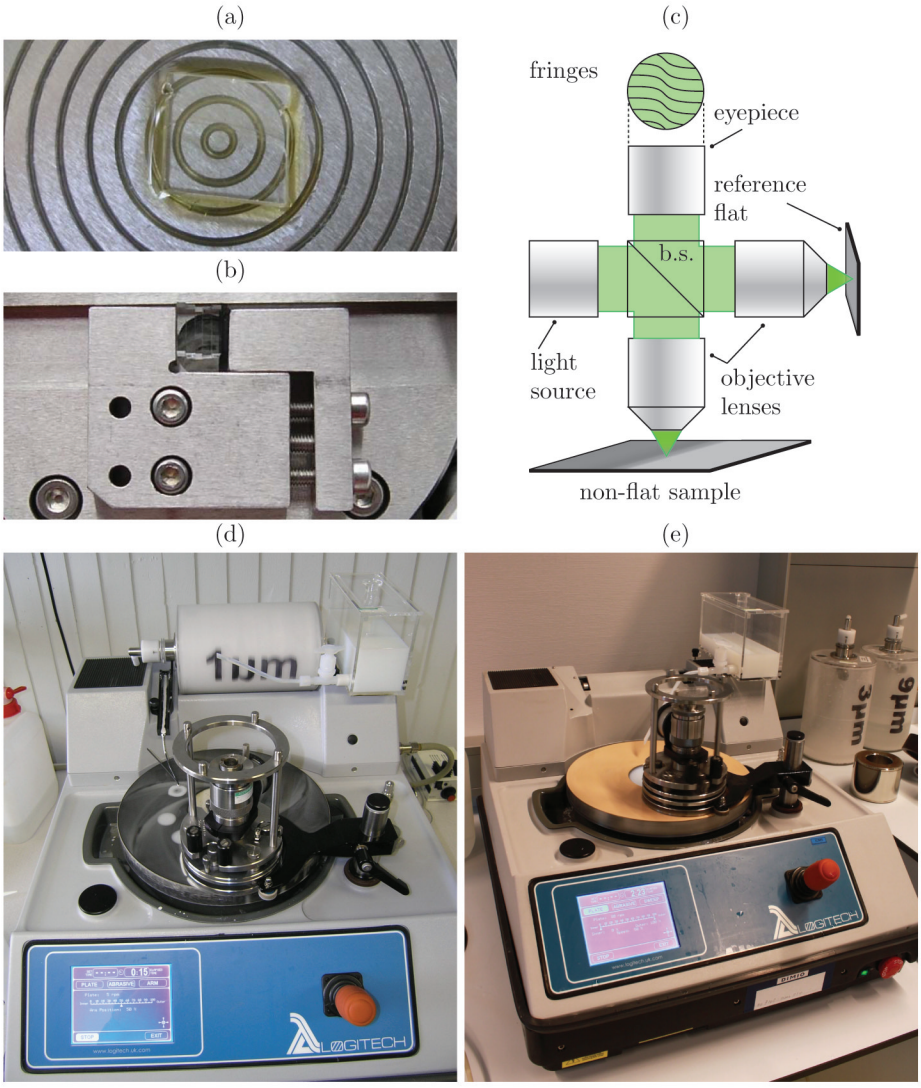

Figure 2.9 **Lapping and polishing of a double tungstate sample.** (a) A sample is mounted onto a flat chuck using soft wax, prior to surface polishing. (b) For end-facet polishing, a sample is squeezed and hard-waxed symmetrically between pieces of soda glass. (c) Monitoring of the planar layer thickness is performed using an interference microscope at 550 nm. (Adapted from [98]). Lapping and polishing of samples is performed using a (d) cast-iron disk and aluminum-oxide particles as an abrasive and (e) a polyurethane disk and a polishing suspension, respectively.

wax with a melting temperature of approximately 90 °C. The stack is heated to the wax melting temperature and cooled down to room temperature while pressing the stack together with a force of a few hundred grams, to obtain as thin wax layers as possible between the glass and sample. The sample holder, containing the glued-in sample/glass stack is subsequently mounted inside the jig, as displayed in figure 2.9b. Alignment with respect to the lapping/polishing disk surface is next performed using the reflection off the 300-µm-wide, relatively smooth, dicing facet, using a 633 nm helium-neon laser (the 'smooth' end-facet does not provide sufficient reflection allowing the use of the autocollimator). After alignment, the layer stack is lapped till the sample and all glass plates have a rough facet. Beyond this point, another several tens of µm are lapped away to make sure that any end-facet damage introduced by dicing is removed. The total amount of end-facet material removed is uncritical, since shortening of the channels by several tens of µm compared to the total length of the channels of several mm makes only a small fraction.

After lapping, a polishing process identical to the one described earlier is performed to obtain a laser-grade end-facet quality. Subsequently, the glass/sample stack is taken apart by re-heating to the wax melting temperature, and the sample is subsequently cleaned by citric acid (to remove wax traces), acetone and isopropanol prior to optical experiments.

2.4.2 Lithography and etching

After surface-polishing of the doped layers to laser-grade optical quality, the sample is ready to be micro-structured. A full description of the process is given in table 2.7. After cleaning with pure nitric acid and treatment of the surface using hexamethyldisilazane (HMDS), a layer of positive photoresist (Fujifilm OiR 908/35) is spun onto the prepared surface, yielding a resist layer with a thickness of up to 4 µm. A mask containing sets of waveguides with a width between 2.5 µm up to 30 µm was used to perform UV-lithography. An automated mask alignment system (EVG 620) was used for a flood exposure of the photoresist with a duration of 10 seconds. Since the mask alignment system is tuned to operate with 4-inch-sized wafers having a rather uniform thickness and since the used double tungstate samples are sized only 1×1 cm^2 with a nonuniform thickness (due to the uncontrollable LPE growth speed on the unpolished backside of the sample), the automated mask alignment function could not be used. Instead, a double tungstate sample was first put onto a sample holder and supported by standard cleanroom tissue to allow for some pressure compensation when the mask is put on top of the sample. Additional cleanroom tissue and pieces of glass were used to support the mask, which is designed to be in hard contact with the resist layer to prevent the occurrence of air gaps and consequently a reduction of resolution. The occurrence of Newton fringes provides a useful aid to verify the

Table 2.7 Lithography and etching process flow for the fabrication of ridge-type channel waveguides in co-doped double tungstate crystals.

Step	Process description
Preparation	
0	Pre-heat oven for step 3.7
Cleaning	
1.1	Cleaning in 100% HNO_3, 10 minutes
1.2	Quick-dump rinse + blow-drying using N_2
Preparing photoresist	
2.1	De-hydration bake, 5 minutes, 120 °C
2.2	Spin-coating of HMDS: 20 seconds, 4000 RPM
2.3	Spin-coating of photoresist (OiR 908/35): 20 seconds, 4000 RPM. Minimise time between applying resist and spinning to reduce edge beat.
2.4	Pre-exposure bake, 2 minutes, 95 °C
2.5	Wait 5 minutes before continuing
Performing the lithography	
3.1	Lithography at EVG620, using flat chuck. Support of the sample and mask by blue tissues and pieces of glass/wafer. The mask is put in place manually, and should be in contact with the sample, which is indicated by the presence of Newton fringes. The N_g optical axis is identified by making use of cross-polarizers and should align parallel to the waveguides on the mask.
3.2	Exposure, 10 seconds, using 'flood exposure' setting with 5 seconds of delay
3.3	Degassing: 5 minutes
3.4	Post-exposure bake, 1 minute, 120 °C
3.5	Standard development: 30 seconds bath 1, 25 seconds bath 2
3.6	Post-exposure bake: 10 minutes, 120 °C
3.7	Post-exposure bake + reflow in oven: 1 hour, 150 °C
3.8	Optical inspection of developed photoresist mask using microscope
Performing the etching	
4.1	Fix samples onto a glass wafer using thermal conductive paste
4.2	Perform argon ion-beam etching using the following settings (for an etch depth of 1.4 µm). Process time: 8 hours. Acceleration voltage: 350 V. Beam current: 20 mA. Sample inclination: 30 degrees.
Resist stripping	
5.1	Cleaning in 100% HNO_3, 10 minutes
5.2	Quick-dump rinse + blow-drying using N_2

contact between sample and mask. Alignment of the mask with respect to the sample is achieved by making use of cross-polarisers and a red bicycle light which does not cross-link the resist prior to exposure. In this way, the channels on the mask are aligned parallel to the N_g optical axis, as discussed in section 2.1.1. The alignment accuracy of this method is estimated to be within 3°. After exposure of the resist, standard development suited for the used resist, and several post-exposure bakes including reflow are performed. The reflow step is performed to guarantee a very smooth, hemispherical-shaped resist pattern, which reduces the effect of re-depositioning of etched material onto the channel sidewalls during the subsequent etching step [112]. The resulting channels defined in photoresist are visible in figure 2.10a, showing a microscopic top-view of a group of 10 channels with a width of $10 - 25$ µm.

Transfer of the resist pattern into the doped double tungstate planar waveguide layer is performed using argon-beam etching. Argon ions are accelerated towards the sample with an acceleration voltage of 350 V. Prior to hitting the target, the ions are electrically neutralised such that a highly directional, high-energy neutral argon atom beam is created, which physically etches any material placed in its path. The sample is mounted on a flat chuck which is tilted at an angle of 20°with respect to the incoming beam, in order to achieve the optimum etching rate and feature shape [113]. The chuck is rotated about its axis for the duration of the etching process to decrease sidewall roughness. An etching selectivity of 1:1 between resist and double tungstate material is realised as a result of the non-chemical process, such that the maximum etch depth into the double tungstate layer was limited by the thickness of the resist layer. In this work, ridge-type channel waveguides with an etch depth between $1.5-1.9$ µm have been produced. At first, an old argon-beam etcher of the MESA$^+$ cleanroom facility was used which had a low etching rate of 3 nm/minute due to having a small beam flux. Later, the etching process was kindly performed by Dr. Christos Grivas at the cleanroom facility of the University of Southampton with a modernised argon-beam etcher, resulting in higher etching speeds.

After etching of the double tungstate layers, the remainder of the photoresist is removed in a pure nitric acid cleaning step. The final fabrication steps are the overgrowth of the ridge-type channel waveguides with an undoped, pure $KY(WO_4)_2$ cladding layer (refer to section 2.2.3), followed by end-facet dicing, lapping and polishing (refer to section 2.4.1). A microscope image of the realised buried, ridge-type channel waveguides is shown in figure 2.10b, which displays channels with a width between $7.5-12.5$ µm, etched into a 6.5-µm-thick thulium-doped double tungstate planar waveguide layer.

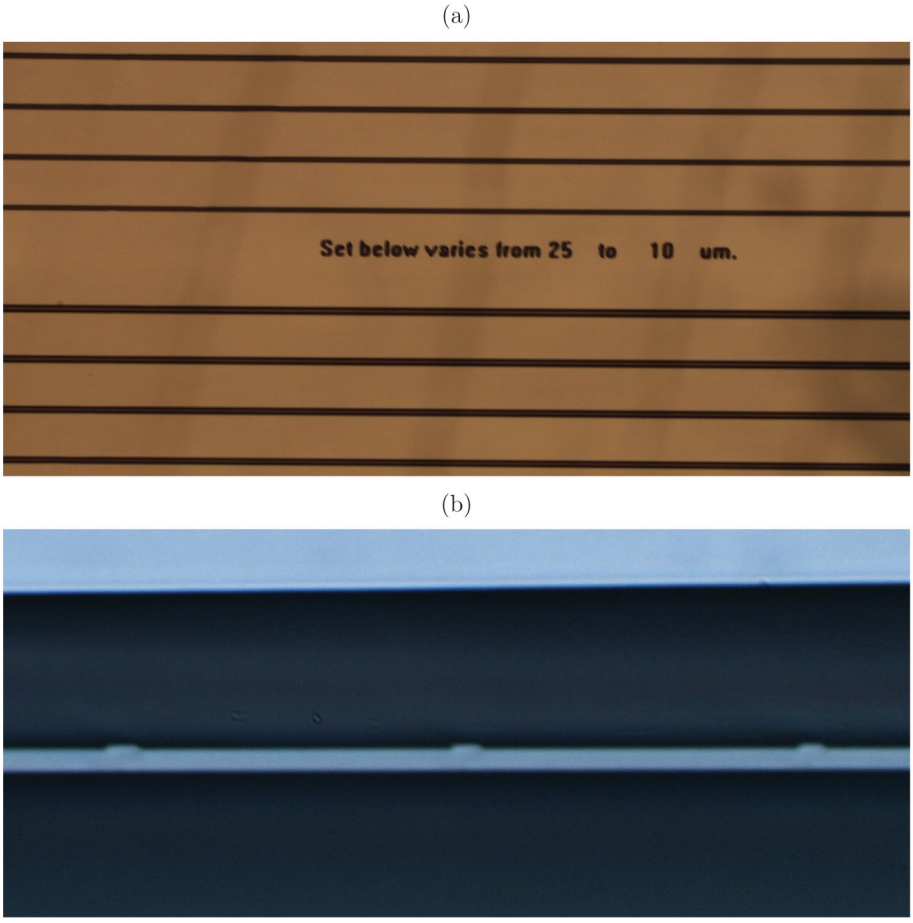

Figure 2.10 **Microstructuring of channel waveguides onto doped tungstate planar layers.** (a) Top-view image of channel waveguides defined in positive photoresist, prior to etching. On this particular sample groups of 10 channels with a width of $10 - 25$ µm were defined. (b) End-facet view of realised buried, ridge-type channel waveguides after overgrowth and end-facet dicing, lapping and polishing. The channels are clearly visible by illumination through the end-facet opposite to the end-facet focused at.

CHAPTER 3

Theoretical analysis

Apart from having the right materials and equipment at hand, laser theory is important for the realisation of powerful and efficient lasers. In this chapter, the theory of three-level lasers is explained, as well as the non-linear processes that take place as a result of the mutual interaction of thulium ions in doped media. In chapter 4, we will use this theory to determine various properties of the waveguide lasers such as the propagation loss and the excited state lifetime, and to compare the theoretical with the experimental performance in terms of threshold, power and efficiency.

3.1 Interaction between light and rare-earth-doped media

3.1.1 Rare-earth elements

The rare-earth elements are a group of 14 lanthanide elements with atomic numbers 58 – 71 in the periodic table of elements. Besides these elements, scandium with atomic number 21, yttrium with atomic number 39 and lanthanum with atomic number 57 are also considered to be part of the rare-earth elements. World-wide demand for rare-earth metals has rapidly increased over the past decades due to the growing electronics industry. The production of rare-earth metals used to be dominated by China despite of having only 35% of the known available resources [114]. However, large stockpiles of rare-earth metals have recently been discovered beneath the water surface that may be exploited in the near future [115]. Rare-earth metals such as neodymium, praseodymium, and gadolinium are in high demand for high quality magnets in speakers and high-power electric motors. Yttrium is an element which is frequently encountered in laser materials, such as yttrium-aluminum-garnet (YAG), ytterium-lithium-fluoride (YLF), and the material being the subject of this thesis: potassium-double-tungstates ($KRe^{3+}(WO_4)_2$), where 'Re^{3+}' can be yttrium, gadolinium, lutetium and thulium.

The electronic transitions of the rare-earth ions usually take place by electrons in the 4f shell, which are partially shielded from the host lattice by electrons

Table 3.1 Common absorption and emission wavelengths of several rare-earth ions. Some of the ions can be used to create three- of four-level lasers. For example, the Nd^{3+} ion acts as a four-level laser when pumped at 800 nm, and emitting at 1060 nm, while emission at 880 nm is a three-level scheme.

Rare-earth ion	Absorption wavelength	Emission wavelength
Pr^{3+}	450 nm	480, 520, 640 nm
Nd^{3+}	800 nm	880, 1060, 1330 nm
Yb^{3+}	980 nm	1020 nm
Er^{3+}	980, 1480 nm	1550 nm
Tm^{3+}	800 nm	1900 nm
Ho^{3+}	1900 nm	2100 nm

in the higher shells. Consequently, the host material has only a small effect on the electronic properties of the rare-earth ions, such as the optical transition wavelengths, and optical absorption and emission cross-sections of the rare-earth ions. Furthermore, the weak interaction between the host lattice and the electrons in the 4f shell facilitates long lifetime of the energy levels that are involved in optical transitions. These favourable electronic and optical properties of the rare-earth ions when incorporated in a suitable host material make these suitable for creating optical amplifiers and lasers. Energy conversion from one wavelength to another is achieved by pumping the ions from the ground-state to a higher energy state, followed by loss of energy via rapid phonon relaxation to a lower energy level. Relaxation back to the ground level is facilitated by the emission of a photon, via spontaneous emission, or, in case of an amplifier or laser, via stimulated emission. The optical transitions of a large number of doubly and triply ionised rare-earth elements were summarised by Dieke [116]. Some of the common absorption and emission wavelengths spanning the visible to the infrared range of rare earths are summarised in Table 3.1.

The rare-earth ion thulium

In this thesis, we will focus on the rare-earth element thulium (atomic number 69), with an emission wavelength of around 1.9 µm. In unbound state, its electronic configuration is $[Xe]4f^{13}6s^2$. Once incorporated in a host material it is usually present in a trivalent state Tm^{3+}, with an electronic configuration of $[Xe]f^{12}$. The incompletely filled 4f shell is responsible for its specific absorption and emission spectrum, which differs only slightly between different host materials due to the

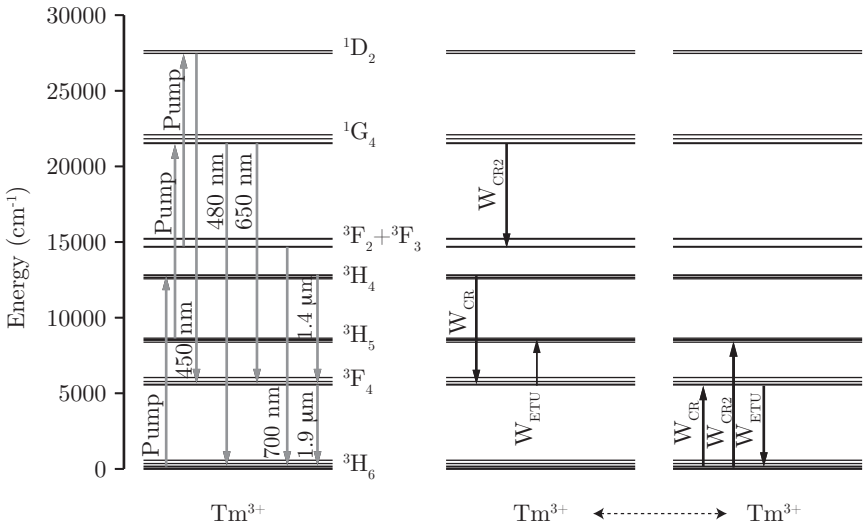

Figure 3.1 The energy levels of the thulium ion and different energy transitions. In the figure on the left, the energy of the manifolds and the wavelengths for some important radiative transitions are indicated. The pump wavelength is around 800 nm, and excites ions from the ground state into the $^3H_4$ manifold, or even higher energy levels via excited-state absorption as indicated in the left diagram. In the right diagram, where a dashed arrow indicates dipole-dipole interaction between two thulium ions, two exothermic cross-relaxation processes W_{CR} and W_{CR2} have been indicated, as well as an exothermic up-conversion process W_{ETU}.

shielding effect of the completely filled 5s and 5p shells, surrounding the 4f shell. Each of the free ion energy levels can be described as $^{2S+1}L_J$ in the Russell-Saunders notation, with S, L and J representing the spin angular momentum, orbital angular momentum, and total angular momentum, respectively. Due to interaction with the crystal field of the potassium tungstate host material, the thulium free ion energy levels split into a total of (2J+1) Stark sub-levels [117]. Thulium is a complex ion with many energy levels and energy transitions. Figure 3.1 shows the different energy levels of thulium in a $KLu(WO_4)_2$ host material, up to an energy of 30.000 cm^{-1} corresponding to a wavelength of approximately 330 nm, which is the lower wavelength limit of optical transparancy of the double tungstate host material. The ground manifold of thulium is the $^3H_6$ level, from which it is usually pumped at 800 nm into the $^3H_4$ excited manifold at around 12.500 cm^{-1}. Possible excited-state absorption at 800 nm occurs from the $^3H_5$ excited state into the $^1G_4$ excited manifold and from the $^3F_2$ excited manifold into the $^1D_2$ excited manifold. From the $^3H_4$ excited manifold, a radiative transition

at 1.4 µm terminates in the $^3F_4$ excited manifold. This $^3F_4$ manifold is the origin of fluorescence around 1.9 µm, which terminates in the ground manifold. Other radiative transitions originate from the $^1D_2$ excited manifold into the $^3F_4$ manifold at 450 nm, and from the $^1G_4$ manifold into the ground manifold at 480 nm. These transitions are responsible for the typical blue fluorescence visible in a thulium-doped host material. An important process taking place in thulium ions is cross-relaxation (CR), in which two ions are involved that are in close vicinity; one ion in the $^3H_4$ excited manifold transfers part of its energy to an adjacent ion in the $^3H_6$ ground manifold, resulting in both ions ending up in the $^3F_4$ manifold. This process is indicated in Figure 3.1 by W_{CR}. This process is beneficial for the development of lasers pumped at 800 nm and operated at 1.9 µm, since each pump photon at 800 nm is converted to a maximum of two photons at a frequency of 1.9 µm, leading to a quantum efficiency of up to 2. Besides this CR process, another CR process W_{CR2} is also indicated in Figure 3.1, as well as an energy-transfer up-conversion (ETU) process W_{ETU}. Besides these three processes which are exothermic, other CR and ETU processes are mentioned in the literature which are endothermic [60, 117] and therefore require phonon energy for the transitions to happen. Besides the 800 nm pump transition, thulium can also be in-band-pumped directly into the $^3F_4$ manifold at 1.8 µm. In either case, thulium acts as a (quasi) three-level system.

3.1.2 Emission and absorption of light

For an enclosed system in thermal equilibrium at a temperature T, the radiation density $\rho(\nu)$ is defined according to Planck's law of blackbody radiation:

$$\rho(\nu) = \frac{8\pi n^3 h\nu^3}{c^3} \frac{1}{e^{h\nu/k_B T} - 1} \tag{3.1}$$

where $\rho(\nu)$ is the radiation density per unit frequency $\left[\mathrm{Js/cm^3}\right]$, k_B is Boltzmann's constant, c is the vacuum speed of light and n is the refractive index of the medium. The quantity $h\nu$ is the energy of a photon with a frequency ν, where h is Planck's constant. This energy $h\nu$ equals the energy difference between two levels E_0 and E_1 when the transition from energy level E_1 to E_0 is accompanied by the emission of a photon.

When a large collection of ions is considered in a thermal equilibrium, the population density between two energy states with energy E_0 and E_1, according to equation 3.14, is given by

$$\frac{N_1}{N_0} = \frac{g_1}{g_0} \exp\left[(E_0 - E_1)/k_B T\right], \tag{3.2}$$

where N_1 and N_0 are the population densities, $\left[\mathrm{cm^{-3}}\right]$, of the ions in energy states E_1 and E_0, with degeneracies g_1 and g_0, respectively. Interaction between

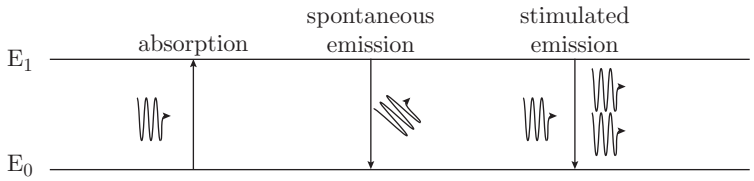

Figure 3.2 Absorption, spontaneous and stimulated emission in a two-level system. Absorption of a photon with energy $\Delta E = E_1 - E_0$ excites the ion from the E_0 ground state into the E_1 excited state (left). De-excitation of the ion can take place through spontaneous emission of a photon with energy $\Delta E = E_1 - E_0$ in random direction (centre), or stimulated emission induced by a photon with energy $\Delta E = E_1 - E_0$ (right). In the latter case, the emitted photon has the same phase and direction as the stimulating photon.

the ions in thermal equilibrium is possible via electromagnetic radiation, in the form of absorption, spontaneous emission, and stimulated emission, such that the population densities N_1 and N_0 remain unaltered. Figure 3.2 depicts these three forms of interaction. The absorption of electromagnetic radiation and the related change per unit time and volume of the population density dN_0/dt is proportional to the population density N_0 and the radiation density $\rho(\nu)$, and can be written as:

$$\frac{dN_0}{dt} = -B_{01}\rho(\nu)N_0 \tag{3.3}$$

where B_{01} is the Einstein coefficient of absorption with dimensions of $\left[\mathrm{cm}^3/\mathrm{Js}^2\right]$.

A similar expression can be written for stimulated emission through the presence of a radiation density $\rho(\nu)$, depleting the upper state with a rate (per unit time and volume):

$$\frac{dN_1}{dt} = -B_{10}\rho(\nu)N_1 \tag{3.4}$$

where B_{10} is the Einstein coefficient of stimulated emission with dimensions of $\left[\mathrm{cm}^3/\mathrm{Js}^2\right]$.

The process of spontaneous emission is stimulated by zero-point fluctuations of the electric field of the vacuum. The rate of spontaneous emission is dependent only on the population density N_1 and the decay rate constant A_{10}:

$$\frac{dN_1}{dt} = -A_{10}N_1 \tag{3.5}$$

where A_{10} is a constant with dimensions of $\left[\mathrm{s}^{-1}\right]$.

Since the system is assumed to be in thermal equilibrium, the population densities N_0 and N_1 of the two levels remain unchanged. This means that the depletion of the lower level caused by absorption of electromagnetic radiation

equals the combined rate of spontaneous and stimulated emission depleting the upper level:

$$B_{01}\rho(\nu)N_0 = A_{10}N_1 + B_{10}\rho(\nu)N_1 \tag{3.6}$$

Combining equations 3.2 and 3.6 yields an expression for the radiation density $\rho(\nu)$:

$$\rho(\nu) = \frac{A_{10}/B_{10}}{(g_0/g_1)(B_{01}/B_{10})\exp\left[h\nu/k_BT\right])} \tag{3.7}$$

where we have used that the energy difference $\Delta E = E_1 - E_0$ equals the photon energy $h\nu$ of an emitted or absorbed photon.

On comparing equation 3.7 to Planck's equation of blackbody radiation, eqn. 3.1, we arrive at the Einstein relations:

$$g_0B_{01} = g_1B_{10} \tag{3.8}$$

$$A_{10} = \frac{8\pi n^3 h\nu^3}{c^3}B_{10} \tag{3.9}$$

If level 1 with energy E_1 can only decay by radiative emission to level 0 with energy E_0 , then the decay rate constant A_{10} is the Einstein coefficient of spontaneous emission, such that $A_{10} = 1/\tau_1$.

Effective emission and absorption cross-sections

The Einstein coefficients A_{10}, B_{01} and B_{10} can be related to the absorption (σ_a) and emission (σ_e) cross-sections [118, 119]:

$$\sigma_a(\nu) = B_{01}g_a(\nu)\frac{h\nu}{c/n} \tag{3.10}$$

$$\sigma_e(\nu) = B_{10}g_e(\nu)\frac{h\nu}{c/n}, \tag{3.11}$$

where $g_a(\nu)$ and $g_e(\nu)$ are the absorption and emission spectral line shape distributions, describing the atomic transitions. Since the absorption and emission cross-sections are related through the Einstein coefficients, calculation of the absorption cross-section is possible from the emission cross-section or vice versa. This procedure is a result from McCumber theory [118]. A relation between the emission cross-section and the radiative lifetime is detailed in the theory of Füchtbauer-Ladenburg [120]. Though these theories are an important result of the Einstein coefficients, we will not further discuss these theories in this thesis.

The cross-sections defined above have units of meters squared. By multiplying the absorption cross-section by the population density N_0 of the lowest energy level, an absorption coefficient α is obtained:

$$\alpha(\nu) = N_0\sigma_a(\nu). \tag{3.12}$$

The absorption coefficient is used in the Lambert-Beer law of absorption to calculate the absorption of a beam of light with irradiance $I(\nu, z)$ propagating through an absorbing medium according to

$$\frac{dI(\nu, z)}{dz} = -\alpha(\nu)I(\nu, z). \tag{3.13}$$

Similar to the absorption coefficient and the Lambert-Beer law of absorption, equations for the gain in a material can be derived by replacing the absorption cross-section by the emission cross-section in the equations.

By measuring the absorption of light in a medium, the absorption coefficient and therefore the cross-sections can be calculated, if the dopant concentration is known. A solid-state laser gain medium exhibits Stark level manifolds rather than isolated optical transitions between a single lower and a single upper energy level in the simplified view of figure 3.2. Therefore, in a practical measurement, many electronic sublevels of an energy level may contribute to the optical absorption and emission, especially because the Stark levels in a manifold are spectrally broadened by the electric fields inside a host material and have slightly different energy depending on the local conditions in the host material (such as local dopant concentration and temperature). Especially in glasses, the contribution from the different electronic sublevels of a manifold is broadened.

The population fraction across a manifold with multiple Stark levels in thermal equilibrium can be calculated according to the Boltzmann distribution. The population fraction is defined as the ratio of the population density in a Stark level over the total population density in the manifold. The population fraction f_i of a Stark sub-level i with an energy of E_i and degeneracy g_i is given by the Boltzmann distribution:

$$f_i = \frac{g_i \exp\left[(E_0 - E_i)/k_B T\right]}{\sum_j g_j \exp\left[(E_0 - E_j)/k_B T\right]}, \tag{3.14}$$

where E_0 is the energy of the lowest Stark sub-level in the manifold, and j is the total amount of Stark sub-levels in the manifold with degeneracy g_j, T is the temperature and k_B is Bolzmann's constant.

A practical measurement of the absorption or emission coefficient is the result of the different population densities of the different Stark levels in a manifold and the individual transition cross-sections between these levels. The calculated absorption or emission cross-section for a certain frequency from the measured frequency-dependent absorption or emission coefficient is the sum of all transition cross-sections at this frequency multiplied by the probability of these transitions, according to:

$$\sigma_{\mathrm{a,eff}}(\nu) = \sum f_i \sigma_{\mathrm{a}}(\nu) \tag{3.15}$$

$$\sigma_{\mathrm{e,eff}}(\nu) = \sum f_i \sigma_{\mathrm{e}}(\nu), \tag{3.16}$$

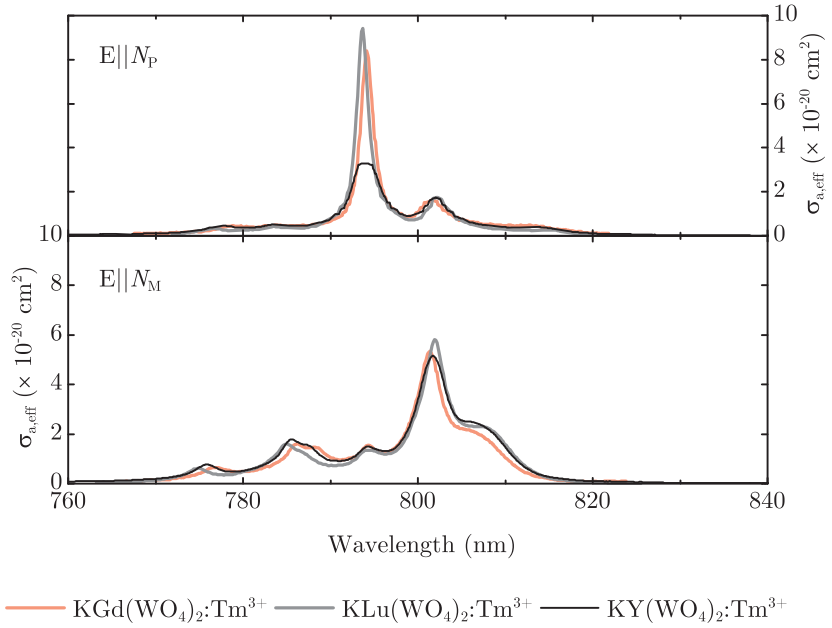

Figure 3.3 Effective absorption cross-sections around 800 nm for Tm-doped double tungstates. $KGd(WO_4)_2$ (red line, [58]), $KLu(WO_4)_2$ (gray line, [40]) and $KY(WO_4)_2$ (black line, [39]). The absorption cross-section is highest, and with the narrowest linewidth, for a polarisation of $E \| N_p$.

and these are called the effective absorption and emission cross-sections, with f_i the transition probability as calculated from the Boltzmann distribution. Therefore, the effective emission and absorption cross-section are temperature-dependent. For the absorption of light inside a medium, it follows from equations 3.12, 3.13 and 3.15:

$$I(\nu, z) = I(\nu, 0)e^{-\alpha(\nu)z} = I(\nu, 0)e^{-N_0\sigma_{a,\mathrm{eff}}(\nu)z} \tag{3.17}$$

The effective absorption cross-sections around 0.8 µm and 2 µm and emission cross-sections around 2 µm of thulium in $KY(WO_4)_2$ [39], $KLu(WO_4)_2$ [40], and $KGd(WO_4)_2$ [58], are shown in figures 3.3 and 3.4.

The lifetime of an ion in an excited state

An ion excited to a higher energy level can decay radiatively, via a decay path of spontaneous emission as discussed before, or via a non-radiative decay path of multi-phonon relaxation. The total decay rate constant is the sum of the rate constants of the two decay processes: $A_{\mathrm{tot.}} = A_{\mathrm{rad.}} + A_{\mathrm{non-rad.}}$. The decay

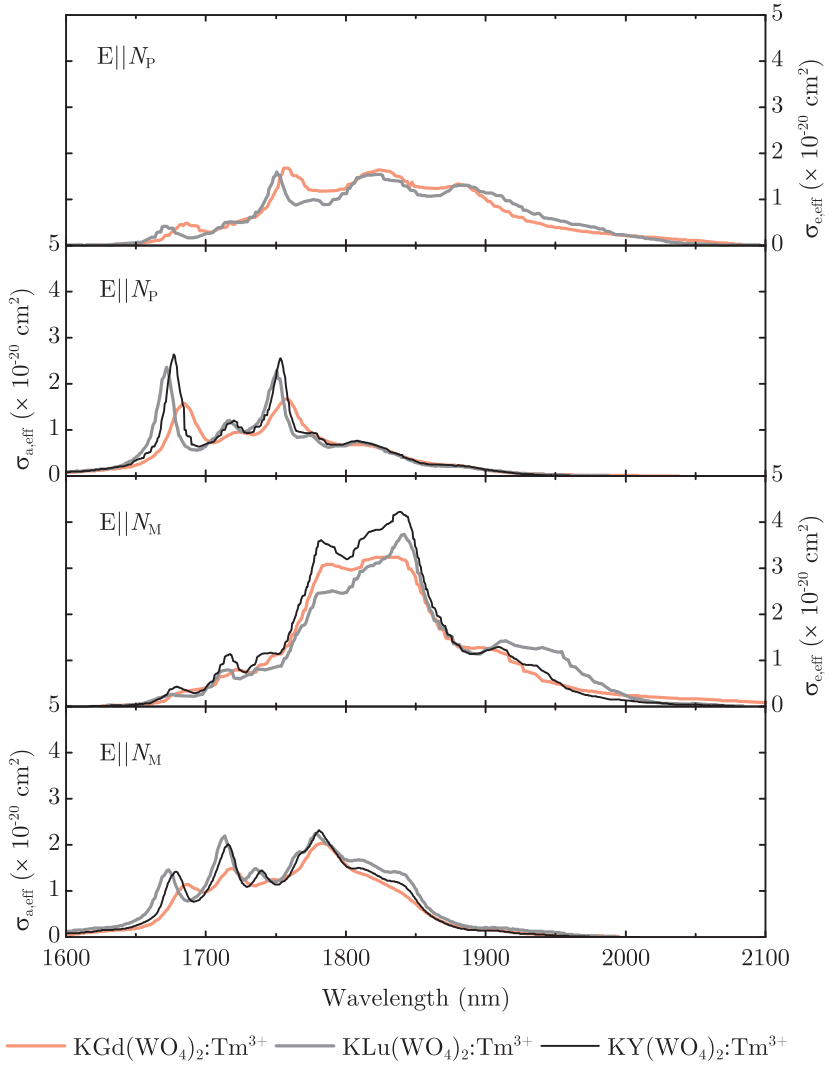

Figure 3.4 Effective absorption and emission cross-sections around 2 µm for Tm-doped double tungstates. $KGd(WO_4)_2$ (red line, [58]), $KLu(WO_4)_2$ (gray line, [40]) and $KY(WO_4)_2$ (black line, [39]).

rates are proportional to the population density in the excited level, since the decay rate is the product of the rate constants and the population density. The spontaneous decay rate constant $A_{\text{rad.}}$ is given by equation 3.5, and the phonon relaxation rate constant is given by [121]:

$$A_{\text{non-rad.}} = C\left[\frac{1}{\exp(\hbar\omega/k_BT)-1}+1\right]^p \exp^{-\alpha\Delta E}, \tag{3.18}$$

where ω is the phonon angular frequency and p is the number of phonons necessary to bridge the energy gap ΔE. Both C and α are host-dependent parameters. Large differences in phonon relaxation rates between different materials can be a result of the phonon energy and the energy gap. For example, in oxides such as tungstates, the phonon relaxation rate is stronger than in fluorides because of the larger phonon energy, requiring fewer phonons to bridge the energy gap ΔE. Typically, if fewer than five phonons are required to bridge the energy gap, the non-radiative decay becomes the dominant decay mechanism [122].

The sum of the total decay rate, radiative and non-radiative, of a system in an excited state can be determined via luminescence decay measurements of the spontaneous emission at a wavelength corresponding to a transition originating from the level of interest. In the absence of the energy-transfer processes such as cross-relaxation, the population density as a function of time for an ensemble of excited ions decaying to the ground state follows an exponential curve. In such case, the time it takes for the population density of the excited state to decrease to $1/\text{e} = 37\%$ of the original population is defined as the luminescence lifetime τ. The luminescence decay rate constant $1/\tau = 1/\tau_{\text{rad.}} + 1/\tau_{\text{non-rad.}}$ is the sum of the radiative and non-radiative decay rate constants. The luminescence lifetime equals the radiative lifetime in case no other processes than spontaneous (radiative) emission are present. In chapter 4, luminescence decay measurements are performed on thulium-co-doped samples to determine the lifetime of the $^3\text{F}_4$ upper laser level. In these experiments, a thulium-doped channel waveguide was excited via quasi-continuous-wave pumping, and the luminescence intensity was measured as a function of time. From the slope of the logarithmic intensity-over-time curves, the luminescence lifetime can be determined.

3.1.3 Energy transfer between rare-earth ions

Besides the emission and absorption of photons by individual ions and multi-phonon relaxation, energy transfer *between* rare-earth ions in a doped medium can also take place through dipole-dipole interactions (and even higher-order multipole interaction). Dipole-dipole interactions manifest themselves between two ions and are strongly dependent on the dopant concentration since the inter-ionic distance determines the dipole-dipole strength. The interaction strength rapidly decreases with the inverse sixth power of the separation distance between the ions.

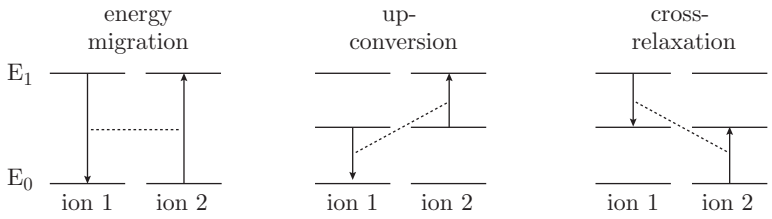

Figure 3.5 Dipole-dipole energy transfer processes. These transfer processes require two ions in sufficient close vicinity as the interaction strength decreases to the sixth power with increasing distance. Energy migration (left) is a process where one donor ion transfers its energy to another ion in such a way that their energy states are swapped. Energy-transfer up-conversion (center) is a process where the energy of a donor ion is used to excite an excited acceptor ion into an even higher energy state. Cross-relaxation (right) is an energy-transfer process where a donor ion in an excited state and an acceptor ion in the ground state both end up in some intermediate energy state.

There are several types of dipole-dipole interaction, which each have different effects on the excitation state of individual ions and the energy distribution within a doped medium. Different types of energy transfer are displayed in figure 3.5. When one ion simply transfers its energy to another ion such that the energy states of the two ions of the same type are swapped, the dipole-dipole interaction is called energy migration. In case of energy migration, the amount of ions in their different energy states are unchanged, but the distribution of energy among the ions in the crystal is.

Another type of dipole-dipole energy transfer is up-conversion, where a donor ion in an excited state donates its energy to an acceptor ion. The acceptor ion is subsequently excited to a higher energy state, whereas the donor ion ends up in a lower energy state.

A third energy-transfer process is cross-relaxation, where an accepter ion in the *ground state* is excited to a higher, intermediate state between the ground state and the original excitation energy level of the donor ion. The donor ion will end up in a lower energy state, which is not necessarily the same state as the acceptor ion is excited into. As figure 3.1 indicates, the thulium ion has a number of possible cross-relaxation channels [117], as well as several energy-transfer up-conversion channels [123]. In the thulium system, the cross-relaxation process has a beneficial effect in the sense that for each pump photon absorbed, two ions end up in the upper laser level. However, cross-relaxation energy transfer may be detrimental to the gain in other rare-earth systems in case the upper laser level is depopulated or the lower laser level is populated.

In general, dipole-dipole energy-transfer processes can be beneficial or detrimental to gain in rare-earth-ion-doped media. Energy migration towards unwanted impurities can for example severely decrease the gain, whereas at the same time the detrimental effects of spatial hole burning can be mitigated by energy migration, leading to better used gain instead. Energy-transfer up-conversion can be exploited in up-conversion lasers to obtain laser radiation at a shorter wavelength than the pump wavelength [124], or to deplete the lower laser level.

Quite a number of macroscopic, as well as microscopic models describing dipole-dipole interactions in gain media have been developed, but application of these models to rare-earth systems with varying dopant concentrations, host materials and ion types to explain energy-transfer rates proves difficult. A theory that is able to describe energy-transfer processes in rare-earth doped media with realistic dopant concentrations is the theory by Zubenko [125], which combines the theories of Grant [126], and Zusman [127], in a single model. However, all of these models treat all ions equally, which is not generally the case for ions embedded in a host material because of non-homogeneous distribution of active ions. Agazzi has shown that these models tend to break down when modelling a gain medium where several classes of ions are present, such as strongly quenched ions due to clustering of impurity ions or due to the absence of neighbouring impurity ions, in amorphous host such as erbium-doped Al_2O_3 [26, 128] or thulium-doped Al_2O_3 [129]. In a crystalline host such as described in this thesis, clustering of ions is not an issue such as in glass materials. However, a class of ions in the crystal can exist that have a large numbers of impurity neighbouring ions compared to a class of rather isolated impurity ions. The model described by Agazzi can be applied to distinguish between these two classes of ions.

The macroscopic cross-relaxation rate parameter W_{CR} can be described as [26, 125]:

$$W_{\mathrm{CR}} = \frac{\pi^2}{3}\sqrt{C_{\mathrm{DA}}C_{\mathrm{DD}}}N_d, \tag{3.19}$$

where C_{DA} and C_{DD} are parameters describing the microscopic donor-acceptor (cross-relaxation) and donor-donor (energy migration) energy-transfer processes, respectively, and N_d is the thulium dopant concentration.

3.2 Rare-earth lasers

3.2.1 Types of lasers

Depending on the ion and the configuration of its energy levels, a laser can act as a four-level, a three-level or a quasi-three-level laser, as indicated in Figure 3.6. A true four-level laser is operated by pumping the ions from the ground level into a higher energy manifold. A rapid non-radiative transition then populates the upper laser level, from which stimulated emission occurs to a lower level, located

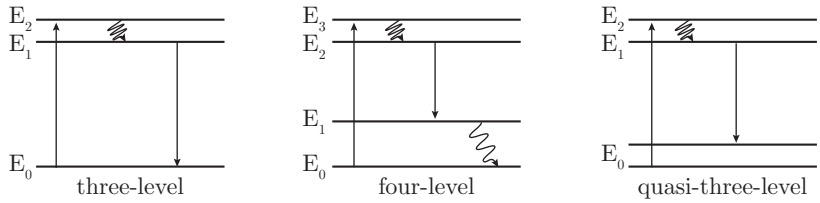

Figure 3.6 Overview of the energy schemes of (quasi-)three-level and four-level lasers. In a three-level laser scheme (left diagram), the pump level is pumped directly from the ground level. From the pump level, rapid multi-phonon relaxation takes place which populates the upper laser level, from which stimulated emission takes place which terminates in the ground level. In this type of laser, the highest pump intensity is required due to the required $> 50\%$ population inversion between the upper laser level and the ground level. In a four-level laser scheme (center diagram), the lower laser level is an excited level which is rapidly depopulated to the ground level by multi-phonon relaxation. The level of inversion needed in a four-level laser (one more excitation in the upper laser level compared to the lower laser level) is therefore much easier achieved, which results in a low pump threshold. In a quasi-three-level laser scheme (right diagram), the lower laser energy level is a high Stark level of the ground manifold. Since the population density of a high Stark level is less than the population density of a low Stark level, due to the Boltzmann distribution, it is easier to achieve population inversion between the upper and lower laser level, compared to a true three-level laser.

above the ground level. The lower laser level is depopulated to the ground level by another rapid non-radiative transition, which eliminates reabsorption of laser radiation and reduces the threshold. An example of a four-level laser is an 800-nm-pumped neodymium laser emitting at 1060 nm.

A three-level laser is operated by pumping from the ground level into a higher energy manifold which is depopulated by rapid non-radiative transition into the upper laser level. Laser radiation is generated by stimulated emission from the upper laser level into the ground level. Significant reabsorption of the laser radiation increases the pump threshold and required inversion: more than 50% of the ions need to be excited to reach threshold. Therefore a high pump intensity is required.

A quasi-three-level laser is similar to a three-level laser but the subtle difference is that the splitting of the ground manifold allows pumping from the lowest Stark level of the ground manifold, while stimulated laser radiation terminates at an elevated Stark level of the ground manifold. This reduces the required

inversion and therefore the pump threshold, as compared to a true three-level laser. An example of a quasi-three-level system is an Yb^{3+} laser pumped at 981 nm, while lasing occurs at 1025 nm. However, when pumping this system at 934 nm and generating laser radiation at the central line corresponding to 981 nm, this system its getting closer to a true three-level system since the required population inversion is almost 50% [51].

For a quasi-three-level laser, temperature is an important parameter that influences the threshold, since an elevated temperature gives rise to an increase of the population fraction of the lower laser Stark level, which increases the reabsorption of laser light and therefore the pump threshold. The population fraction across a manifold with multiple Stark levels in thermal equilibrium can be calculated according to the Boltzmann distribution of equation 3.14.

3.2.2 Thulium laser

Figure 3.7 shows various fluorescence, multi-phonon relaxation, cross-relaxation and energy-transfer up-conversion processes for the thulium system, of which the rate equations are as follows:

$$\frac{dN_3}{dt} = R_p - W_{\mathrm{CR}} N_3 N_0 - \frac{N_3}{\tau_3} \tag{3.20}$$

$$\frac{dN_2}{dt} = W_{\mathrm{ETU}} N_1^2 + \beta_{32}\frac{N_3}{\tau_3} - \frac{N_2}{\tau_2} \tag{3.21}$$

$$\frac{dN_1}{dt} = 2W_{\mathrm{CR}} N_3 N_0 - 2W_{\mathrm{ETU}} N_1^2 - \frac{N_1}{\tau_1} + \beta_{21}\frac{N_2}{\tau_2} + \beta_{31}\frac{N_3}{\tau_3} \tag{3.22}$$

$$N_0 = N_{\mathrm{Tm}} - \sum_{i=1}^{3} N_i \tag{3.23}$$

Here, the terms for stimulated emission have been omitted. R_p is the pump rate per unit volume from the ground manifold (0) into level 3. The terms N_i/τ_i account for the spontaneous decay rate of level i, and β_{ij} is the branching ratio of the spontaneous transition $i \rightarrow j$. The terms accounting for the energy transfer rate, W_{CR} and W_{ETU}, describe the cross-relaxation and up-conversion energy transfer processes between two ions, respectively. The total population density $N_{\mathrm{Tm}} = \sum_{i=0}^{3} N_i$ equals the sum of the population density of all levels.

When simulating the behaviour of a thulium laser based on a double tungstate host material, one can significantly simplify the level system of figure 3.7. One is the elimination of the $^3\mathrm{H}_5$ manifold from the equations, and the reason for this is the lifetime of the $^3\mathrm{H}_5$ manifold, which has a lifetime shorter than 30 µs [56], leading to rapid de-excitation of the $^3\mathrm{H}_5$ manifold to the $^3\mathrm{F}_4$ upper laser manifold. The cross-relaxation process W_{CR} becomes more dominant as the

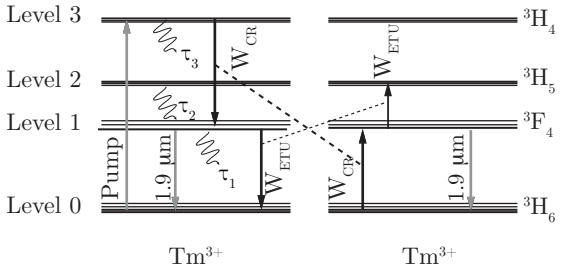

Figure 3.7 Energy levels and optical transitions of a thulium ion. The system is pumped from the $^3H_6$ ground manifold (level 0), into the upper pumped level, $^3H_4$, (level 3). This level is depopulated by an exothermic cross-relaxation process W_{CR} into the upper laser level and via non-radiative decay into level 2. The intermediate level 2 ($^3H_5$) is depopulated rapidly by non-radiative decay. Laser action is taking place from the $^3F_4$ manifold (level 1) back into the ground manifold. An exothermic energy-transfer up-conversion process W_{ETU} is also shown.

thulium dopant concentration increases, which ensures rapid population of the $^3F_4$ upper laser level [56, 123]. As a result of the rapid population of the upper laser level due to cross-relaxation, the pump rate from the ground manifold into level 3 can be simplified as if it directly populates the upper laser level N_1. As a result of the cross-relaxation rate, the quantum efficiency η_q, defined as the efficiency of the number thulium ions excited into the upper laser level for each pump photon absorbed, reaches a value of up to 2. In the following sub-section, this simplified set of rate equations, is used to derive a set of equations that describe the behaviour of the thulium laser, by taking into account the cross-relaxation through the quantum efficiency. The energy-transfer up-conversion process de-excites one ion in the upper laser level to the ground state and excites another ion to the $^3H_5$ level. Due to rapid multi-phonon relaxation from the $^3H_5$ level into the upper laser level, the decrease of excited ions in the upper laser level is limited to one ion per ETU process.

3.2.3 Steady-state laser behaviour

A set of rate equations describing the laser dynamics of three-level lasers is described below, by considering only the upper laser level which is rapidly populated from the pumped level. A separate equation for the photon balance in the cavity is needed. The rate equations follow the notation of Svelto [130].

The population density in the pumped level is considered to decay extremely fast into the first excited level N_1, such that the pump rate R_p can be assumed

to directly populate the first excited level. This simplification allows to write only the time-dependent population density N_1 and total photon number Φ in the laser cavity:

$$\frac{dN_1}{dt} = R_p - \frac{c}{V}(\sigma_{e,\text{eff}} N_1 - \sigma_{a,\text{eff}} N_0)\Phi - \frac{N_1}{\tau_1} \tag{3.24}$$

$$\frac{d\Phi}{dt} = V_a \frac{c}{V}(\sigma_{e,\text{eff}} N_1 - \sigma_{a,\text{eff}} N_0)\Phi - \frac{\Phi}{\tau_c}, \tag{3.25}$$

where the total dopant concentration $N_T = N_0 + N_1$ is the sum of the population density of all levels. In these equations, the effective absorption and emission cross-sections are indicated by $\sigma_{a,\text{eff}}$ and $\sigma_{e,\text{eff}}$, respectively, and c is the vacuum speed of light. $V = V_a l_{opt}/l_{cr}$ and V_a are the mode volume in the entire laser cavity and in the active medium, respectively. The pump rate,

$$R_p = \eta_p \eta_q P_p / h\nu_p A_{\text{cr}} l_{cr}, \tag{3.26}$$

is a function of the pump absorption efficiency η_p, the quantum efficiency η_q, the pump power P_p and the energy of a pump photon $h\nu_p$, the cross-sectional area A_{cr} of the active medium and length in the active medium l_{cr} over which pump light is absorbed. It is assumed in this case that the active medium is uniformly pumped. The pump absorption efficiency is derived from equation 3.17:

$$\eta_p = 1 - e^{-\sigma_{a,\text{eff}} N_0 l_{cr}} \tag{3.27}$$

The quantum efficiency η_q is the amount of ions excited into the upper laser level per each pump photon absorbed. The intrinsic lifetime of the upper laser level is denoted by τ_1. The cavity photon lifetime is:

$$\tau_c = 2l_{opt}/c\delta, \tag{3.28}$$

with $l_{opt} = l_{res} + l_{cr}(n-1)$ the single-pass optical path length in the laser cavity, l_{res} the total cavity length, and l_{cr} and n the length and refractive index of the active medium. The logarithmic roundtrip loss δ, with the cavity out-coupling coefficients $\delta_{i,\text{out}}$ and the cavity loss coefficients $\delta_{j,\text{loss}}$ is:

$$\delta = \sum_i \delta_{i,\text{out}} + \sum_j \delta_{j,\text{loss}} = -\left(\sum_i \ln(R_i) + \ln(1-L)\right), \tag{3.29}$$

with $R_i = 1 - T_{i,\text{out}}$ the reflectivity and $T_{i,\text{out}}$ the transmission of mirror i. The loss due to out-coupling of laser photons is a desired (useful) loss. The intrinsic cavity roundtrip loss is $L = 1 - e^{\zeta 2 l_{cr}}$ with ζ the scattering coefficient. Other loss sources are for example losses introduced by mirror defects or badly attached mirrors.

In the set of equations 3.24 and 3.25, describing the time-dependent population density and photon number it is assumed that the population density is space-independent, so that there is a uniform population density across the entire

volume V_a within the active medium, and a uniform photon density across the entire mode volume V in the cavity. In a laser the spontaneous emission of a photon that is coupled to the laser mode is responsible for the start of laser emission after threshold has been reached. To include the spontaneous emission into equation 3.25, one must quantify the fraction $f_{sp.}N_1/\tau_1$ of spontaneously emitted photons coupled to the laser mode. When omitting this term, one can still calculate the threshold condition for a laser as will follow, but the equations do not describe the starting of laser emission as a result of the spontaneous emission. In a numerical simulation this can be solved by assuming that there are always photons present in a laser cavity to start laser oscillation once the laser reaches threshold.

Using the substitutions $\Delta N = N_1 - fN_0$ and $f_\sigma = \sigma_{a,\text{eff}}/\sigma_{e,\text{eff}}$, the equations 3.24 and 3.25 can be written as

$$\frac{d\Delta N}{dt} = R_p(1+f_\sigma) - \frac{(\sigma_{e,\text{eff}}+\sigma_{a,\text{eff}})c}{V}\Phi\Delta N - \frac{f_\sigma N_T + \Delta N}{\tau_1} \quad (3.30)$$

$$\frac{d\Phi}{dt} = (\frac{V_a\sigma_{e,\text{eff}}c}{V}\Delta N - \frac{1}{\tau_c})\Phi, \quad (3.31)$$

so that the equations depend only on the population inversion density ΔN and the (constant) dopant concentration N_T.

By putting $d\Delta N/dt = 0$, $d\Phi/dt = 0$ and $\Phi = 0$ in equations 3.30 and 3.31, the steady-state conditions can be derived at threshold. The population inversion and pump rate at the threshold of lasing are, respectively:

$$\Delta N_{\text{thr.}} = \frac{V}{V_a\sigma_{e,\text{eff}}c\tau_c} \quad (3.32)$$

$$R_{p,\text{thr.}} = \frac{f_\sigma N_T + \Delta N_{\text{thr.}}}{(1+f_\sigma)\tau_1}. \quad (3.33)$$

By combining the pump rate (equation 3.26) with equation 3.33, the threshold pump power is obtained:

$$P_{\text{thr}} = \frac{\delta + \sigma_{a,\text{eff}}N_T l_{cr}}{\eta_p\eta_q}\frac{h\nu_p}{\tau_1}\frac{A_{\text{cr}}}{\sigma_{e,\text{eff}}+\sigma_{a,\text{eff}}}. \quad (3.34)$$

Above threshold, with $\Phi > 0$, the steady-state inversion ΔN also follows from equation 3.31, and is identical to equation 3.32. This implies that the population inversion is clamped to its threshold value. The steady-state cavity photon number above threshold, derived from equation 3.30, with aid from equations 3.32 and 3.33, equals

$$\Phi_0 = \frac{A_b\delta(1+B_{\text{al}})}{\sigma_{e,\text{eff}}+\sigma_{a,\text{eff}}}\frac{\tau_c}{\tau_1}\left[\frac{P_p}{P_{thr}} - 1\right], \quad (3.35)$$

where A_b is the cross-sectional area of the laser mode, and $B_{\text{al}} = \frac{\sigma_{a,\text{eff}}N_T l_{cr}}{\delta}$ is the ratio of reabsorption loss over the total cavity losses. Equation 3.35 can be

rewritten by multiplying on both sides by $P_{\rm thr}$ and using the expression for $B_{\rm al}$, to obtain:

$$\Phi_0 = \frac{A_b}{A_{cr}} \frac{\tau_c}{h\nu_p} \eta_p \eta_q (P_p - P_{\rm thr}). \tag{3.36}$$

The population inversion does not increase for $P_p > P_{\rm thr}$, but the cavity photon number increases as the pump power increases beyond the threshold pump power. The laser power P_{out} out-coupled from the cavity is calculated as the product of the energy $h\nu_l$ of a laser photon, the exponential decay time due to the out-coupling of photons by an out-coupling mirror and the photon number of equation 3.36:

$$\begin{aligned} P_{out} &= h\nu \frac{\delta_{\rm out} c}{2 l_{\rm opt}} \Phi_0 & (3.37) \\ &= \frac{A_b}{A_{cr}} \frac{h\nu_l}{h\nu_p} \frac{\delta_{\rm out}}{\delta} \eta_p \eta_q (P_p - P_{\rm thr}) & (3.38) \end{aligned}$$

The ratio $\eta_t = A_b/A_{cr}$ is called the transverse efficiency and gives the fraction of the active medium cross section used by the laser beam cross section [130]. In equation 3.38, it has a maximum value of unity in case the beam overlaps the entire excited region A_{cr}. This overlap of the resonating laser photons in the laser cavity with the excited ions determines how much energy of the excited ions (and therefore pump energy) can be converted into laser photons by stimulated emission: if all the excited ions are accessible to the laser photons, stimulated emission into the laser mode and adding to the laser photons is most efficient. The case where the laser mode is larger than the region of excited ions will be discussed later on.

The slope efficiency of an oscillating laser, η_s, is defined as the ratio of the increase of out-coupled laser power over the increase of in-coupled (launched), or absorbed pump power, above threshold. The slope efficiency versus launched pump power is derived from equation 3.38 and equals:

$$\begin{aligned} \eta_s &= \frac{dP_{out}}{dP_p} = \frac{A_b}{A_{cr}} \frac{h\nu_l}{h\nu_p} \frac{\delta_{\rm out}}{\delta} \eta_p \eta_q & (3.39) \\ &= \eta_t \eta_{St} \eta_{\rm out} \eta_p \eta_q & (3.40) \end{aligned}$$

Similarly, the slope efficiency versus absorbed pump power equals:

$$\begin{aligned} \eta_s &= \frac{dP_{out}}{dP_{abs}} = \frac{1}{\eta_p} \frac{dP_{out}}{dP_p} = \frac{A_b}{A_{cr}} \frac{h\nu_l}{h\nu_p} \frac{\delta_{\rm out}}{\delta} \eta_q & (3.41) \\ &= \eta_t \eta_{St} \eta_{\rm out} \eta_q & (3.42) \end{aligned}$$

The Stokes efficiency, $\eta_{St} = h\nu_l/h\nu_p = \lambda_p/\lambda_l$, is the ratio of the laser photon energy over the pump photon energy, where λ_p, λ_l are the pump and laser wavelength, respectively. The out-coupling efficiency is defined as the ratio of out-coupled laser energy over the total loss of energy by the cavity, calculated by the ratio of the respective loss coefficients $\eta_{\rm out} = \delta_{\rm out}/\delta$.

Gaussian laser and pump beams in an end-pumped configuration

In the more complex case of an end-pumped configuration where an active medium is pumped with a Gaussian pump beam with a radius w_p, and a spatial distribution of the pump energy according to the distribution of:

$$r_p(r,z) = \frac{2\alpha}{\eta_p \pi w_p^2} \exp\left(\frac{-2r^2}{w_p^2}\right) \exp(-\alpha z), \tag{3.43}$$

where α is the pump absorption coefficient, such that $\eta_p = 1 - \exp(-\alpha l_{cr})$ is the pump absorption efficiency for an end-pumped configuration. The radial coordinate is defined by r, and the longitudinal coordinate by z. Similarly, the distribution function for the laser Gaussian beam with radius w_l is defined as:

$$\phi_0(r,z) = \frac{2}{\pi w_l^2 l_{cr}} \exp\left(\frac{-2r^2}{w_l^2}\right) \tag{3.44}$$

Both distribution functions for the pump and laser Gaussian beams are normalised to unity over the volume of the active medium. Without again showing a derivation of the equations for the threshold pump power and the slope efficiency, these equations by Risk are presented here [131]. The equation for the threshold pump power for a three-level laser with Gaussian pump and laser beams is:

$$P_{\text{thr}} = \frac{\delta + 2N_T l_{cr}}{4\eta_p \eta_q} \frac{h\nu_p}{\tau_1} \frac{\pi w_l^2 + \pi w_p^2}{\sigma_{e,\text{eff}} + \sigma_{a,\text{eff}}}, \tag{3.45}$$

and the equation for the slope efficiency of such a laser is:

$$\eta_s = \frac{dP_{out}}{dP_p} = \eta_p \eta_q \eta_{St} \eta_{\text{out}} \frac{dS}{dF}, \tag{3.46}$$

where dS/dF has the same function as the transversal efficiency η_t of equations 3.40 and 3.42, which is to quantify the efficiency with which absorbed pump photons are converted into laser photons. dS/dF is also sometimes called the mode-coupling efficiency, between the pump and laser mode [132]. If $dS/dF = 1$, every pump photon absorbed beyond the amount required to reach threshold, causes the emission of η_q laser photons. Risk showed that for a four-level laser, the ratio of pump beam radius over laser beam radius $a = w_p/w_l$ should be as small as possible. This is because the stimulated emission rate depends partly on the intensity of the stimulating field, which is highest in the centre of the laser beam so that the pump energy is most efficiency converted to laser photons. The wings of the four-level laser beam that do not overlap with a region of pumped ions will not suffer from reabsorption loss. Risk further showed that when reabsorption increases from zero in a four-level laser to a finite value in a (quasi-)three-level laser, the ratio of pump beam radius over laser beam radius $a = w_p/w_l$ that results in the best conversion efficiency between pump and

laser energy, increases toward unity [131]. The reason for this is there being an optimum between two competing factors: (1) as $a = w_p/w_l$ gets closer to zero, a high stimulating laser field over the entire excitation profile ensures optimum extraction of the pump energy, and (2) as $a = w_p/w_l$ increases to infinity, the overlap of the laser beam with lossy, unpumped regions decreases. Further, as the pump power increases, the region overlapping with the wings of the pump and laser beams becomes increasingly pumped, so that the ground state becomes increasingly bleached, and the laser reabsorption loss decreases. Hence, both the overlap of the pump and laser beams, and the pump power in case of reabsorption, influence dS/dF.

The quantity dS/dF, not shown here directly, is derived by differentiating the inverse equation for the calculation of the pump power as a function of the intra-cavity laser power:

$$F = \frac{1 + \dfrac{L_{\text{reab}}}{S}\ln(1+S)}{\displaystyle\int_0^{\infty} \frac{\exp\left[-(a^2+1)x\right]}{1 + S\exp(-a^2 x)}\,dx}. \tag{3.47}$$

A substitution of the radius r by the relation $x = 2r^2/w_p^2$ was made to simplify the calculation. The ratio of reabsorption loss to total cavity loss is indicated by L_{reab}. F is a normalised variable proportional to pump power, and S is a normalised variable proportional to the intra-cavity laser power. These three variables L_{reab}, F, and S are defined as follows:

$$L_{\text{reab}} = \frac{2N_{\text{T}}\sigma_{a,\text{eff}}l_{cr}}{\delta} \tag{3.48}$$

$$F = \frac{4\tau_1\eta_p\eta_q(\sigma_{a,\text{eff}} + \sigma_{e,\text{eff}})}{\pi h\nu_p w_l^2 \delta}P_p \tag{3.49}$$

$$S = \frac{2c\tau_1(\sigma_{a,\text{eff}} + \sigma_{e,\text{eff}})}{n\pi w_l^2 l_c}\Phi \tag{3.50}$$

Here, $\Phi = 2nl_{cr}P_{\text{cav}}/ch\nu_l$ is the total number of laser photons in the cavity with P_{cav} the intra-cavity laser power traveling in one direction. The calculation is straightforward by using the intra-cavity laser power P_{cav} as the input to calculate Φ and S, which can be used together with L_{reab} to calculate F in equation 3.47, which is proportional to the incident pump power P_p according to equation 3.49. This will need to be repeated for a range of powers P_{cav} in order to derive an input-output curve for the laser performance.

3.2.4 Transient laser behaviour

In the rate equation derivation above, steady state operation has been assumed. However, the coupled interaction between the population inversion and laser radiation within the resonator combined with small fluctuations in the pump power,

cavity losses and other factors give rise to oscillations of the laser output power. These oscillations are called relaxation oscillations, and generally take the form of damped sinusoidal fluctuations of both the population inversion and output power. Since the frequency of the relaxation oscillation is strongly related to the characteristics of the ion and the used laser cavity, these relaxation oscillations are a very useful tool to derive properties such as the losses in the laser cavity, provided the other parameters are known [133, 134].

A small temporal perturbation of δN to the steady-state population inversion and $\delta\Phi$ to the steady-state cavity photon number results in small oscillations about the steady-state values. This dynamic behaviour can be described analytically, provided that the perturbations are small compared to the steady state population density and photon number, such that $\delta N \ll \Delta N_0$ and $\delta\Phi \ll \Phi_0$.

By inserting $\Delta N(t) = \Delta N_0 + \delta N(t)$ and $\Phi(t) = \Phi_0 + \delta\Phi(t)$ into equations 3.30 and 3.31, and comparing this with the steady-state ($d\Delta N/dt = d\Phi/dt = 0$) solutions to these equations, the differential equations describing the dynamic behaviour of the photon number can be derived:

$$\frac{d\delta N(t)}{dt} = \frac{-(\sigma_{a,\mathrm{eff}} + \sigma_{e,\mathrm{eff}})c}{V}\left[N_0\delta\Phi(t) + \Phi_0\delta N(t)\right] - \frac{\delta N(t)}{\tau_1} \tag{3.51}$$

$$\frac{d\delta\Phi(t)}{dt} = \frac{V_a\sigma_{e,\mathrm{eff}}c}{V}\Phi_0\delta N(t), \tag{3.52}$$

where the product terms of $\delta N(t)\delta\Phi(t)$ have been omitted because of their negligible contribution. These differential equations combine to a single differential equation, if the latter equation is substituted in the first:

$$\frac{d^2\delta\Phi(t)}{dt^2} + \frac{d\delta\Phi(t)}{dt}\left[\frac{c\Phi_0(\sigma_{a,\mathrm{eff}} + \sigma_{e,\mathrm{eff}})}{V} + \frac{1}{\tau_1}\right] + \delta\Phi(t)\frac{V_a\sigma_{e,\mathrm{eff}}(\sigma_{a,\mathrm{eff}} + \sigma_{e,\mathrm{eff}})c^2N_0\Phi_0}{V^2}. \tag{3.53}$$

The solution to this second-order differential equation is an exponential function of the form $\Phi(t) = \Phi_0 + C_1\exp(-\gamma_{sp}t)\cos(\sqrt{(}\omega^2 - \gamma^2))$ [134], where γ is the oscillation damping coefficient and ω is the oscillation frequency [135]. ω^2 is given by:

$$\omega^2 = \frac{1}{\tau_1\tau_c}(1 + c\sigma_{a,\mathrm{eff}}N_T\tau_c/n)\left[\frac{R_p}{R_{p,\mathrm{thr}}} - 1\right], \tag{3.54}$$

or:

$$\omega^2 = \frac{\tau_c}{\tau_1}\left(1 + N_T\frac{\sigma_{a_{\mathrm{eff}}}}{\tau_c}\frac{c}{n}\right)\left(\frac{P_p}{P_{p,\mathrm{thr}}} - 1\right). \tag{3.55}$$

Equation 3.55 is used later on to calculate the intrinsic loss from a channel waveguide laser.

The relaxation-oscillation frequency is often written as in equation 3.54, using a ratio of the pump rate over the pump threshold rate. However, as explained by Agazzi, this scaling with respect to the threshold pump rate can cause significant underestimation of the relaxation-oscillation frequency in case the threshold

pump rate is affected by quenching effects as a result of energy transfer between clustered ions, or to co-doped impurities [135]. A proposed better way to use these equations is to subtract the threshold pump rate from the pump rate above threshold:

$$\omega^2 = \frac{c(\sigma_{a,\mathrm{eff}} + \sigma_{e,\mathrm{eff}})}{n}(R_p - R_{p,\mathrm{thr}}), \tag{3.56}$$

The pump rate $R_{p,\mathrm{thr}}$ used in equations 3.54 and 3.56 is given by:

$$R_{p,\mathrm{thr}} = \frac{n}{c\tau_1\tau_c}\frac{1}{\sigma_{a,\mathrm{eff}} + \sigma_{e,\mathrm{eff}}}(1 + c\sigma_{a,\mathrm{eff}}N_T\tau_c/c). \tag{3.57}$$

CHAPTER 4

Highly efficient lasers

In chapter 2, the design and fabrication steps of ridge-type channel waveguides in potassium double tungstate layers have been explained. The process steps explained in that chapter have been used to create several thulium-doped channel waveguides which have been the subject of study for their lasing performance. The current chapter discusses the various experiments performed and results obtained on these micro channels fabricated in potassium double tungstate crystals.

4.1 Efficient lasers in low-loss buried channel waveguides

4.1.1 Fabrication of thulium-co-doped microchannel waveguides

Using the fabrication steps explained in chapter 2, a co-doped layer of $KY_{0.4}Gd_{0.295}Lu_{0.29}Tm_{0.015}(WO_4)_2$ with a thickness of several tens of micrometers was grown onto a pure, (010)-orientated, laser-grade polished KYW substrate by liquid-phase epitaxy in a $K_2W_2O_7$ solvent at $920 - 923$ °C. The relatively low thulium concentration of 1.5 at.% was selected as a starting point to investigate the concentration dependence of the laser performance of thulium-co-doped potassium double tungstate crystals. This concentration corresponds to a value of 0.95×10^{20} cm^{-3}, via the method discussed in chapter 2. The layer was lapped and polished to a thickness of 6.6 µm with laser-grade surface uniformity. A photoresist mask (Fujifilm OiR 908/35) was deposited onto the layer and patterned. Ar^+-beam milling at an acceleration voltage of 350 eV, resulting in an etch rate of 3 nm/minute, was applied to the sample to produce ridge-type channel waveguides along the N_g optical axis with widths of $7.5 - 12.5$ µm and an etch depth of 1.5 µm. Afterwards the channel waveguides were overgrown with a pure KYW cladding layer to prevent, firstly, additional scattering losses at the channel-air interface and, secondly, detrimental rounding effects at the end facets during end-face polishing. After overgrowth, the samples were diced and end-face polished to a length of 8.4 mm.

4.1.2 Laser experiments on thulium-co-doped microchannel waveguides

Laser experiments on the Tm^{3+}-doped channel waveguides were carried out using a titanium-sapphire pump laser tuned alternatively to a wavelength of 794 nm in transverse-magnetic (TM, E $\|N_p$) polarisation, or 802 nm in transverse-electric (TE, E $\|N_m$) polarisation. The pump absorption cross-section in these thulium-doped channels of exceeding 8×10^{-20} cm^2 at 794 nm is the highest, compared to almost 6×10^{-20} cm^2 at 802 nm.

The experimental setup for the laser characterisation of the channel waveguides is shown in figure 4.1a. In-coupling of pump light into the channels was optimized using cylindrical lenses with focal lengths of 40 mm and 10 mm to focus the pump beam in the horizontal and vertical directions, respectively. In this way, the mode mismatch between pump beam and the elliptical channel pump mode (figure 2.8) is minimised by shaping the circular, Gaussian pump beam into an elliptical pump beam. An overlap efficiency of approximately 95% was achieved in this way between the incident pump beam and channel pump mode, determined via imaging of the pump beam and its calculated overlap with the channel fundamental pump mode using Phoenix FieldDesigner software.

Dielectric mirrors with a reflectivity of $R = 99.9$ % (highly reflective, HR), $R = 98\%$, and $R = 92\%$ at $1900-2100$ nm and high transmission of $T = 99.5\%$ at $790-810$ nm were butt-coupled to the sample using index-matching, fluorinated oil (Fluorinert). Mirror combinations of HR and $R = 98\%$, HR and $R = 92\%$, and twice $R = 92\%$ reflectivity were used to assess the laser performance. The laser output power was out-coupled from the end-facet opposite to the in-coupling end-facet via a microscope objective with a numerical aperture of NA = 0.25. A high-pass filter (Schott RG-1000) with a cut-off wavelength of 1000 nm was placed behind the out-coupling objective to block any residual, unabsorbed pump power. For the configuration with two 92% out-coupling mirrors, the laser output power was also measured at the pump in-coupling side by use of a beam splitter and a high-pass filter. Since the in- and out-coupling optics and the high-pass filter introduce losses in the setup, the measured pump and laser output power do not represent the actual power in- and out-coupled from the waveguide. The transmission coefficients of the used optics have been used to obtain the correct values.

A spectrometer (Horiba Jobin Yvon *i*HR550) was used to determine the laser wavelength. The polarisation of the 2-µm laser was determined by passing the beam through a polariser with an extinction ratio of 1000:1 at wavelengths of $650-2000$ nm and its beam quality was analysed with a beam profiler (Coherent Lasercam-HR). Cavity losses at the laser wavelength were determined by measuring the relaxation-oscillation frequency as a function of pump power via an InGaAs detector (Thorlabs FGA20) connected to an oscilloscope (HP-Agilent In-

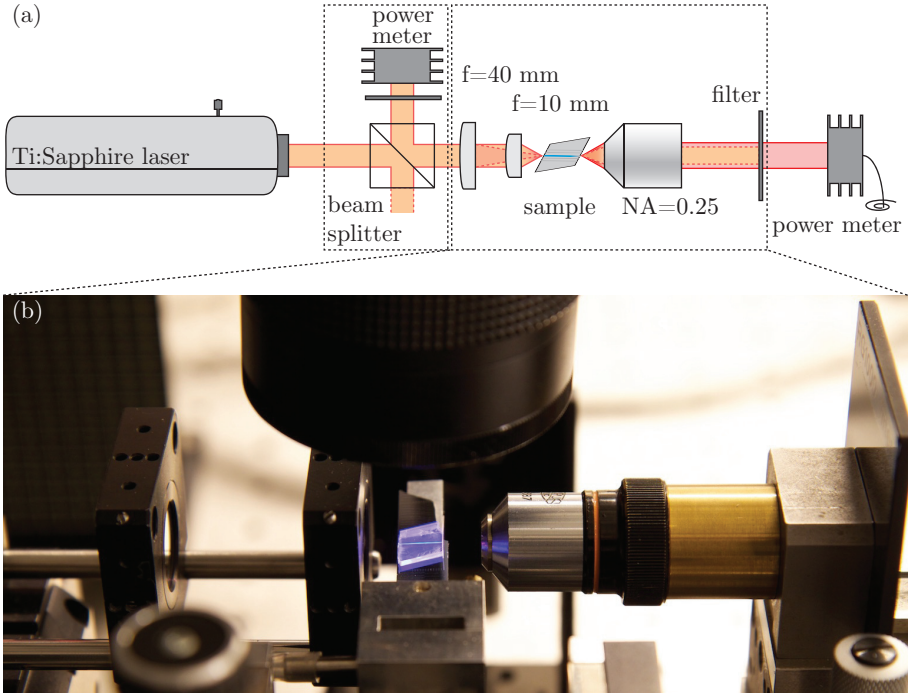

Figure 4.1 Experimental setup for the assessment of laser performance. (a) Laser light from a tuneable titanium-sapphire pump laser, emitting at a wavelength of around 800 nm, is focussed into a channel waveguide by two cylindrical lenses with focal lengths of 40 mm (horizontal) and 10 mm (vertical). Dielectric mirrors are (optionally) attached to the end-facets using index-matching oil. A microscope lens with a numerical aperture of 0.25 is used for out-coupling of laser light from the channel waveguide. An RG1000 high-pass filter (cut-off wavelength of 1000 nm) is used to prevent any residual pump light of reaching the power meter. In some experiments, an additional beam-splitter cube, filter and power meter were used to measure the amount of laser light emitted from the pump in-coupling end-facet. (b) Photograph of the actual setup with a micro-structured thulium-doped crystal pumped by a titanium-sapphire laser. The cylindrical in-coupling lenses are visible on the left, and the RG1000 high-pass filter on the right. The blue fluorescent light is typical of thulium-doped media, and originates from $^1D_2$ and $^1G_4$ upper manifold de-excitations. Though hardly visible, in this experiment this particular crystal has had dielectric mirrors attached to both end-facets using index-matching oil.

finium). The locking signal to the oscilloscope was provided by a chopper wheel running at 133 Hz, placed in the pump beam (not shown in figure 4.1).

4.1.3 Experimental results

Output power, efficiency and thresholds

The output power of the laser measured with a variety of dielectric mirror combinations of increasing out-coupling transmission $T_{\text{out}} = 1 - R_1 R_2$, and for different pump in-coupling frequency and polarisation are plotted in figure 4.2. Figures 4.2a,b show the data measured at a pump wavelength of 802 nm, in TE polarisation, while figures 4.2c,d show the data measured at a pump wavelength of 794 nm in TM polarisation. The measured data are indicated by the dots, while a linear fit through the data indicates the slope efficiency, which are visualised by solid lines. Due to the low pump absorption of $< 50\%$ in these micro channels with this thulium dopant concentration of 1.5at.%, the laser output power has been plotted versus launched pump power and absorbed pump power. The maximum measured output power for this laser amounted to 149 mW, and was obtained while pumping at 794 nm in TM polarisation and with mirrors of $R = 92\%$ reflectivity butt-coupled to both end-facets, yielding a combined out-coupling transmission of $T_{\text{out}} = 1 - 0.92^2 \approx 15\%$. The measured output power and pump power relates to a maximum slope efficiency of 11.1% (versus launched pump power), or 31.5% (versus absorbed pump power). The laser performance when pumping at 802 nm in TE polarisation and the same out-coupling transmission was significantly lower with 76 mW of output power and 17% of slope efficiency versus absorbed pump power. Bolaños, however, demonstrated his best laser performance in TE polarisation on a buried micro channel, mirror-less laser with a thulium concentration twice as high as discussed here [53]. The different results between the two polarisations, and the opposite conclusion between the results demonstrated here and obtained by Bolaños could indicate that in-coupling of pump light was not optimized in case of the measured inferior laser results of this work and the work of Bolaños. The threshold of the laser of figure 4.2 was as low as 7 mW when out-coupling with $T_{\text{out}} = 2\%$ and pumped in 794 nm in TM polarisation. As expected, the threshold increases for higher out-coupling efficiencies with a maximum threshold of 15 mW for an out-coupling transmission of $T_{\text{out}} = 15\%$. The measured threshold values are significantly lower than previously reported results in planar and mirror-less lasers [53, 69]. This is a result of the better horizontal confinement in the channel compared to a planar waveguide and a lower output coupling transmission compared to the mirror-less laser and better vertical confinement compared to both previous results.

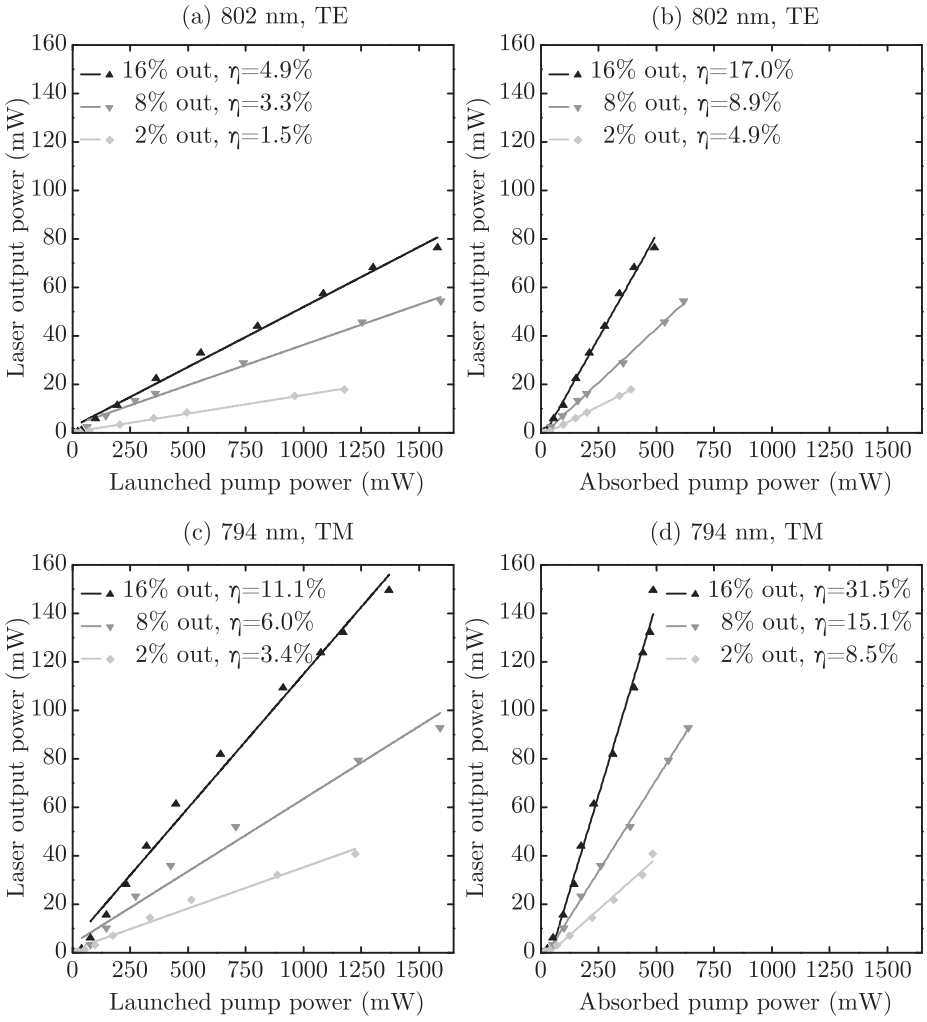

Figure 4.2 Laser output power versus launched and absorbed pump power for a 1.5at.%-doped thulium laser. The laser was pumped at 802 nm in TE polarisation (a,b), and 794 nm in TM polarisation (c,d). The output power was plotted as a function of launched pump power (a,c) and absorbed pump power (b,d). Approximately one-third of the launched pump power was absorbed in the waveguides with a length of 8.4 mm, which results in a much larger slope efficiency versus absorbed pump power (max. 31.5%) compared to launched power (max. 11%). By increasing the dopant concentration, the pumping efficiency and cross-relaxation efficiency can likely dramatically be increased.

Table 4.1 Laser parameters used for the calculation of the waveguide propagation losses.

Parameter	Value	Reference
Reflectivity of mirrors, R_1, R_2	0.99, 0.92	Manufacturer
Optical resonator length, $2l_{opt}$	33.9 mm	Calculated
$^3F_4$ upper laser level lifetime, τ_1	1.4 ms	Measured
Tm^{3+} dopant concentration, N_T	0.935×10^{20} cm^{-3}	Calculated
Eff. refractive index of laser mode, n	2.006	Calculated
Eff. absorption cross-section (1934 nm), σ_a	6.68×10^{-22} cm^2	[39]

Multi-wavelength operation by selection of the output coupler

As a result of the increased out-coupling transmission and related increased cavity losses, the laser operating wavelength was found to shift significantly as displayed in figure 4.3. The laser was found to operate at wavelengths around 1930 nm, when a low out-coupling transmission of $T_{\text{out}} = 2\%$ was used. With different mirror configurations and their related out-coupling transmission of $T_{\text{out}} = 8\%$ and $T_{\text{out}} = 15\%$, a shift to shorter wavelengths of 1906 nm and 1846 nm, respectively, was measured. The higher losses due to the higher out-coupling transmission increase the threshold inversion and cause the laser to shift toward shorter wavelengths where the maximum gain is higher [39, 51]. The shape and line width of the laser emission peaks indicate that the laser operates on multiple longitudinal modes.

Determining the losses of the waveguide

The propagation losses of the waveguide were determined by measuring the relaxation-oscillation frequency as a function of the pump power over the pump threshold. The relaxation-oscillations, measured for the 1.5 at.% thulium-doped laser with 80 mW of launched pump power which is approximately ten times above threshold, are displayed in figure 4.4a. The pump energy supplied to the channel waveguide is modulated on/off by a chopper wheel rotating at 133 Hz. The strong spiking behaviour is the result of the population inversion and photon number relaxation about their threshold value, switching the laser on and off. Continuous-wave operation of the laser is reached after approximately 40 µs. The relation-oscillation frequency as a function of the pump power is shown in figure 4.4b, measured to approximately five times above threshold for a laser with out-coupling mirrors of HR and 92%. The threshold was approximately 7 mW of absorbed pump power. A linear fit through the measured data, combined with

parameters of the laser indicated in table 4.1 and equation 3.54, yields a value for the waveguide propagation loss of 0.1 ± 0.03 dB/cm (or approximately 4% of round-trip losses). Compared to other lasers realised in double tungstate channel waveguides, for example a Gd^{3+}-Lu^{3+}-Yb^{3+}-co-doped KYW channel waveguide laser with a waveguide propagation loss of 0.34 dB/cm [49], this value is lower. Our result can be partially explained by the longer operating wavelength ($\sim$2 µm in Tm^{3+}, compared to $\sim$1 µm in Yb^{3+}) which results in lower scattering losses. Potential losses introduced by imperfect butt-coupling of the dielectric mirrors also contribute to the measured losses, and are likely less wavelength-dependent than scattering losses.

Verification of the single-mode behaviour of the channel waveguide

In order to get a sense of the transverse-mode behaviour of the waveguide, the near-field output profile has been measured with a beam-profiler camera, and displayed in figure 4.5. The waveguide has been designed to support only the fundamental transverse mode profiles for both pump and laser wavelength, to maximise the pump/laser intensity overlap and therefore the overall efficiency of the laser. In a channel waveguide, it is generally difficult to find a balance between forced fundamental-mode behaviour and overlap between the modal intensities and the active medium, especially when the difference between pump wavelength and laser wavelength is large. It is usually the shorter wavelengths that run into higher-transverse-mode behaviour even when longer wavelengths still have a fundamental-transverse-mode character. Therefore, if the single-transverse-mode character of the pump mode can be proven, this almost certainly means that the laser mode is also of fundamental-transverse-mode nature. The measured mode profile of the pump mode exiting the channel waveguide, measured by a beam profiler camera, is displayed in figure 4.5. The $1/e^2$ intensity radii of the slightly elliptical mode profile were 6.1×3.5 µm^2. The expected quasi-TE laser polarisation was measured by using a polariser and revealed a 12:1 power ratio in favour of TE polarisation.

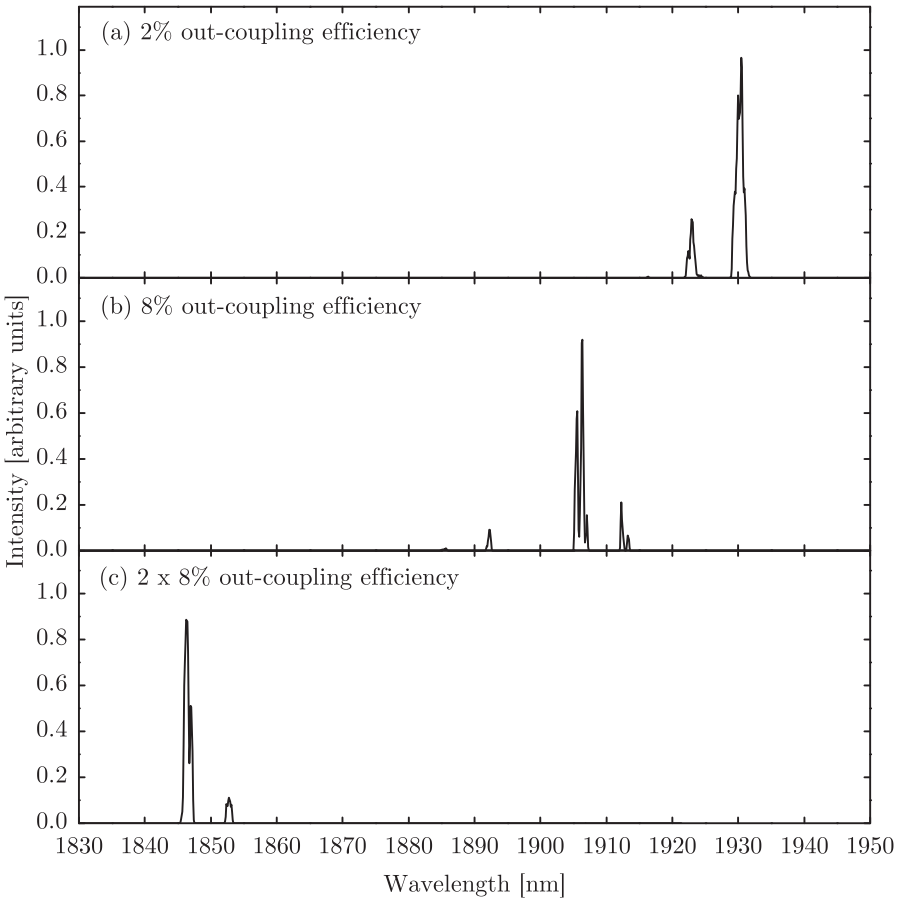

Figure 4.3 Laser operating wavelength as a function of out-coupling transmission. The operating frequency of the 1.5 at.% thulium-doped waveguides was dependent on the out-coupling transmission. The laser operating wavelength and out-coupling transmission combinations are (a) 1930 nm for 2% of out-coupling, (b) 1906 nm for 8% of out-coupling, and (c) 1846 nm for $2 \times 8\%$ of out-coupling.

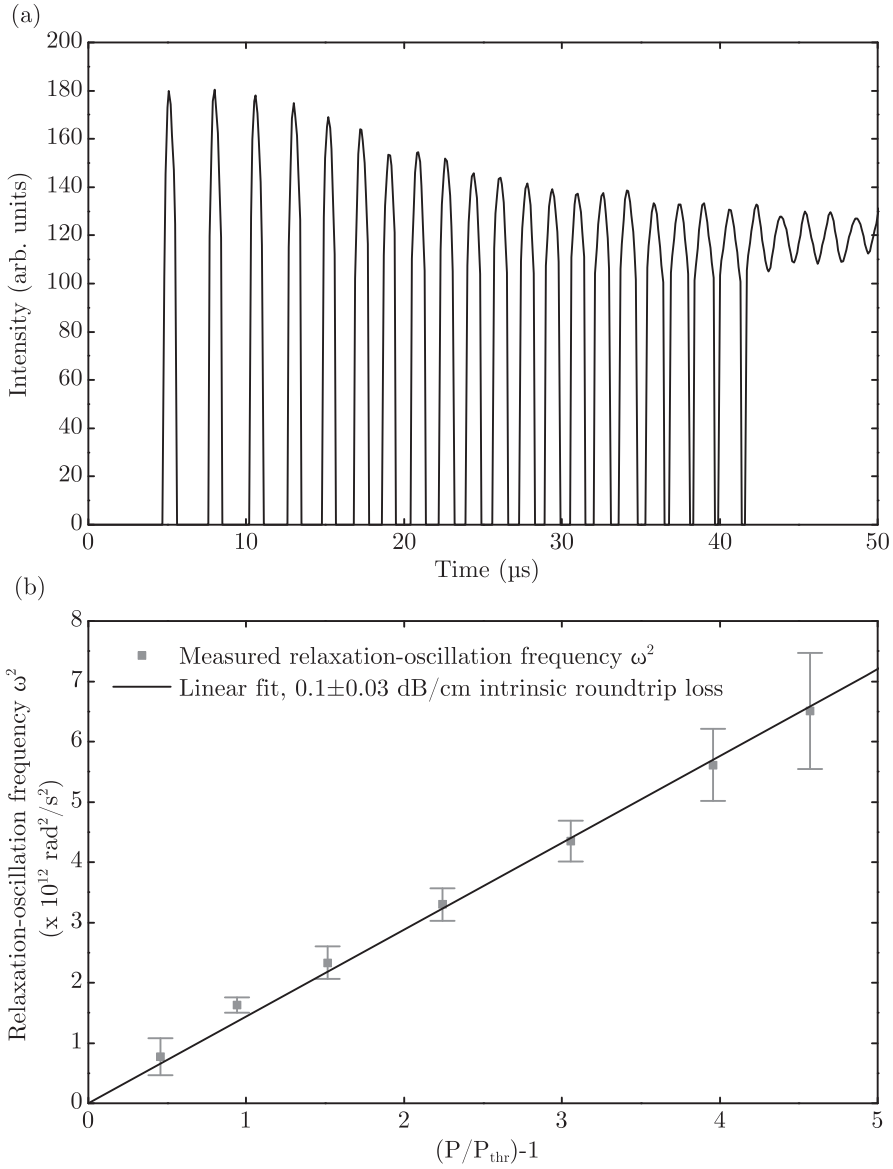

Figure 4.4 Relaxation-oscillation frequency measured in a the 1.5at.%-doped thulium laser. (a) Strong spiking behaviour of the laser output during starting-up, when the laser is pumped approximately 10 times above threshold at 80 mW of launched pump power. (b) Plot of the measured relaxation-oscillation frequency ω^2, as a function of P/P_{the}, according to equation 3.54. From a linear fit through the measured data, with the waveguide propagation loss as a free parameter, a value of 0.1 ± 0.03 dB/cm for the propagation loss was calculated. The error bars represent the standard deviation of the recorded frequency by the oscilloscope.

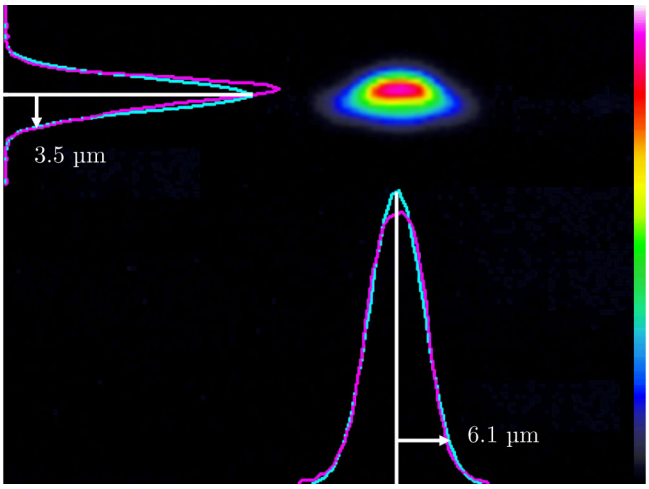

Figure 4.5 Mode profile of the pump mode exiting from the channel waveguide. The profile was measured with a beam profiler camera and the $1/e^2$ Gaussian fit results in intensity radii of 6.1×3.5 µm^2.

4.2 Laser efficiencies - toward the theoretical limit

In the previous paragraph, the results of a 1.5at.%-doped thulium laser were presented. This laser exhibited a very low propagation loss, a reasonably high slope efficiency versus absorbed pump power, and low thresholds. However, the pump absorption coefficient was rather low, resulting in a poor use of the available pump power and therefore a rather low slope efficiency versus launched pump power.

There are different methods to improve the slope efficiency of the laser, which include the use of a longer channel waveguide, multi-pass pumping schemes, and employing higher dopant concentrations. Since the channel waveguide length of the laser presented in the previous paragraph is 8.45 mm, and the maximum size of the crystals grown in our facility is 1×1 cm^2, the option of using longer channel waveguides is ruled out. The use of a multi-pass pumping scheme would require a different set of dielectric mirrors and the expected improvement of the slope efficiency is presumably limited (less than double the absorption compared to the previous paragraph) as a result of the intrinsically low pump absorption in channel waveguides with this low dopant concentration and length.

A straightforward way to improve the optical-to-optical efficiency and internal slope efficiency of the laser is therefore to increase of the dopant concentration. As discussed in chapter 3, this will expectedly also increase the efficiency of the cross-relaxation effect, which is a very beneficial process in thulium lasers pumped at the wavelengths around 800 nm.

4.2.1 Fabrication

Following the fabrication steps of chapter 2, co-doped layers of $KY_{0.4}Gd_{0.29}Lu_{0.28}Tm_{0.03}(WO_4)_2$, $KY_{0.4}Gd_{0.29}Lu_{0.26}Tm_{0.05}(WO_4)_2$, $KY_{0.4}Gd_{0.29}Lu_{0.23}Tm_{0.08}(WO_4)_2$, $KGd_{0.48}Lu_{0.40}Tm_{0.12}(WO_4)_2$, and $KGd_{0.47}Lu_{0.33}Tm_{0.20}(WO_4)_2$ were grown onto pure $KY(WO_4)_2$ substrates by liquid-phase epitaxy. The Tm^{3+} dopant concentration of the 3at.%, 5at.%, 8at.%, 12at.% and 20at.%-doped samples are 1.91×10^{20} cm^{-3}, 3.18×10^{20} cm^{-3}, 5.09×10^{20} cm^{-3}, 7.63×10^{20} cm^{-3} and 12.7×10^{20} cm^{-3}, respectively, calculated via the method out-lined in chapter 2. These layers were lapped and polished to a thickness of, respectively, 6.6 µm, 7.7 µm, 14.3 µm, 8.8 µm, and 8.8 µm, and were of laser-grade quality. Micro-fabrication of channel waveguides was performed, realising ridge-type channels with a width of $10 - 25$ µm on the samples, and etched, respectively, to a depth of 1.5 µm for the 3at.% and 5at.% doped samples, 1.9 µm for the 8at.% doped sample, and 1.8 µm for the 12at.% and 20at.%-doped sample by Ar^+-beam milling. As with the 1.5at.%-doped sample of paragraph 4.1, the channel waveguides were also oriented along the N_g optical axis. These samples were subsequently overgrown with a pure $KY(WO_4)_2$ cladding layer firstly to

Table 4.2 Fluorescence lifetimes of the $^3F_4$ multiplet found in the literature. Lifetimes (τ_1) and measurement methods for the three relevant compositions have been summarized.

Composition	Tm^{3+} (at.%)	τ_1 (ms)	Method	Ref.
$KY(WO_4)_2$:Tm^{3+}	15	1.47	meas., backscattered lum. decay	[56]
$KY(WO_4)_2$:Tm^{3+}	0.1	1.11	meas., lum. decay of tungstate powder concentration range in suspension	[39]
$KGd(WO_4)_2$:Tm^{3+}	0.1−10	1.53 − 1.76	meas., lum. decay on bulk samples	[136]
$KGd(WO_4)_2$:Tm^{3+}	5	0.90	meas., lum. decay using pinhole	[40]
$KLu(WO_4)_2$:Tm^{3+}	3	1.34	meas., lum. decay using pinhole	[40]
$KLu(WO_4)_2$:Tm^{3+}	5	0.90	meas., lum. decay using pinhole	[40]

symmetrise the channel refractive index contrast in vertical direction, secondly to protect the channel waveguides and to ease further sample processing, and thirdly to allow better butt-coupling of the dielectric mirrors. After overgrowth, the samples were diced to lengths of 7.3, 6.7, 4.2, 2.8 and 2.8 mm, respectively, and end-face lapped and polished. Experiments to determine the fluorescence lifetime and laser performance were then performed on these samples.

4.2.2 Fluorescence lifetimes of thulium-co-doped layers

Fluorescence lifetimes of the $^3F_4$ upper laser level

Excited-state lifetimes for the $^3F_4$ multiplet can be found in the literature for thulium-doped $KY(WO_4)_2$, $KLu(WO_4)_2$ and $KGd(WO_4)_2$, and these are shown in table 4.2. Lifetimes for the $^3F_4$ multiplet between $0.90 - 1.76$ ms are reported for the different thulium-doped compositions, with $KGd(WO_4)_2$ having the longest lifetimes and $KLu(WO_4)_2$ the shortest. Since, in this work, we are using thulium-yttrium-gadolinium-lutetium-co-doped double tungstates with a range of fractions for the different rare-earth ions, the lifetimes will also vary as a function of the dopant fractions. Therefore, the $^3F_4$ fluorescence lifetimes τ_1 of the 1.5at.%, 3at.%, 5at.% and 8at.% thulium-doped compositions mentioned in the previous paragraph were determined via luminescence decay measurements.

The setup for the luminescence decay measurements is shown in figure 4.6. A Ti:Sapphire laser tuned to 794 nm in transverse-magnetic polarisation (TM, $E \| N_p$) is used as a pump source to excite the thulium-doped samples. In-coupling of pump light is done via two cylindrical lenses with focal lengths of 40 mm

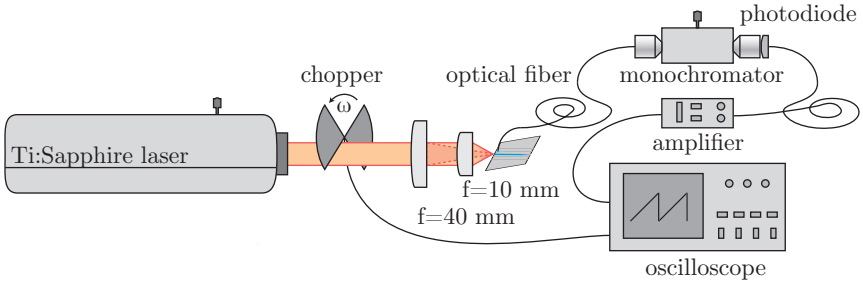

Figure 4.6 Experimental setup for measuring excited-state luminescence decay times. Laser light from a tuneable titanium-sapphire pump laser, emitting at a wavelength of around 800 nm, is focussed into a channel waveguide by two cylindrical lenses with focal lengths of 40 mm (horizontal) and 10 mm (vertical). The pump light is chopped at a frequency ω. Fluorescent light emitted by the excited thulium ions in the channel waveguide is collected via a top-mounted fibre and focussed into a monochromator to select the wavelength corresponding to the energy of the radiative transition of interest. The filtered light is focussed onto a photodiode which generates an electrical signal which is then amplified and recorded by an oscilloscope. The oscilloscope is triggered by the chopper signal.

(horizontal) and 10 mm (vertical). The cw pump light was modulated (quasi-cw) via a chopper wheel with 50% duty cycle, which chopper signal was also used as a trigger for the oscilloscope. Luminescence originating from the $^3F_4$ manifold upon radiative de-excitation to the $^3H_6$ ground manifold was collected via a standard 9-µm fibre into a monochromator tuned to the wavelength of 1840 nm where the highest intensity was obtained and focussed onto an InGaAs detector connected to the oscilloscope. The fibre was placed at the beginning of the sample to collect luminescence from regions where the excitation was highest, in order to reduce the effects of lifetime elongation as a result of radiation trapping. The fibre acts as a natural pinhole to reduce in-coupling of luminescence originating from weakly-pumped regions beside the waveguide.

The data of the luminescence decay measurements, averaged over several thousands of traces to reduce noise, were analysed and plotted on a (natural) logarithmic scale as a function of time in figure 4.7. The lifetime τ_1 is equal to the inverse, negative slope of the linear fit through the data. From the slopes, lifetimes of $\tau_1 = 1.40, 1.30, 1.21, 1.15$ ms for the 1.5at.%, 3at.%, 5at.% and 8at.% thulium-doped samples, respectively, have been determined. These values for the fluorescence lifetime of the $^3F_4$ manifold agree well with the data presented in table 4.2; it is expected that for the compositions used in this work, the fluorescence lifetime is approximately a linear combination of the fluorescence lifetimes

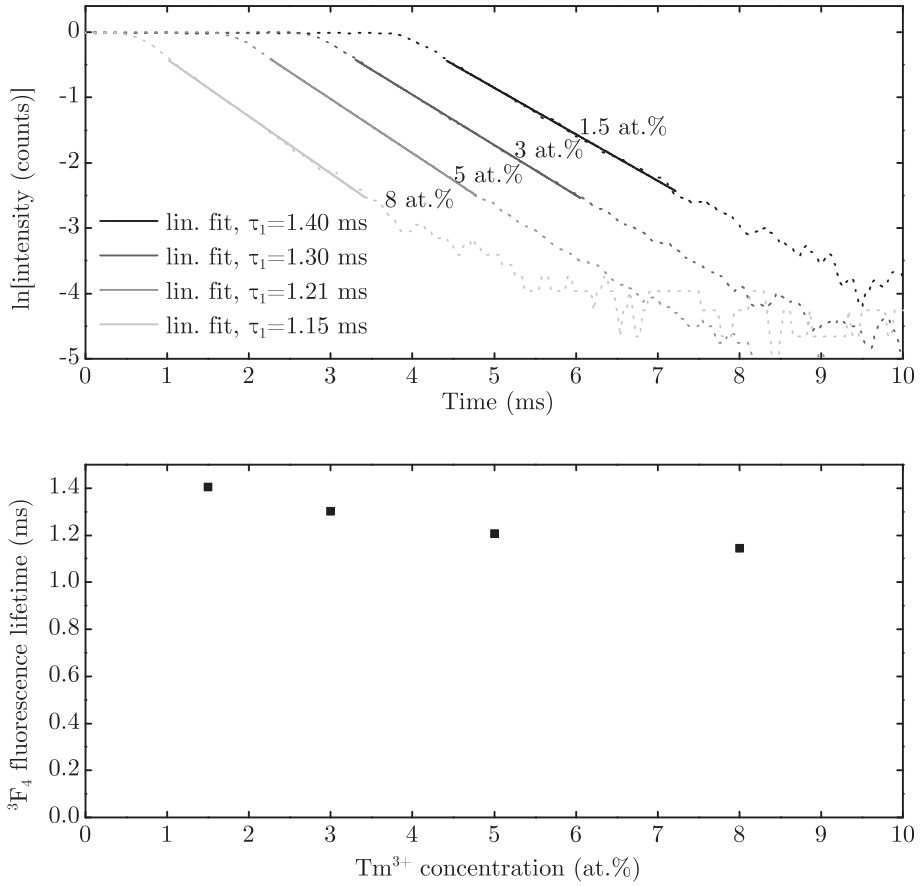

Figure 4.7 Luminescence lifetimes of the $^3F_4$ level in thulium-co-doped channel waveguides. The lifetimes τ_1, obtained via luminescence decay measurements are 1.40, 1.30, 1.21 and 1.15 ms, for 1.5at%, 3at.%, 5at.% and 8at.% thulium-doped samples, respectively (bottom figure). These lifetimes have been obtained from a linear fit through the logarithmic intensity-over-time data (top figure).

of the fractions of (nearly) stoichiometric compounds.

Fluorescence lifetimes of the $^3H_4$ upper pump level and the cross-relaxation rate

Data on the luminescence lifetimes of the thulium $^3H_4$ level which is used as the upper pump level in our laser, can be found in the literature for thulium-doped $KGd(WO_4)_2$ [136] and $KLu(WO_4)_2$[137], but not for $KY(WO_4)_2$. The data from this literature is plotted in figure 4.8c, as a function of thulium concentration. The

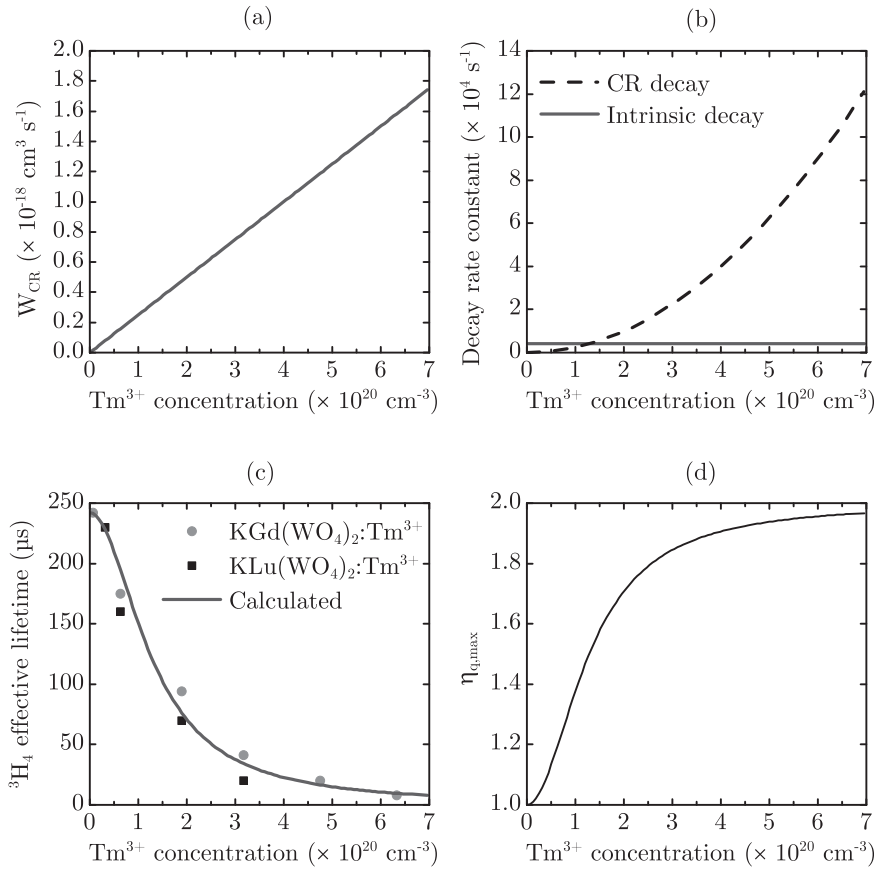

Figure 4.8 Luminescence lifetimes of the $^3H_4$ manifold in thulium-doped $KGd(WO_4)_2$ and $KLu(WO_4)_2$, decay rate and pump quantum efficiency a) cross-relaxation parameter, b) intrinsic and cross-relaxation decay rate constants, c) luminescence lifetimes of the $^3H_4$ manifold in thulium-doped $KGd(WO_4)_2$ and $KLu(WO_4)_2$, and calculated effective lifetime, d) pump quantum efficiency. All data as function of thulium concentration.

observed concentration quenching is attributed to the cross-relaxation process shown in figure 3.7 of chapter 3 [138]: in the absence of inter-ionic processes the lifetime is close to 250 µs, whereas the lifetime decreases to under 10 µs for thulium concentrations exceeding 3×10^{20} cm^{-3}.

The population density in the $^3H_4$ manifold decreases via intrinsic decay and via cross-relaxation. This decay is approximately exponential. If short-pulse excitation from the ground manifold into level $^3H_4$ is assumed, with a low enough

intensity not to bleach the ground manifold, the $^3H_4$ population density decay rate R_3 per unit volume and time (cm^{-3} s^{-1}) is given by:

$$R_3 = -\left(\frac{1}{\tau_3} + W_{CR}N_0\right)N_3 = -\frac{1}{\tau_{3,eff}}N_3. \tag{4.1}$$

In the absence of cross-relaxation, the $^3H_4$ population density decay rate R_3 is equal to the intrinsic decay rate constant $1/\tau_3$ multiplied by the population density of N_3. The intrinsic, concentration-independent, decay rate constant is indicated by the gray line in figure 4.8b.

The macroscopic cross-relaxation rate constant, W_{CR}, is derived from the microscopic parameters C_{DD} (donor-donor) and C_{DA} (donor-acceptor) energy migration and cross-relaxation, respectively [26]:

$$W_{CR} = \frac{\pi^2}{3}\sqrt{C_{DA}C_{DD}}N_d = C_{CR}N_d, \tag{4.2}$$

and is linearly dependent on the thulium doping concentration N_d. While the values of the parameters C_{DD} and C_{DA} remain unknown, a plot of the cross-relaxation parameter is shown in figure 4.8a after derivation of the value of $C_{CR} = 2.5 \times 10^{-37}$ from the lifetime data and the thulium concentration, as explained below.

The cross-relaxation rate constant multiplied by the ground-state population N_0 , defines the $^3H_4$ population density decay rate constant due to cross-relaxation. This decay rate constant, plotted in figure 4.8b by the dashed line, is quadratically dependent on the thulium dopant concentration since it is assumed that the ground state population N_0 is not bleached as a result of short pulse excitation, such that the ground state population density $N_0 = N_T$.

By assuming a value for the concentration-independent parameter $C_{CR} = 2.5 \times 10^{-37}$ cm^6 s^{-1} and by assuming an intrinsic lifetime of $\tau_3 = 242$ µs, the effective lifetime $\tau_{3,eff}$ can be calculated from equation 4.1. The result yields a good fit of the $^3H_4$ literature data, as is visible in figure 4.8c by the solid, gray line.

The pump quantum efficiency η_q, defined as the number of excitations of the $^3F_4$ upper laser level resulting from one pump excitation of the $^3H_4$ level is given by

$$\eta_q = 1 + \frac{W_{CR}N_0}{1/\tau_3 + W_{CR}N_0}. \tag{4.3}$$

For the given parameter values, and in the absence of ground-state bleaching, figure 4.8d shows the relation of the pump quantum efficiency on the thulium concentration. With increasing ground-state bleaching, η_q decreases from this value.

4.2.3 Laser performance

The performance of the channel waveguides was investigated similar to the procedure explained in sub-section 4.1.2, by pumping the channels with a continuous-wave Ti:sapphire laser at a wavelength of 794 nm with TM polarisation, or 802 nm with TE polarisation. Sets of dielectric mirrors with an out-coupling transmission of $T_{\text{out}} = 2\%$, 8%, 16% and 89% were used, and an out-coupling transmission of $T_{out} = 1 - R_1R_2 = 1 - 0.11^2 \approx 99$ % was achieved when using no dielectric mirrors at all. The crystal-air interface of an end-facet provides a Fresnel reflectivity of $R = 1 - 4n_1n_2/(n_1 + n_2)^2 \approx 11\%$, where n_1, n_2 are the wavelength- and polarisation-dependent effective refractive index of the laser mode propagating in the channel, and the refractive index of air, respectively. As a result of this Fresnel reflection, the pump in-coupling efficiency was also reduced by the same amount in case no dielectric mirror was attached to the pump in-coupling end-facet, since these dielectric mirrors are provided with an anti-reflection coating at the pump wavelength. The Fresnel reflectivity of $\approx 11\%$ at one or both bare waveguide end-facets provided sufficient feedback for laser oscillation of the thulium-doped lasers with a thulium concentration higher than 1.5at.%, contrary to the 1.5at.% thulium doped laser which could not be operated at this high out-coupling transmission because of too low gain to reach the threshold.

The calculation of the pump power launched into the channels equals $P_p = \eta_L P_I$, where P_I and P_p are the incident and launched pump power, and η_L is the in-coupling efficiency of the external pump beam into the channel pump mode. The non-coupled fraction $1 - \eta_L$ partly propagates through the undoped part of the sample and is detected as non-absorbed pump power, and is partly lost due to scattering, reflection, and absorption in the planar waveguide region adjacent to the channel waveguide. During the experiments on the 8at.%-doped thulium laser, it was measured that approximately 10% of the incident pump power is detected as non-absorbed pump power, despite the fact that the sample length is long compared to the absorption length of the pump in the absence of ground-state bleaching, and despite the fact that we calculated a coupling efficiency of $\eta_L = 95\%$ for this laser. This indicates that a maximum of 90% of the incident pump power is actually coupled to the pump mode in the channel and absorbed. Since the absorbed pump power is calculated by subtracting the measured residual pump power from the incident pump power, we do not risk the laser slope efficiency to be overestimated, because only a part of the non-coupled pump power fraction $1 - \eta_L$ is detected by the power meter.

Laser performance of 5, 8, 12 and 20at.% thulium-doped waveguides for comparable pump powers

The results of the 5at.%, 8at.%, 12at.% and 20at.%-doped channel waveguide lasers are presented in figures 4.9 through 4.12. All data have been plotted both

as a function of launched and absorbed pump power, and for the two pump wavelengths and polarisations. Contrary to the previous results for the 1.5at.%-doped thulium laser, which, owing to unknown reasons exhibited significantly less efficient operation when pumped at 802 nm in TE polarisation, the results for the other thulium-doped samples show good agreement within a few percent of efficiency, for both pumping wavelengths and polarisations.

For the 5at.%-doped lasers, the highest slope efficiency obtained was 53% versus absorbed pump power in case the laser was pumped at 794 nm in TM polarisation and with 89% of out-coupling efficiency. A lower, but similar result of a slope efficiency of 50% was obtained when pumping at 802 nm in TE polarisation and the same out-coupling configuration. When out-coupling $T_{out} =$ 15%, 8% and 2%, the laser slope efficiency versus absorbed pump power dropped to approximately 31%, 20% and 10%, respectively. The measured thresholds for the different out-coupling combinations varied slightly because of variations in the butt-coupling of the dielectric mirrors, resulting in varying amounts of loss. However, the thresholds amounted to approximately 20 mW of absorbed power for the lowest value for the out-coupling transmission, and increased to a value of approximately 40 mW of absorbed power for the highest ($T_{\text{out}} = 89\%$ and 99%) values of out-coupling transmission.

For the 8at.%-doped lasers combined with the highest out-coupling efficiency of $T_{\text{out}} = 89\%$ and 99%, a slope efficiency versus absorbed pump power was obtained between 68% and 70%, regardless of the pumping wavelength and polarisation, with a maximum of 300 mW of output power. Between the different pumping wavelengths and polarisations, very similar results in terms of the output power and slope efficiency were obtained, with a slope efficiency versus absorbed pump power of just over 30% for $T_{out} = 2\%$, and $44 - 48\%$ for $T_{out} = 8\%$. The very high pump absorption efficiency of over 90% in single pass results in only a small difference between the slope efficiency versus launched pump power or versus absorbed pump power. Compared to the 5at.%-doped laser, the threshold at the low out-coupling of $T_{\text{out}} = 2\%$ increased to from 20 mW to 25 mW, whereas a threshold of 85 mW of absorbed pump power was measured in case no dielectric mirrors were butt-coupled to the end-facets.

The results of the 12at.% and 20at.%-doped lasers yield slightly lower slope efficiency than the 8at.%-doped waveguide lasers. The highest measured slope efficiency was 62% in case of $T_{\text{out}} = 89\%$ of out-coupling, for the 20at.%-doped channels. The lower efficiency could be the result of a lesser channel waveguide quality, which introduce loss, or the result of quenching processes owing to the higher thulium dopant concentration. The quantum efficiency $\eta_q = 1.94$ as a result of cross-relaxation cannot increase much more as the maximum value for η_q equals 2. It is expected that up-conversion processes that bleach the upper laser level become increasingly efficient as the thulium concentration increases beyond 8at.%, which results in a lower slope efficiency.

Similar to the 1.5at.%-doped laser, a shift in operating wavelength as a function of the used out-coupling transmission was also measured for the 5at.% and 8at.% thulium-doped channel waveguide lasers. Only the results of the 8.at%-doped laser are presented in figure 4.13, because it demonstrated the longest operating wavelength. The longest operating wavelength, and clearly multi-longitudinal-mode operation of the laser because of the multiple wavelengths being present simultaneously, was found when using $T_{\text{out}} = 2\%$ of out-coupling. In this configuration, the laser was oscillating at a frequency very close to 2 µm, with at least one longitudinal mode oscillating at a wavelength of 2037 nm. When selecting an out-coupling transmission of $T_{\text{out}} = 8\%$, the laser shifted towards 1940 nm, and further to around 1840 nm in case a high out-coupling transmission of $T_{\text{out}} = 89\%$ or 99% was used. The longer operating wavelength of this 8at.%-doped laser compared to the 1.5at.%-doped laser can be explained by the fact that the ratio of internal gain over the cavity losses of the former laser is favourable compared to the latter. It was noted that in case a low out-coupling transmission of 2% and 8% was used, the laser operating wavelength was shifting by several tens of nanometers because of the thermal and mechanical vibrations in the setup, in combination with the flat gain cross-section of thulium in double tungstate in this wavelength region.

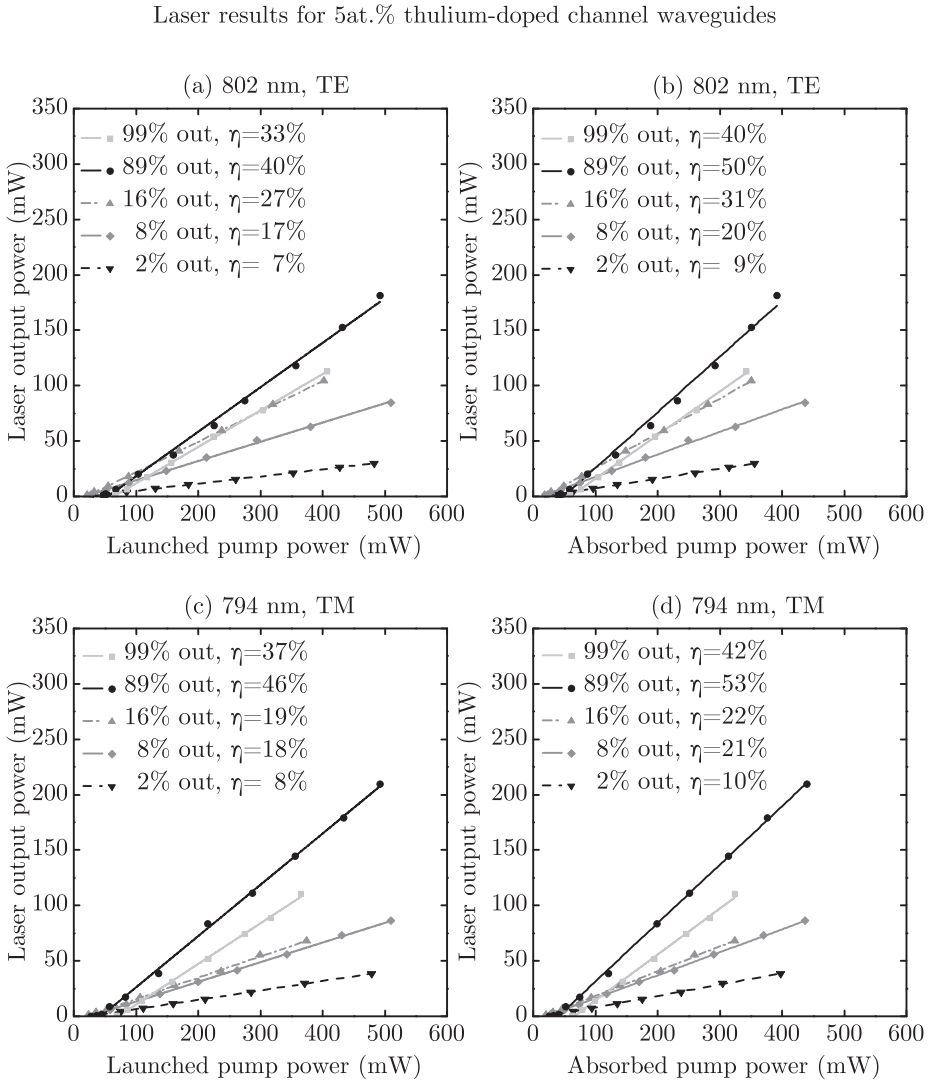

Figure 4.9 Laser output power versus launched and absorbed pump power for a 5at.%-doped thulium laser. The laser was pumped at 802 nm in TE polarisation (a,b), and 794 nm in TM polarisation (c,d). The output power is plotted as a function of launched pump power (a,c) and absorbed pump power (b,d). A maximum slope efficiency of 53% versus absorbed pump power was achieved for a high out-coupling efficiency of 89%.

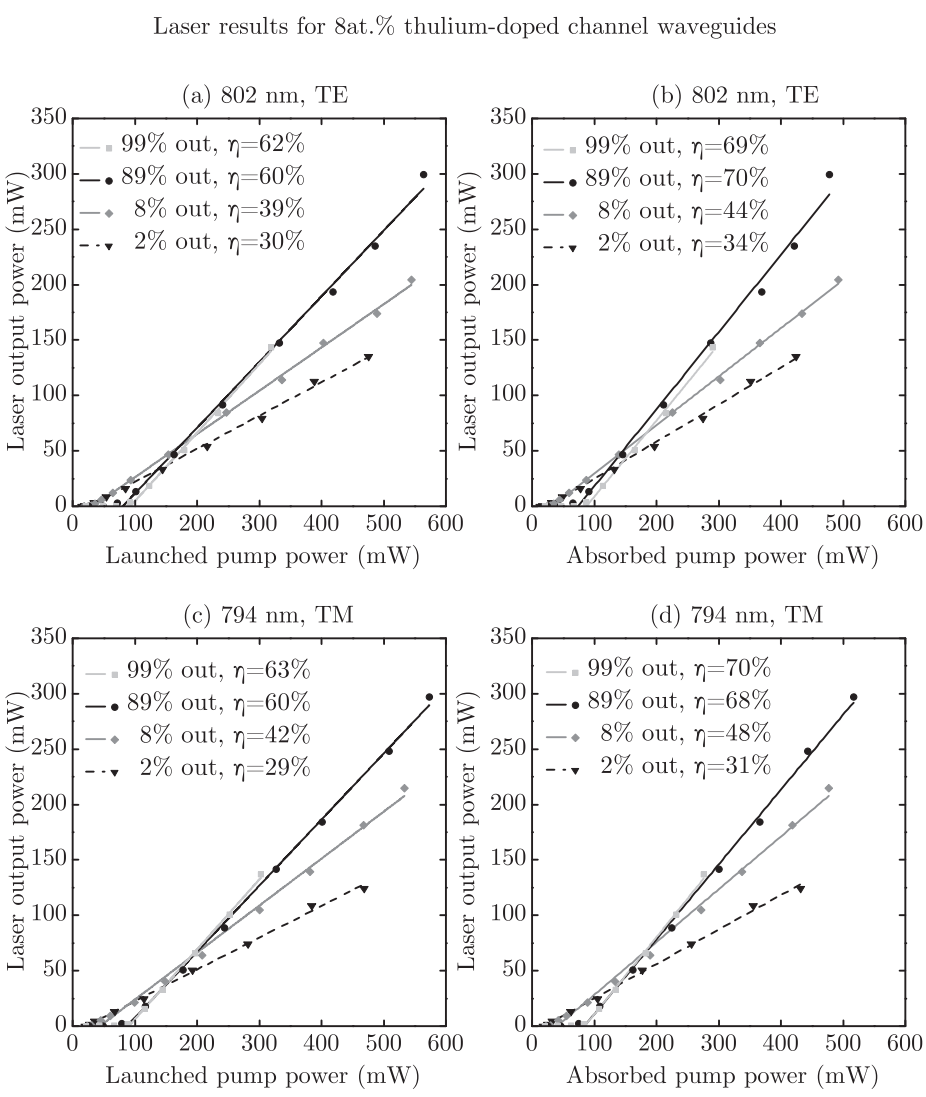

Figure 4.10 Laser output power versus launched and absorbed pump power for a 8at.%-doped thulium laser. The laser was pumped at 802 nm in TE polarisation (a,b), and 794 nm in TM polarisation (c,d). The output power is plotted as a function of launched pump power (a,c) and absorbed pump power (b,d). In the waveguides with a length of 4.3 mm, approximately 90% of the launched pump power was absorbed. A maximum slope efficiency of 70% versus absorbed pump power was achieved for a high out-coupling transmission of $T_{\text{out}} = 89\%$ and 99%.

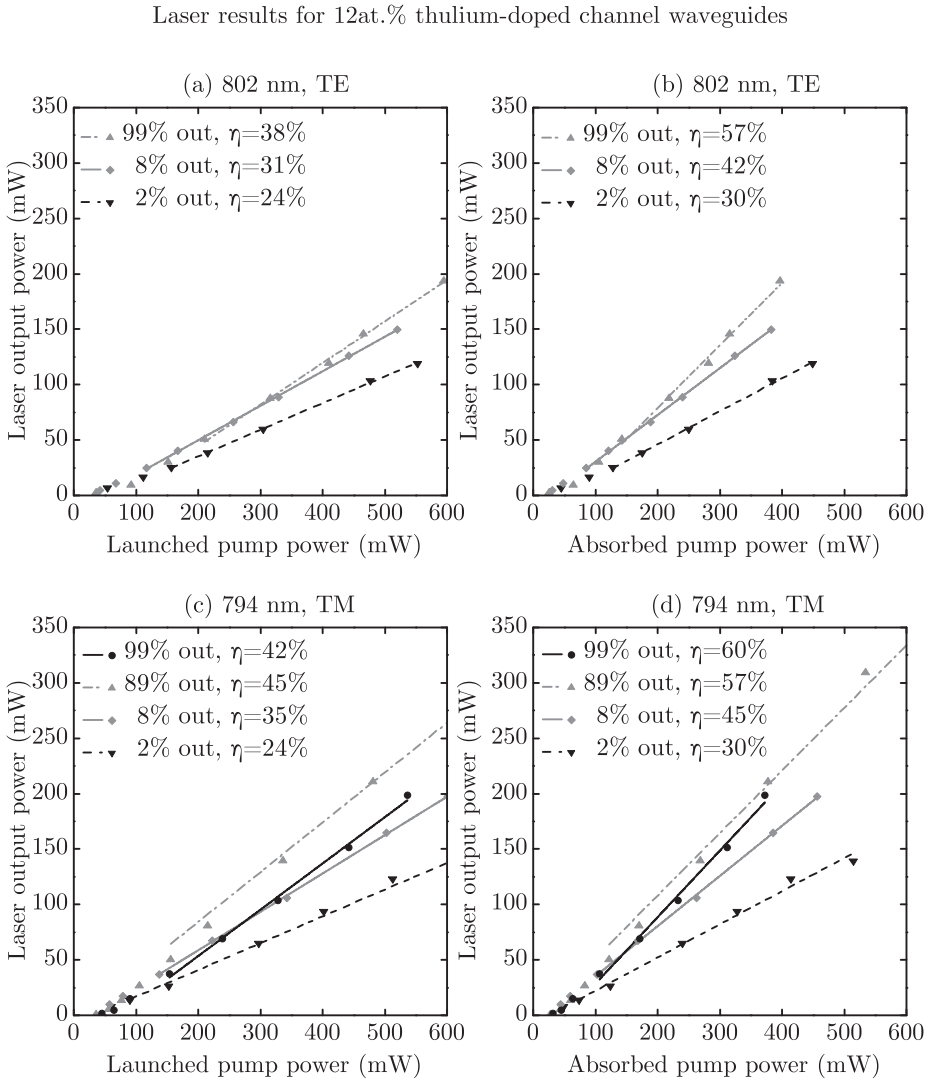

Figure 4.11 Laser output power versus launched and absorbed pump power for a 12at.%-doped thulium laser. The laser was pumped at 802 nm in TE polarisation (a,b), and 794 nm in TM polarisation (c,d). The output power is plotted as a function of launched pump power (a,c) and absorbed pump power (b,d). A maximum slope efficiency of 60% versus absorbed pump power was achieved for a high out-coupling transmission of $T_{\text{out}} = 99\%$.

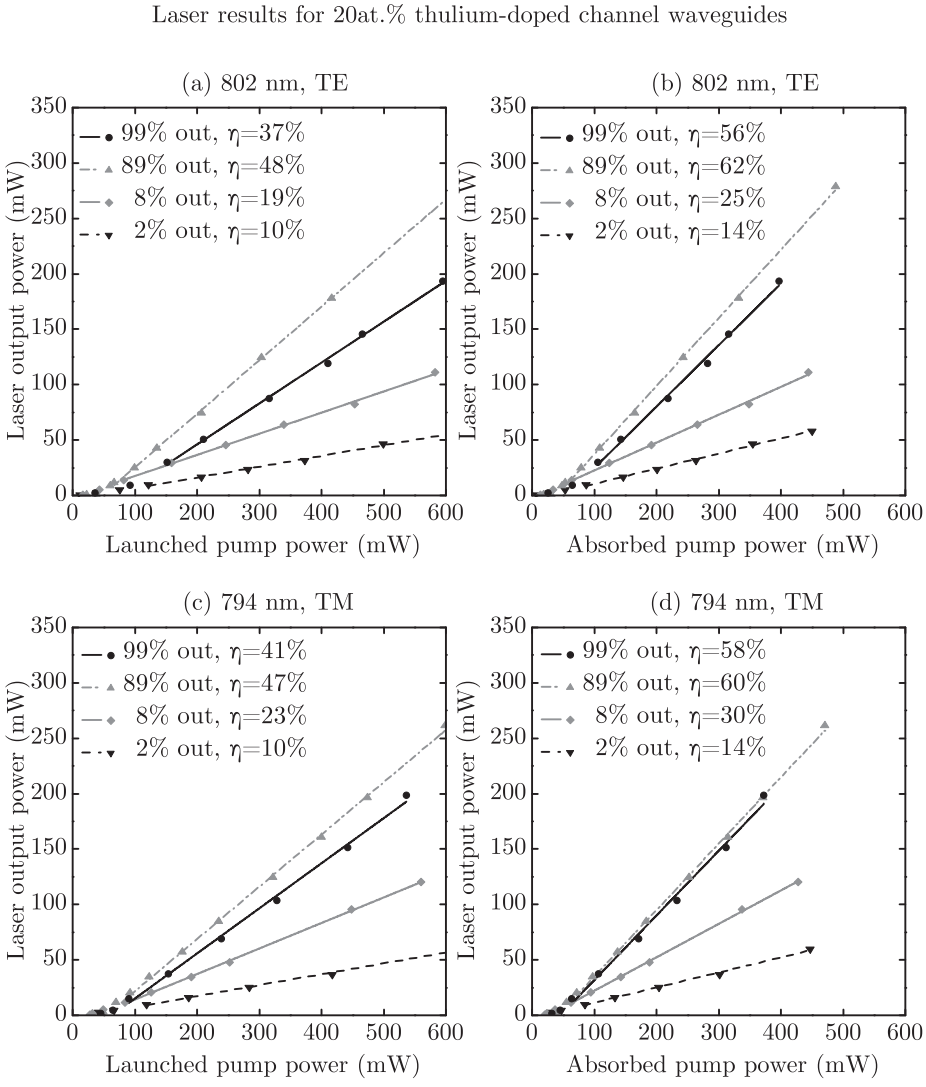

Figure 4.12 Laser output power versus launched and absorbed pump power for a 20at.%-doped thulium laser. The laser was pumped at 802 nm in TE polarisation (a,b), and 794 nm in TM polarisation (c,d). The output power is plotted as a function of launched pump power (a,c) and absorbed pump power (b,d). A maximum slope efficiency of 62% versus absorbed pump power was achieved for a high out-coupling transmission of $T_{\text{out}} = 89\%$.

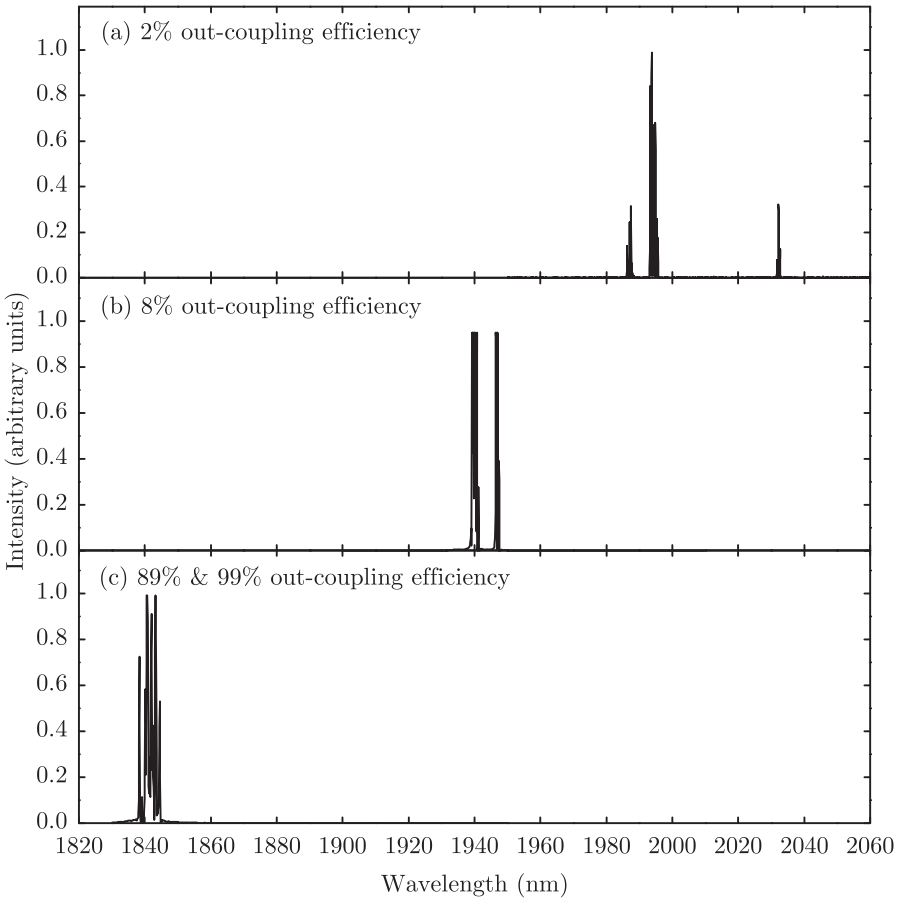

Figure 4.13 Measured laser operating wavelength for a 8at.%-doped thulium laser. The measured laser wavelength was dependent on the out-coupling transmission. The laser operating wavelength and out-coupling transmission combinations are (a) around 2 µm, with a maximum of 2037 nm for $T_{\text{out}} = 2\%$ of out-coupling, (b) $1940 - 1950$ nm for $T_{\text{out}} = 8\%$ of out-coupling, and (c) around 1840 nm for a high out-coupling transmission of $T_{\text{out}} = 89\%$ and 99%.

Power-scaling of 8at.% thulium-doped channel waveguide lasers

The highest measured slope efficiencies as a function of the dopant concentration of the five laser samples discussed in paragraph 4.1 and in this paragraph are shown in figure 4.14. From equation 3.46, it is known that the slope efficiency of a laser depends on many factors, such as the pump efficiency η_p, the quantum efficiency η_q, the Stokes efficiency $\eta_{St.}$, the efficiency with which pump photons are converted to laser photons dF/dS, and the out-coupling efficiency η_{out}. Between the different lasers measured, η_p has changed because of the dopant concentration and the different channel lengths, and η_{out} has been varied by using different out-coupling mirror configurations. By plotting the slope efficiency versus absorbed pump power for the different laser samples and out-coupling configurations measured in figure 4.14, a comparison between the different lasers becomes independent of the factor η_p (refer to eqn. 3.41). Despite the fact that dS/dF and $\eta_{St.}$ are each nearly identical between the different measured lasers, a large increase of the maximum measured slope efficiency is demonstrated as the Tm^{3+} concentration increases until 8at.%, upon comparing the lasers with identical out-coupling mirror configurations. This can only be explained by an increase of the internal efficiency of the laser, such as the increase of the quantum efficiency, η_q, resulting from an increase of the ion-ion cross-relaxation efficiency. The slope efficiency obtains its peak value of 70% (or 80% at higher pump powers as explained later), at thulium dopant concentrations of 8at.%, whereas it is lowered for even increased thulium dopant concentrations towards 12at.% and 20at.%. Quenching effects such as up-conversion or detrimental cross-relaxation into other levels than the $^3F_4$ upper laser level could be the reason for this decrease in slope efficiency, since less ions are available for the gain on the laser transition.

Whereas the demonstrated slope efficiency of 70% of the 8at.%-doped thulium laser was a very good result, the output power of this laser was only several hundreds of milliwatts. However, after again reviewing the 1.5at.%-doped laser results, it was realised that these lasers had already been tested with over 1 Watt of pump power, resulting in no damage to the laser end-facets. For that reason, and since our used Ti:Sapphire laser produces up to 3 Watts of power at 800 nm, the aim was to investigate the maximum obtainable output of the best-performing 8at.%-doped laser.

Two separate measurements have been performed and the results are shown in figure 4.15. These measurements have been obtained when using only a pump wavelength of 794 nm and TM polarisation, since the pumping wavelength and polarisation does not have a significant influence of the performance of this laser, according to the previously measured results of figure 4.10. Due to the high out-coupling transmission of $T_{out} = 89\%$, the laser was operating at the central line of 1840 nm, which is the transition from the lowest to lowest crystal-field

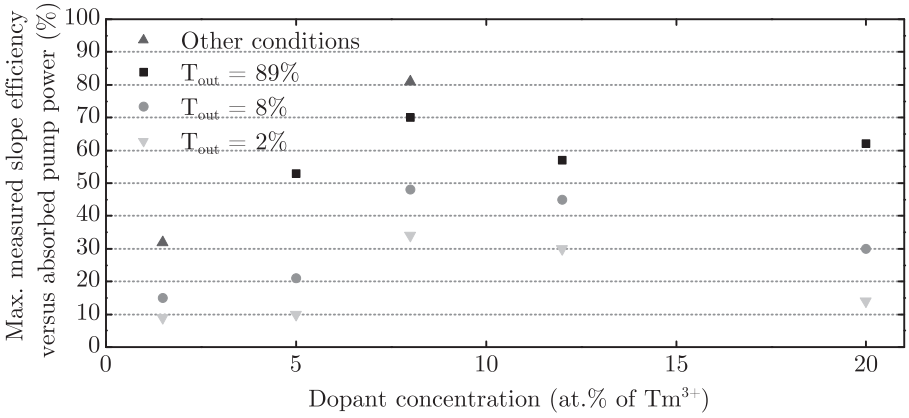

Figure 4.14 Highest measured slope efficiency as a function of the Tm^{3+} dopant concentration and out-coupling mirror configurations The 'other conditions' refer to the used 15% out-coupling transmission and launched pump powers beyond 1 Watt for the 1.5at.%-doped laser, and 89% of out-coupling and pump powers up to 3 Watts (power-scaled) for the 8at.%-doped lasers. The measured higher slope efficiency for increasing Tm^{3+} concentration until 8at.% (compared between identical mirror configurations) is a result of the higher dopant concentration and related cross-relaxation efficiency.

level of the electronic multiplets. The input-output curves of the measurements displayed in figure 4.15 at lower pump powers up to 600 mW are identical to the results of the other, independent measurements shown in figure 4.10. The maximum measured output power was approximately 1.6 W for an absorbed pump power of approximately 2.3 W, with a threshold of just over 50 mW of absorbed pump power. A linear fit of the measured data resulted in a maximum slope efficiency of $75 \pm 3\%$ and $81 \pm 3\%$ for measurements 1 and 2, respectively, obtained for pump powers beyond approximately 0.8 W. At $300 - 800$ mW of absorbed pump power, where the input-output curve is rounded, a linear fit yields a slope efficiency of 72% and 75% for measurements 1 and 2, respectively. The difference in laser performance between these two measurements is likely because of small differences in the butt-coupling of the mirror to the waveguide end-facet and/or the coupling of pump light to the pump waveguide mode. During the measurements, the output power from the used Ti:Sapphire laser was found to fluctuate by $\pm 1\%$. While this is not a large fluctuation, a significantly larger error accumulates in the calculation of absorbed pump power and laser output power, which are indicated by the error bars in figure 4.15.

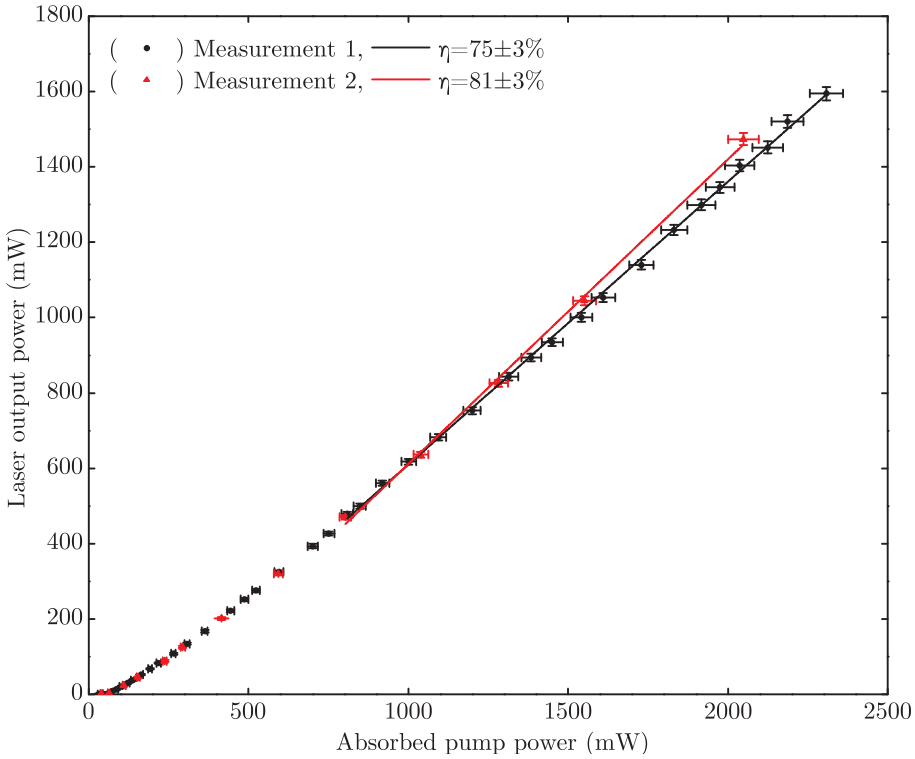

Figure 4.15 Laser output power versus absorbed pump power for a 8at.%-doped thulium laser. The results of two separate measurements have been displayed, yielding a slope efficiency of 75±3% and 81 ± 3% for the two measurements. The error bars stem from the fluctuations of the pump laser.

The measured efficiency in relation to the maximum theoretical slope efficiency of thulium-doped lasers

The theoretical limit of the slope efficiency depends, partly, on the pump quantum efficiency η_q that is influenced by the cross-relaxation process from ($^3H_4$,$^3H_6$) to ($^3F_4$,$^3F_4$). In paragraph 4.2.2, a value for the cross-relaxation rate parameter of $W_{CR} = 1.27\times10^{-16}$ cm^3 s^{-1} was derived for the thulium dopant concentration of 8at.% (=5.07×10^{20} cm^{-3}) of the best-performing channel waveguide laser. The quantum efficiency η_q as a result of pumping at 794 nm, defined as the number of ions excited into the upper laser level ($^3F_4$) per one pump photon absorbed, was defined in equation 4.3:

$$\eta_q = 1 + \frac{W_{CR}N_0}{1/\tau_3 + W_{CR}N_0}. \tag{4.4}$$

The maximum quantum efficiency equals $\eta_q = 1.94$ for $W_{\mathrm{CR}} = 1.27 \times 10^{-16}$ cm^3 s^{-1} in case ground-state bleaching is absent ($N_0 = N_{\mathrm{d}}$). For increasing ground-state bleaching, the maximum quantum efficiency decreases from this value.

The maximum slope efficiency versus absorbed pump power of the 8at.% thulium-doped laser according to equation 3.46 is calculated as the product of the Stokes efficiency of $\eta_{\mathrm{St}} = \lambda_p/\lambda_l = 794\mathrm{nm}/\ 1840\mathrm{nm} = 0.432$, the quantum efficiency of $\eta_q = 1.94$, and the output-coupling efficiency:

$$\eta_{\mathrm{out}} = \frac{\delta_{\mathrm{out}}}{\delta} \tag{4.5}$$

$$= \frac{\ln(1 - T_{\mathrm{out}})}{\ln\left[(1 - T_{\mathrm{out}})(1 - L)\right]} \tag{4.6}$$

$$= \frac{\ln(1 - 0.89)}{\ln\left[(1 - 0.89)(1 - 0.04)\right]} \tag{4.7}$$

$$= 0.99 \tag{4.8}$$

In the calculation of the out-coupling efficiency, a value for the roundtrip loss of $L = 0.04$ (4%) is assumed, as measured in sub-section 4.1.3. The maximum slope efficiency as calculated using these values is 82.2%, in case the geometry of the waveguide is such that the maximum efficiency of conversion between pump photons to laser photons is reached, such that all excited ions are accessible to the oscillating photons at the laser wavelength ($dF/dS = 1$). It can be seen in figure 2.7 that according to simulations for the best-performing 8at.% thulium-doped waveguide with waveguide dimensions of 14.3×25 µm^2, the pump mode overlap with the active medium exceeds 98%, the laser mode overlap with the active medium exceeds 90% and the pump/laser mode overlap exceeds 90%. In figure 2.8 where these pump and laser modes have been plotted, it can be seen that for this waveguide the entire pumped region is accessible to the laser photons. It is therefore expected that the value of dF/dS for our laser is indeed close to unity. The measured slope efficiency of $81 \pm 3\%$ and $75 \pm 3\%$ is only slightly lower than the calculated theoretical limit of 82.2%.

The results of the high-power laser experiments for 8at.% doping have been plotted once more in figures 4.16a–d, with the blue and red dots representing the data of the results with $81 \pm 3\%$ and $75 \pm 3\%$ slope efficiency, respectively, along with the predicted input-output curves (dashed, black lines) of equation 3.47, based on the theory by Risk. The theoretical curves were calculated with the geometrical, cavity, and dopant parameters corresponding to the measured waveguide laser, and a quantum efficiency of $\eta_q = 1.94$. In figures 4.16a (zoom-in b), the roundtrip loss (excluding mirror out-coupling 'losses') amounts to $L = 4\%$, which is similar to the derived round-trip loss for the 1.5at.%-doped thulium laser discussed in paragraph 4.1.3. The calculated slope efficiency (black, dashed curve), is 81.7%, which is close to the maximum measured slope efficiency of $81 \pm 3\%$. However, whereas the maximum slope efficiency during the experiment

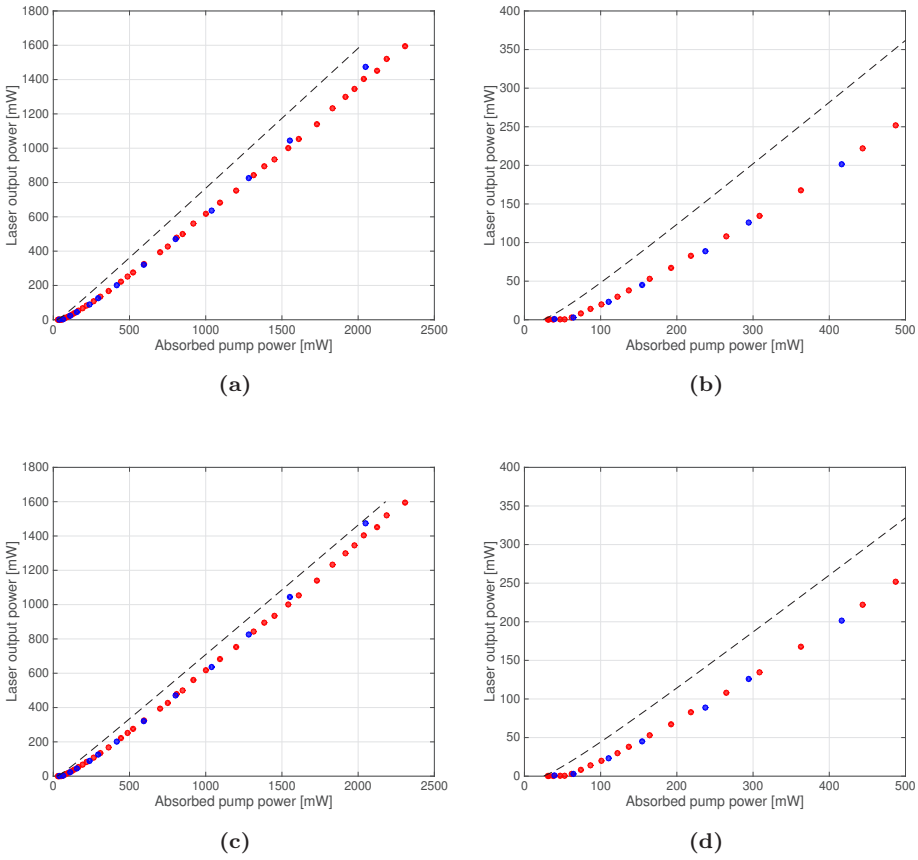

Figure 4.16 Theoretical and experimental input-output curves of a 8at.%-doped thulium channel waveguide laser. Shown are the results of the experiments yielding a slope efficiency of $81 \pm 3\%$ (blue dots) and $75 \pm 3\%$ (red dots), along with the theoretical input-output curve (dashed, black line). The theoretical curves have been calculated using a value for the quantum efficiency of $\eta_q = 1.94$ and a value for the round-trip losses of a,b) $L = 4\%$, yielding a maximum slope efficiency of 81% and c,d) $L = 20\%$, yielding a maximum slope efficiency of 75%.

is reached for pump powers beyond 1 Watt, the theory predicts that this slope efficiency is reached before 500 mW of pump power is absorbed. The laser threshold predicted by theory is approximately 30 mW, whereas in the experiment a value of over 50 mW was found.

In figures 4.16c,d, the results of the experiment have been plotted together with the calculated slope efficiency, based on a roundtrip loss of $L = 20\%$, while keeping all of the other parameters equal to the calculation of figures a,b. A higher round-trip loss could be the result of worse butt-coupling of the mirrors to the end-facets: for example as a result of the evaporation of index-matching fluid or the application of too much fluid. A maximum slope efficiency of 75.7% is calculated using these parameters, which is similar to the results of the measurement with a slope efficiency of $75 \pm 3\%$, depicted by the red dots.

From the graphs it is clear that the laser threshold is underestimated and that the slope efficiency at low pump powers are overestimated, which results in a horizontal offset between the calculated and experimental curves at higher pump powers (> 1 W), where the experimental slope efficiency matches the predicted slope efficiency.

The deviation between the theory and the experiment lies only in the ramp-up region, where the efficiency predicted by theory is higher than measured. According to equation 3.46, the increasing slope efficiency with increasing absorbed pump power during the experiment can only take place as a result of a better Stokes efficiency η_{St}, an increased ratio of useful loss over total loss η_{out}, an increased quantum efficiency η_q, or a better conversion efficiency dF/dS of pump photon energy to laser photon energy, which is influenced by the pump and laser mode overlap and the amount of laser reabsorption.

The laser spectra measured during the experiment with large out-coupling degree showed several peaks at an operating wavelength between 1839 nm and 1846 nm, as shown in figure 4.13c. However, the effect of this frequency bandwidth on the Stokes efficiency is negligible, since the difference of operating wavelength of the laser between 1839 to 1846 nm during the experiment, represents a change of the Stokes efficiency of only $\Delta\eta_{St} = \Delta\lambda_l \left|\frac{\lambda_p}{\lambda_l^2}\right| = 7\text{nm}\left|\frac{794\text{nm}}{(1840\text{nm})^2}\right| \approx 0.2\%$. During the experiment, the ratio of η_{out} has not changed: no other mirrors have been attached, and the intrinsic roundtrip loss is a fixed value determined by scattering loss inside the channel waveguide. This rules out the possibility of an increased slope efficiency as a result of an increase of the Stokes efficiency or a better out-coupling efficiency.

As explained in subsection 3.2.3, dF/dS changes as a function of the overlap of the pump and laser modes, and the pump power since thulium is a quasi-three-level laser which exhibits reabsorption on the laser transition. During pumping of the laser, heat is generated because of several effects: the first is that due to the quantum defect, defined as the difference in energy between a pump photon and a laser photon, heat is generated when as a result of multi-phonon decay an

ion de-excites from the pump level into the upper laser level. Another possibility for the generation of heat is that in the thulium laser, the dominant exothermic cross-relaxation process W_{CR} takes place, which also generates phonons and therefore heat. As a result of the generated heat and the resulting higher temperature of waveguide, the refractive index of the waveguide changes. In table 1.1 is shown that potassium double tungstates exhibit a negative dn/dT on the order of 10^{-5} K^{-1} depending on the wavelength, the composition of the crystal and the polarisation [31]. For the 8at.% thulium-doped waveguide, with the composition used of $\mathrm{KY}_{0.4}\mathrm{Gd}_{0.29}\mathrm{Lu}_{0.23}\mathrm{Tm}_{0.08}$, a refractive index change as a function of temperature of approximately $dn/dT = -15 \times 10^{-}6$ K^{-1} for the pump mode at 794 in TM polarisation and approximately $dn/dT = -10 \times 10^{-}6$ K^{-1} for the laser at 1840 nm in TE polarisation was calculated, by plugging-in the values of dn/dT (obtained from [31]) for the pure compounds in equation 2.2. The refractive index contrast of the thulium-doped core with the substrate and the cladding is approximately 1.1×10^{-2} at the pump wavelength of 794 nm and TM polarisation, and approximately 0.6×10^{-2} at the laser wavelength of 1840 nm in TE polarisation. In case it is assumed that the temperature increase within the channel waveguide is 100 K compared to the cladding and substrate, the refractive index of the core layer, and therefore the refractive index contrast of the channel waveguide for the pump mode is lowered by -1.5×10^{-3} or $-1.5/11 = -14\%$, and for the laser mode by -1×10^{-3} or $-1/6 = -17\%$. This means that both the pump and laser mode will expand by approximately the same amount, which does not significantly affect their beam overlap ratio w_p/w_l and therefore dS/dF. As a result of the increased pump and laser beam ratio, however, the threshold is increased. While the calculated decrease of the refractive index contrast for the pump and laser modes is based on a 100 K 'step-function' temperature increase, in reality the heat diffuses radially outward, so that both the core layer, as well as the substrate and cladding layer become heated, and the change of refractive-index contrast is lower than in the calculation.

According to equation 3.46, the final parameter that could influence the slope efficiency is the quantum efficiency η_q. In graph 4.16, a fixed quantum efficiency of $\eta_q = 1.94$ as a result of cross-relaxation in the laser is used. Consequently, this fixed quantum efficiency η_q cannot help to explain the rounded input-output curve in graph 4.16, where the threshold is underestimated by theory, and the slope efficiency at threshold is overestimated by theory.

Several attempts have been made to simulate the long ramp-up section in the measured laser results. According to Rustad and Stenersen, the effect of upconversion, will shift the threshold of a laser to a higher value, since effectively the quantum efficiency η_q is reduced. This can in part explain the higher threshold seen in the measured data in figures 4.16b,d, but not the higher slope efficiency as the absorbed pump power increases [123]. In fact, as a result of higher upconversion, the slope efficiency is reduced, which is also expected to be the case

for the thulium-doped lasers with a dopant concentration higher than 8at.%, in this work.

As explained above, the temperature of the waveguide with increasing pump power increases as a result of the quantum defect that is bridged by multi-phonon decay, or alternatively via an exothermic cross-relaxation process which also generates phonons. When simulating an increased pump and laser beam radius as a result of this, the pump threshold increases, as expected, but the slope efficiency, as expected, does not increase for higher pump powers.

A possibility for the increasing slope efficiency as a function of absorbed pump power could be a temperature-dependent cross-relaxation rate, and therefore a temperature-dependent quantum efficiency, which increases as the temperature increases. To test this hypothesis, a quantification of the cross-relaxation process for different temperatures is required through the measurement of luminescence decay curves from the pump level to determine if the pump level is increasingly quenched as the temperature increases.

4.3 Tunable lasers via an extended cavity in Littrow configuration

In the previous sections, lasers have been demonstrated which exhibited different operating wavelengths depending on the out-coupling mirror configuration. In this way, once the mirrors are fixed to the end-facets, the laser wavelength is also fixed. Therefore, an experiment was conducted in an attempt to create a continuously tuned laser by means of an external blazed grating in Littrow configuration. For this experiment the 8at.% thulium-doped sample of the previous section was used.

The usual setup for assessing the laser performance of a channel waveguide was modified and shown in figure 4.17. The laser beam was out-coupled from the waveguide and collimated using an out-coupling microscope objective with a NA= 0.25, and reflected back by a blazed diffraction grating consisting of 450 grooves per millimeter, a blaze wavelength of 3.1 µm, and a reflection efficiency for the first-order diffraction close to 85% for perpendicular polarisation at 2 µm (Thorlabs GR1325). A beam-splitter cube in combination with an out-coupling mirror of $T_{out} = 2\%$ placed at the pump-incoupling end facet and an optical spectrometer was used to determine the laser wavelength. Experiments have been performed with and without dielectric mirrors butt-coupled to the other end-facet. The same pump and in-coupling optics were used as for the previous laser experiments.

The results of the experiment are shown in figure 4.18. During the experiment with only a mirror with $T_{out} = 2\%$ placed at the pump-incoupling end facet and no mirror placed at the other end-facet, sufficient feedback from the blazed grating could be obtained to perform continuous tuning of the operating wavelength between $1810 - 1950$ nm, by rotating the blazed grating. The laser was operating at multiple longitudinal modes during the tuning experiment, indicated by the fact that in addition to the dominant modes at 1810 nm, 1860 nm and 1900 nm up to 1950 nm, weaker optical intensity was (often) recorded between $1840 - 1850$ nm. An explanation for this could be the high gain of the laser, indicated by highly efficient operation of the laser even without dielectric mirrors as shown in the previous paragraph, in combination with spatial hole burning effects that allow simultaneous operation of the $1840 - 1850$ nm modes and other modes.

An attempt to tune the laser to longer operating wavelengths was made by butt-coupling a second dielectric mirror with $T_{out} = 2\%$ to the other end-facet. The operating wavelength of the laser shifted to beyond 2000 nm and up to 2040 nm, but no significant, if any, effect as a result of rotating the external blazed grating could be measured. The feedback of the external blazed grating is strongly mitigated by reflection of the intensity off the dielectric mirror.

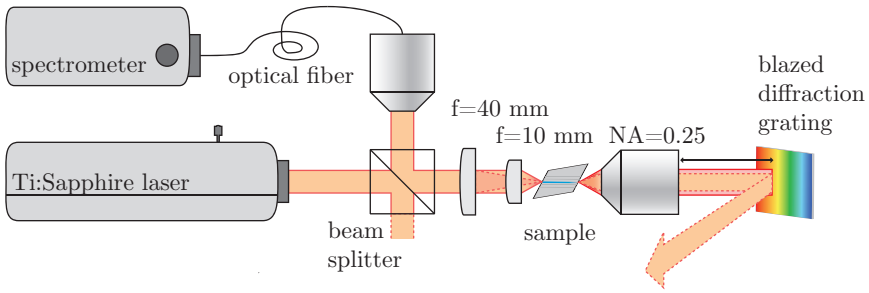

Figure 4.17 Experimental setup for a tuneable laser via an external cavity in a Littrow configuration. Laser light from a tuneable titanium-sapphire pump laser, emitting at a wavelength of around 800 nm, is focussed into a channel waveguide by two cylindrical lenses with focal lengths of 40 mm (horizontal) and 10 mm (vertical). A dielectric mirror with a reflectivity of $R = 99.9\%$ is attached to the pump in-coupling end-facet only, such that most of the generated laser light is exiting the channel from the other end-facet, and collimated using an out-coupling microscope lens with a numerical aperture of 0.25. An external, blazed, diffraction grating operating on the first diffraction order is used to force the laser to operate at the wavelength selected between $1800 - 2050$ nm, by reflecting this light back into the waveguide. Laser light out-coupled at the front is focussed into an optical fibre connected to a spectrometer which is used to record the wavelength the laser is operated on.

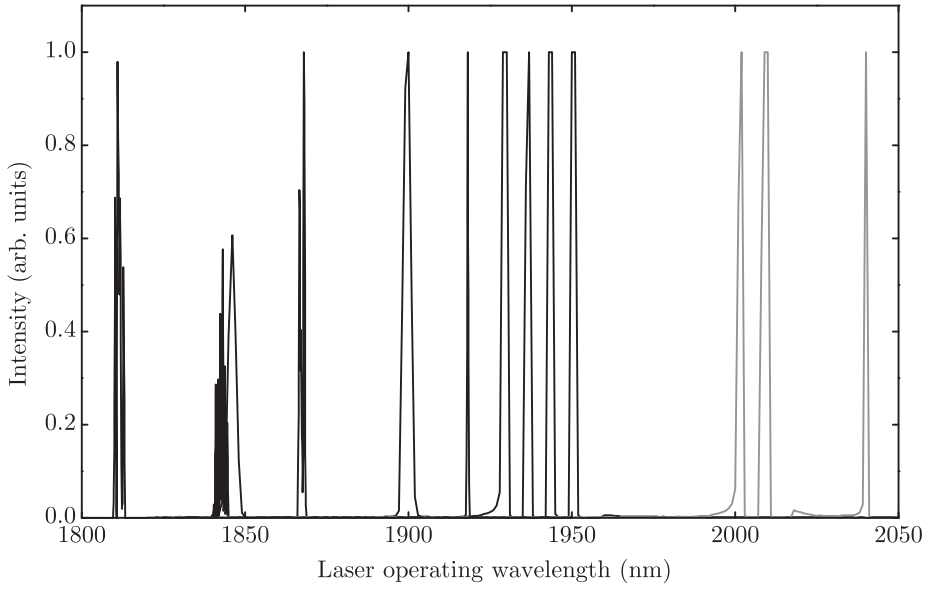

Figure 4.18 Tuned wavelength of a thulium laser by using an external blazed diffraction grating. The 8at.% thulium-doped sample was placed in an extended cavity with a blazed diffraction grating and a $T_{out} = 2\%$ dielectric out-coupling mirror at the pump in-coupling waveguide end-facet. By rotating the external blazed grating, the laser operating wavelength could be tuned between $1810 - 1950$ nm (black spectra). By attaching a second dielectric mirror of $T_{out} = 2\%$ to the other waveguide end-facet, a maximum operating wavelength of 2040 nm was obtained (gray spectra). The laser operated on multiple longitudinal modes, probably as a result of feedback from the Fresnel reflection of the end-facet in combination with high gain and spatial hole burning.

CHAPTER 5

Summary and Outlook

5.1 Summary

This thesis concerns the development of a high-power 2-µm buried channel waveguide laser in a potassium double tungstate host material. This particular host material has been selected because of its high transition cross-sections and ability for high dopant concentrations of rare-earth ions. When co-doping with gadolinium and lutetium, a relatively high refractive index contrast is obtained which allows the fabrication of small form factor, micro-channel waveguide lasers.

At the Integrated Optics and MicroSystems group, growth of thulium-doped yttrium-gadolinium-lutetium-co-doped layers onto a pure $KY(WO_4)_2$ substrate by liquid-phase epitaxy was performed by Dr Aravazhi. These layers are lapped and polished to the right thickness and afterwards argon-beam milled, using a process developed by Dr. Geskus, after photo-definition of channel waveguides, and overgrown with a pure $KY(WO_4)_2$ cladding layer. The concentration of the co-dopants and the dimensions of the buried channel waveguide are chosen such that the overlap between pump and laser optical modes is maximised, whilst preventing lattice stress and cracking of the layers and ensuring single-transverse-mode operation at both the pump and laser frequency. For this, the refractive indices of a variety of crystal compositions have been measured and simulations regarding the optical distribution as a function of waveguide dimensions have been performed and presented in chapter 2. The channels fabricated in this work have a width of $7.5 - 25$ µm and a width of $6 - 14$ µm, based on a maximum refractive-index contrast of 1.2×10^{-2}, and have been measured to exhibit a maximum propagation loss of 0.1 ± 0.03 dB/cm near 2 µm.

The efficiency of thulium-doped lasers hinges on the efficiency of non-linear two-ion processes, in case the laser is pumped at 800 into the $^3H_4$ manifold. In chapter 3 processes which influence the slope efficiency of a thulium laser are explained, such as dopant-concentration-dependent cross-relaxation and up-conversion, and geometrical factors such a pump and laser optical mode overlap which is very important in these three-level lasers because of their reabsorption on the laser transition. Based on this theory, predictions for the threshold and efficiency of the designed lasers could be made, using literature data such as absorption and emission cross-sections, and measured data such as lifetimes. In addition,

the theory was used to derive parameters such as the waveguide propagation loss based on relaxation-oscillation measurements, and the cross-relaxation rate parameter from concentration-dependent fluorescence lifetime data.

A variety of buried, channel waveguides with thulium dopant concentrations of 1.5, 5, 8, 12 and 20at.% have been fabricated and laser experiments performed, using a Ti:sapphire laser near 800 nm. All channel waveguides were tested using butt-coupled dielectric mirrors with a combined out-coupling transmission up to 89%. Due to the high gain in these channel waveguides, lasing has also been achieved for channels with thulium concentrations higher than 1.5at.% if no mirrors were attached, resulting in an out-coupling transmission of 99%. Laser operation has been achieved for the 1.5at.%-doped channels with a maximum value for the slope efficiency of 31.5% and a maximum output power of 149 mW if an out-coupling transmission of 16% was used. These lasers exhibited a pump power threshold as low as 7 mW, due to the small transverse cross-section, relatively low dopant concentration, low propagation loss, and a relatively low degree of out-coupling transmission.

For the channel waveguide with 5at.% of thulium, a maximum slope efficiency of 53% has been found. The best results obtained with the 8at.%-doped channel waveguide laser in two separate measurements were a slope efficiency $75 \pm 3\%$ and $81 \pm 3\%$ and a maximum continuous-wave output power of 1.6 W for 2.3 W of absorbed pump power. These channels, with lateral dimensions of 14×25 μm^2, exhibited low threshold absorbed pump powers of just over 50 mW. To the best of our knowledge, these results represent the most efficient 2-µm channel waveguide laser to date. For the channel waveguide lasers doped with 12at.% and 20at.% of thulium, the best results were slope efficiencies of around 60% and several hundreds of milliwatts of output power.

The higher slope efficiency as the concentration is increased for the thulium lasers until 8at.% of thulium concentration in this work is a result of a higher cross-relaxation efficiency due to a shorter thulium ion-ion distance. The maximum value for the theoretical cross-relaxation rate parameter of 1.27×10^{-16} cm^3 s^-1 was derived from fluorescence decay measurement data, and results in a maximum quantum efficiency of $\eta_q = 1.94$ for the laser with 8at.% thulium dopant concentration. The experimentally found slope efficiency is close to the theoretical maximum of the slope efficiency of 83%, calculated using this quantum efficiency. For the thulium lasers with even higher dopant concentration, the quantum efficiency $\eta_q = 1.94$ as a result of cross-relaxation cannot increase much more as the maximum value for η_q equals 2. It is expected that up-conversion processes that bleach the upper laser level become increasingly efficient as the thulium concentration increases beyond 8at.%, which results in a lower slope efficiency.

Depending on the out-coupling transmission selectable by the dielectric mirrors, the laser output wavelength was found to shift between 1840 nm and 2037

nm, as a result of the varied threshold inversion. By using a blazed diffraction grating in Littrow configuration, tuning of the laser output wavelength between 1810 – 1950 nm has been achieved.

5.2 Outlook

The buried channel waveguide lasers presented in this work demonstrate excellent efficiency and output power from a device with a size of several millimeters. These lasers operated on multiple longitudinal modes and the wavelength was found to shift as a function of the out-coupling efficiency. The waveguide lasers were tested with butt-coupled dielectric mirrors using index-matching fluid, which is a short-term solution as the fluid tends to evaporate.

A step forward toward on-chip, monolithic lasers is the integration of mirrors on the chip itself, which allows for a more permanent and durable solution. In addition, using on-chip mirrors in the form on distributed-feedback, or distributed Bragg reflector gratings has the advantage that operation of the laser is reduced to a single longitudinal mode, with very narrow line-width and excellent stability [12, 21].

Figure 5.1 shows details of corrugated, strip-loaded silicon-nitride (SiN) channel waveguides on a planar double tungstate thulium-doped layer. The SiN strip-loaded channel acts as a corrugated cladding, which can confine the pump and laser modes and can provide optical feedback to support only a single longitudinal laser mode with a frequency that depends on the periodicity of the corrugation. In figure 5.1a a corrugated channel with a periodicity of 500 nm is shown, which, together with the effective refractive index of the guided mode, provides optical feedback at 2000 nm. In figure 5.1b a corrugated, third-order channel waveguide with a periodicity of 1.18 µm is shown, which is designed to provide feedback at 1550 nm. In figure 5.1c, a full chip with multiple corrugated, strip-loaded SiN channels is shown.

While the chip of figure 5.1 provided some feedback at 1550 nm, the response was ultimately too weak to provide sufficient feedback for lasing, or losses introduced by the strip-loaded grating were too high to reach threshold for lasing. Nevertheless, the integration of on-chip mirrors is a necessary step for monolithically integrated on-chip lasers on double tungstates and would open up possibilities to combine high output and efficiency from double tungstate lasers with narrow linewidth, and stability.

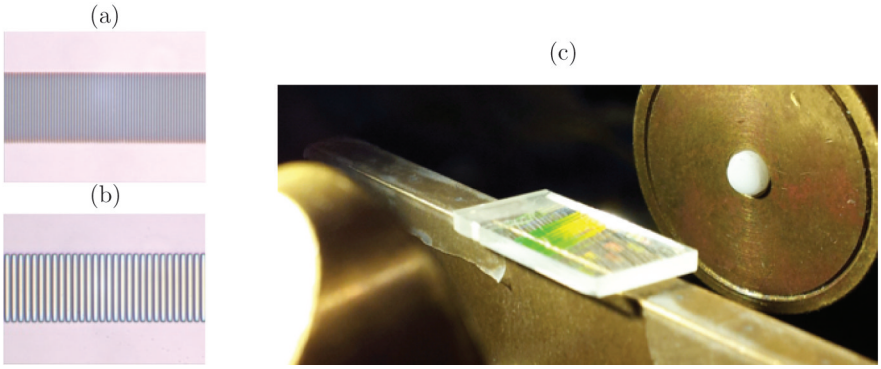

Figure 5.1 Double tungstate chip with on-chip resonant structures in SiN fabricated by electron-beam lithography. Detail of a corrugated, strip-loaded channel waveguide structure with a periodicity of (a) 500 nm, and (b) 1.18 µm. (c) Chip with several on-chip corrugated waveguides fabricated in SiN by electron-beam lithography and subsequent etching.

Abstract

The subject of this thesis is the development of 2-µm rare-earth lasers in thulium-doped yttrium-gadolinium-lutetium-co-doped potassium double tungstate film layers. These thulium-doped layers were grown onto undoped potassium yttrium double tungstates by liquid-phase epitaxy and were lapped and polished afterwards, prior to a photo-lithographic process to define channel waveguides. Channels were subsequently obtained by argon-beam milling of the samples, resulting in ridge-type channel waveguides. During another liquid-phase epitaxy growth these channels were overgrown with a double tungstate cladding to obtain buried channel waveguides. The concentration of the co-dopants and the dimensions of the buried channel waveguide are chosen such that the overlap between pump and laser optical modes is maximised, whilst preventing lattice stress and cracking of the layers and ensuring single-transverse-mode operation at both the pump and laser frequency. The fabricated channels on multiple samples have a width of $7.5 - 25$ µm and a height of $6.6 - 14.3$ µm, and have thulium dopant concentrations of $1.5 - 20$at.%.

Laser experiments on the channel waveguides were performed by using a Ti:-sapphire laser near 800 nm as the pumping source. The channel waveguides were tested with different out-coupling transmission of up to 89%, provided by various combinations of butt-coupled dielectric mirrors, or an out-coupling transmission of up to 99% in case no mirrors were used. For a 1.5% thulium-doped channel waveguide, a threshold of 7 mW, a slope efficiency of 31.5%, and an output power of 149 mW were measured and a value for the propagation loss of 0.1 ± 0.03 dB/cm at the lasing wavelength of 2 µm were derived from relaxation-oscillation measurements. Laser experiments on channel waveguides with a higher thulium dopant concentration of 5at.% yielded a maximum slope efficiency of 53%. The optimum thulium dopant concentration was 8at.% which yielded a maximum slope efficiency of 81 ± 3%, which is close to the theoretical maximum for this laser of 83%. An output power of 1.6 W was obtained from this laser for 2.3 W of absorbed pump power. The high efficiency is a result of cross-relaxation which increases the maximum quantum efficiency for this laser to $\eta_q = 1.94$. For higher thulium concentrations of 12at.% and 20at.%, the maximum obtained slope efficiency was 60%.

Depending on the out-coupling transmission selectable by the dielectric mirrors, the laser output wavelength was found to shift between 1840 nm and 2037 nm, as a result of the varied threshold inversion. By using a blazed diffraction

grating in Littrow configuration, tuning of the laser output wavelength between $1810 - 1950$ nm has been achieved.

Nederlandse samenvatting

Het onderwerp van dit proefschrift betreft de ontwikkeling van zeldzame-aarde lasers in laagjes van thulium-gedoteerd yttrium-gadolinium-lutetium co-gedoteerd kalium-wolfraam-oxide. Deze thulium-gedoteerde lagen worden 'gegroeid' doormiddel van een laag-voor-laag kristalgroei proces waarbij een kristal in vaste vorm wordt ondergedompeld in een bad van gesmolten kristal met de gewenste samenstelling (in het Engels: liquid-phase epitaxy). Na het groeiproces worden de kristallen langzaam gekoeld en de nog ruwe lagen worden vervolgens tot de gewenste dikte geschuurd, en vervolgens gepolijst. Op deze gepolijste lagen wordt vervolgens een laagje van een licht-gevoelig materiaal (masker) aangebracht waarin patronen gemaakt kunnen worden doormiddel van licht; op plekken waar licht het masker raakt wordt het masker zo van samenstelling veranderd dat het oplosbaar wordt in vloeistof. Het niet-belichte, en daardoor niet in vloeistof opgeloste, gedeelte van het masker beschermt het onderliggende kristal tijdens het etsen. Het etsproces bestaat uit een ionen bombardement waarmee heel uniform een gedeelte van het kristal 'uitgegraven' wordt. Met dit proces zijn rechte kanalen gemaakt waarin het laserlicht kan geleiden. Deze kanalen worden vervolgens nog eenmaal overgroeid met ongedoteerd kristal, om de kanalen te beschermen en de optische eigenschappen van de kanalen te verbeteren. De dusdanig verkregen kanalen zijn $7.5 - 25$ µm breed, $6.6 - 14.3$ µm hoog, en hebben een thulium concentratie van $1.5 - 20$at.% (at.% betekent: als percentage van de totale hoeveelheid vervangbare atomen).

Laser experimenten op de verschillende kristallen zijn uitgevoerd met gebruikmaking van een titaan-saffier laser als de energiebron (pomp-bron), welke was afgesteld op een golflengte rond 800 nm. Verschillende types spiegels zijn gebruikt, waarbij een transmissie van laserlicht uit de kanalen tot wel 89% bereikt werd. Deze spiegels werden met behulp van een vloeistof tegen de uiteinden van de kanalen geplakt. De lasers konden zelfs getest worden zonder spiegels wat de hoge optische versterkingsfactor van het gebruikte kristal onderstreept. Kanalen met een thulium concentratie van 1.5at.% resulteerden in een laser met een efficiëntie van 31.5%, een vermogen van 149 mW en een drempelvermogen van 7 mW voor de pomp. De verliezen tengevolge van propagatie door de kanaalgolfgeleider zijn bepaald op 0.1 ± 0.03 dB/cm tijdens dit experiment. Laser experimenten met een kanaalgolfgeleider gedoteerd met 5at.% leverden een maximale efficiëntie op van 53%. Het beste resultaat werd verkregen met een 8at.% thulium-gedoteerde kkanaalgolfgeleider: een maximaal vermogen van 1.6 W met

een efficiëntie van 81% werd gemeten. Dit resultaat ligt zeer nabij de maximaal theoretische efficiëntie van 83% voor een thulium laser. Tevens is dit de meest efficiënte 2-µm kanaalgolfgeleider laser ooit gemeten. Deze hoge efficiëntie is het resultaat van een concentratie-afhankelijke ion-ion interactie die 'cross-relaxatie' wordt genoemd; een door een pomp photon aangeslagen thulium ion draagt energie over aan een nabijgelegen thulium ion zodanig dat beide ionen bijdragen aan de optische versterking op de lasergolflengte. De kanaalgolfgeleider lasers met een hogere thulium concentratie van 12at.% en 20at.% bereikten tijdens de experimenten een maximale efficiëntie van 60%. Deze lagere efficiëntie van thulium lasers bij een hogere concentratie dan 8at.% is vermoedelijk het gevolg van 'up-conversion' (excitatie naar een hoger energieniveau van een thulium ion tengevolge van overdracht van energie door een nabijgelegen thulium ion dat een lager energieniveau bereikt).

Afhankelijk van de mate van reflectie van de gebruikte spiegels was de laser golflengte tijdens de experimenten te variëren. Het bleek mogelijk de golflengte te controleren tussen de $1840 - 2037$ nm, als een direct resultaat van de wisselende drempelinversie van de thulium ionen. Door van het gebruik van een diffractierooster in Littrow configuratie kon de golflengte van de laser gevarieerd worden tussen de $1810 - 1950$ nm.

Bibliography

[1] Richard P. Feynman. Plenty of room at the bottom, December 1959. — p.1.

[2] Sebastianus A. Goorden, Marcel Horstmann, Allard P. Mosk, Boris Škorić, and Pepijn W. H. Pinkse. Quantum-secure authentication of a physical unclonable key. *Optica*, 1(6):421–424, Dec 2014. — p.1.

[3] M. J. Kobrinsky, B. A. Block, J. F. Zheng, B. C. Barnett, E. Mohammed, M. Reshotko, F. Robertson, S. List, I. Young, and K. Cadien. On-chip optical interconnects. *Intel Technology Journal*, 8:129–141, 2004. — p.1.

[4] N. Lindenmann, G. Balthasar, D. Hillerkuss, R. Schmogrow, M. Jordan, J. Leuthold, W. Freude, and C. Koos. Photonic wire bonding: a novel concept for chip-scale interconnects. *Optics Express*, 20(16):17667–17677, Jul 2012. — p.1.

[5] L. Chang, M. Dijkstra, N. Ismail, M. Pollnau, R. M. de Ridder, K. Wörhoff, V. Subramaniam, and J. S. Kanger. Waveguide-coupled micro-ball lens array suitable for mass fabrication. *Optics Express*, 23(17):22414–22423, Aug 2015. — p.1.

[6] Christos Grivas. Optically pumped planar waveguide lasers, part i: Fundamentals and fabrication techniques. *Progress in Quantum Electronics*, 35(6):159 – 239, June 2011. — p.2.

[7] Christos Grivas. Optically pumped planar waveguide lasers: Part ii: Gain media, laser systems, and applications. *Progress in Quantum Electronics*, 45–46:3–160, 2016/3// 2016. — p.2.

[8] Jonathan D. B. Bradley, Marcia Costa e Silva, Mathilde Gay, Laurent Bramerie, Alfred Driessen, Kerstin Wörhoff, Jean-Claude Simon, and Markus Pollnau. 170 gbit/s transmission in an erbium-doped waveguide amplifier on silicon. *Optics Express*, 17(24):22201–22208, Nov 2009. — p.2.

[9] J. D. Bradley, R. Stoffer, L. Agazzi, F. Ay, K. Wörhoff, and M. Pollnau. Integrated al2o3:er3+ ring lasers on silicon with wide wavelength selectivity. *Optics Letters*, 35(1):73–75, Jan 2010. — p.2.

[10] Sergio A. Vázquez-Córdova, Meindert Dijkstra, Edward H. Bernhardi, Feridun Ay, Kerstin Wörhoff, Jennifer L. Herek, Sonia M. García-Blanco, and Markus Pollnau. Erbium-doped spiral amplifiers with 20 db of net gain on silicon. *Optics Express*, 22(21):25993–26004, 2014. — p.2.

[11] J. Yang, K. van Dalfsen, K. Wörhoff, F. Ay, and M. Pollnau. High-gain al_2o_3:nd^{3+} channel waveguide amplifiers at 880 nm, 1060 nm, and 1330 nm. *Applied Physics B: Lasers and Optics*, 101(1-2):119–127, October 2010. — p.2.

[12] E. H. Bernhardi, H. A. G. M. van Wolferen, L. Agazzi, M. R. H. Khan, C. G. H. Roeloffzen, K. Wörhoff, M. Pollnau, and R. M. de Ridder. Ultra-narrow-linewidth, single-

frequency distributed feedback waveguide laser in $al_2o_3:er^{3+}$ on silicon. *Optics letters*, 35(14):2394–2396, July 2010. — p.2, 99.

[13] E. H. Bernhardi, M. R. H. Khan, C. G. H. Roeloffzen, H. A. G. M. van Wolferen, K. Wörhoff, R. M. de Ridder, and M. Pollnau. Photonic generation of stable microwave signals from a dual-wavelength $al_2o_3:yb^{3+}$ distributed-feedback waveguide laser. *Optics Letters*, 37(2):181–183, Jan 2012. — p.2.

[14] Edward H. Bernhardi, Kees O. van der Werf, Anton J. F. Hollink, Kerstin Wörhoff, René M. de Ridder, Vinod Subramaniam, and Markus Pollnau. Intra-laser-cavity microparticle sensing with a dual-wavelength distributed-feedback laser. *Laser and Photonics Reviews*, 7(4):589–598, 2013. — p.2.

[15] Christos Grivas, Jing Yang, Mart B.J. Diemeer, Alfred Driessen, and Markus Pollnau. Continuous-wave nd-doped polymer lasers. *Optics Letters*, 35(12):1983–1985, June 2010. — p.2.

[16] J. Yang, M.B.J. Diemeer, C. Grivas, G. Sengo, A. Driessen, and M. Pollnau. Steady-state lasing in a solid polymer. *Laser Physics Letters*, 7(9):650–656, 2010. — p.2.

[17] Chaitanya Dongre, Jasper van Weerd, Nicola Bellini, Roberto Osellame, Giulio Cerullo, Rob van Weeghel, Hugo J. W. M. Hoekstra, and Markus Pollnau. Dual-point dual-wavelength fluorescence monitoring of dna separation in a lab on a chip. *Biomedical Optics Express*, 1(2):729–735, Sep 2010. — p.2.

[18] Chaitanya Dongre, Jasper van Weerd, Geert A. J. Besselink, Rebeca Martinez Vazquez, Roberto Osellame, Giulio Cerullo, Rob van Weeghel, Hans H. van den Vlekkert, Hugo J. W. M. Hoekstra, and Markus Pollnau. Modulation-frequency encoded multi-color fluorescent dna analysis in an optofluidic chip. *Lab on a Chip*, 11:679–683, 2011. — p.2.

[19] B. I. Akca, B. Považay, A. Alex, K. Wörhoff, R. M. de Ridder, W. Drexler, and M. Pollnau. Miniature spectrometer and beam splitter for an optical coherence tomography on a silicon chip. *Optics Express*, 21(14):16648–16656, Jul 2013. — p.2.

[20] N. Ismail, L.-P. Choo-Smith, K. Wörhoff, A. Driessen, A. C. Baclig, P. J. Caspers, G. J. Puppels, R. M. de Ridder, and M. Pollnau. Raman spectroscopy with an integrated arrayed-waveguide grating. *Optics Letters*, 36(23):4629–4631, Dec 2011. — p.2.

[21] E. H. Bernhardi, H. A. G. M. van Wolferen, K. Wörhoff, R. M. de Ridder, and M. Pollnau. Highly efficient, low-threshold monolithic distributed-bragg-reflector channel waveguide laser in $al_2o_3:yb^{3+}$. *Optics Letters*, 36(5):603–605, Mar 2011. — p.2, 99.

[22] Jonathan D. B. Bradley and Ehsan Shah Hosseini. Monolithic erbium- and ytterbium-doped microring lasers on silicon chips. *Opt. Express*, 22(10):12226–12237, May 2014. — p.2.

[23] Jared F. Bauters, Martijn J. R. Heck, Demis John, Daoxin Dai, Ming-Chun Tien, Jonathon S. Barton, Arne Leinse, René G. Heideman, Daniel J. Blumenthal, and John E. Bowers. Ultra-low-loss high-aspect-ratio si_3n_4 waveguides. *Optics Express*, 19(4):3163–3174, Feb 2011. — p.2.

[24] J. P. Epping, T. Hellwig, M. Hoekman, R. Mateman, A. Leinse, R. G. Heideman, A. van Rees, P. J.M. van der Slot, C. J. Lee, C. Fallnich, and K.-J. Boller. On-chip visible-to-infrared supercontinuum generation with more than 495 thz spectral bandwidth. *Optics*

Express, 23(15):19596–19604, Jul 2015. — p.2.

[25] R M Oldenbeuving, E J Klein, H L Offerhaus, C J Lee, H Song, and K-J Boller. 25 khz narrow spectral bandwidth of a wavelength tunable diode laser with a short waveguide-based external cavity. *Laser Physics Letters*, 10(1):015804, 2013. — p.2.

[26] L. Agazzi, K. Wörhoff, and M. Pollnau. Energy-transfer-upconversion models, their applicability and breakdown in the presence of spectroscopically distinct ion classes: A case study in amorphous $al_2o_3:er^{3+}$. *The Journal of Physical Chemistry C*, 117(13):6759–6776, 2014/04/16 2013. — p.3, 50, 76.

[27] N. Ter-Gabrielyan, V. Fromzel, X. Mu, H. Meissner, and M. Dubinskii. Resonantly pumped single-mode channel waveguide er:yag laser with nearly quantum defect limited efficiency. *Optics Letters*, 38(14):2431–2433, Jul 2013. — p.3.

[28] K. Petermann, D. Fagundes-Peters, J. Johannsen, M. Mond, V. Peters, J.J. Romero, S. Kutovoi, J. Speiser, and A. Giesen. Highly yb-doped oxides for thin-disc lasers. *Journal of Crystal Growth*, 275(1–2):135 – 140, 2005. Proceedings of the 14th International Conference on Crystal Growth and the 12th International Conference on Vapor Growth and Epitaxy. — p.3, 4.

[29] R. Paschotta. Rp photonics encyclopedia, 2015. — p.4.

[30] Jakub W. Szela. *Planar waveguide lasers and spectroscopic study of upconversion solid-state materials*. PhD thesis, University of Southampton, January 2015. — p.4.

[31] P.A. Loiko, K.V. Yumashev, N.V. Kuleshov, G.E. Rachkovskaya, and A.A. Pavlyuk. Thermo-optic dispersion formulas for monoclinic double tungstates $kre(wo_4)_2$ where re=gd, y, lu, yb. *Optical Materials*, 33(11):1688 – 1694, 2011. — p.4, 91.

[32] Peter Klopp, Valentin Petrov, and Uwe Griebner. Potassium ytterbium tungstate provides the smallest laser quantum defect. *Japanese Journal of Applied Physics*, 42(3A):L246, 2003. — p.3.

[33] Markus Pollnau, Yaroslav E. Romanyuk, Florent Gardillou, Camelia N. Borca, Uwe Griebner, Simon Rivier, and Valentin Petrov. Double tungstate lasers: From bulk toward on-chip integrated waveguide devices. *IEEE Journal of Selected Topics in Quantum Electronics*, 13(3):661–671, 2007. — p.3.

[34] F. Brunner, T. Südmeyer, E. Innerhofer, F. Morier-Genoud, R. Paschotta, V. E. Kisel, V. G. Shcherbitsky, N. V. Kuleshov, J. Gao, K. Contag, A. Giesen, and U. Keller. 240-fs pulses with 22-W average power from a mode-locked thin-disk $Yb:KY(WO_4)_2$ laser. *Optics Letters*, 27(13):1162–1164, 2002. — p.3.

[35] Dimitri Geskus, Shanmugam Aravazhi, Sonia M. García-Blanco, and Markus Pollnau. Giant optical gain in a rare-earth-ion-doped microstructure. *Advanced Materials*, 24(10):OP19–OP22, March 2012. — p.3, 5.

[36] Y. S. Yong, S. Aravazhi, S. A. Vazquez-Cordova, S. M. García-Blanco, and M. Pollnau. 1050 db/cm gain in a 57.5at.% yb-doped $kgd(wo_4)_2$ thin film at 981 nm. In *Conference on Lasers and Electro-Optics Europe*, Munich, Germany, 2015. — p.3.

[37] Alexander A. Kaminskii, K. Ueda, Hans E. Eichler, Julian Findeisen, Sergei N. Bagayev, Fedor A. Kuznetsov, Alexsei A. Pavlyuk, Georges Boulon, and Frederic Bourgeois. Monoclinic tungstates $kdy(wo_4)_2$ and $klu(wo_4)_2$ - new $\chi^{(3)}$-active crystals for laser raman

shifters. *Japanese Journal of Applied Physics*, 37(Part 2, No. 8A):L923–L926, 1998. — p.4.

[38] Dimitri Geskus, Jonas Jakutis Neto, Saara-Maarit Reijn, Helen M. Pask, and Niklaus U. Wetter. Quasi-continuous wave raman lasers at 990 and 976 nm based on a three-level nd:ylf laser. *Optics Letters*, 39(10):2982–2985, May 2014. — p.4.

[39] A. E. Troshin, V. E. Kisel, A. S. Yasukevich, N. V. Kuleshov, A. A. Pavlyuk, E. B. Dunina, and A. A. Kornienko. Spectroscopy and laser properties of Tm^{3+}:$KY(WO_4)_2$ crystal. *Applied Physics B: Lasers and Optics*, 86(2):287–292, 01 2007. — p.4, 46, 47, 66, 72.

[40] X. Mateos, V. Petrov, J. Liu, M.C. Pujol, U. Griebner, M. Aguiló, F. Díaz, M. Galan, and G. Viera. Efficient 2-µm continuous-wave laser oscillation of tm^{3+}:$KLu(WO_4)_2$. *IEEE Journal of Quantum Electronics*, 42(10):1008–1015, October 2006. — p.4, 6, 46, 47, 72.

[41] A. A. Lagatsky, F. Fusari, S. Calvez, J.A. Gupta, V.E. Kisel, N.V. Kuleshov, C.T.A. Brown, M.D. Dawson, and W. Sibbett. Passive mode locking of a Tm,Ho:$KY(WO_4)_2$ laser around 2µm. *Optics Letters*, 34(17):2587–2589, 2009. — p.4.

[42] P. Klopp, U. Griebner, V. Petrov, X. Mateos, M. A. Bursukova, M. C. Pujol, R. Sole, J. Gavalda, M. Aguilo, F. Güell, J. Massons, T. Kirilov, and F. Diaz. Laser operation of the new stoichiometric crystal $kyb(wo_4)_2$. *Applied Physics B: Lasers and Optics*, 74(2):185–189, 02 2002. — p.4.

[43] Yaroslav E. Romanyuk, Camelia N. Borca, Markus Pollnau, Simon Rivier, Valentin Petrov, and Uwe Griebner. Yb-doped $ky(wo_4)_2$ planar waveguide laser. *Optics Letters*, 31(1):53–55, 2006. — p.5, 19.

[44] D. Geskus, S. Aravazhi, E. Bernhardi, C. Grivas, S. Harkema, K. Hametner, D. Gunther, K. Worhoff, and M.Pollnau. Low-threshold, highly efficient gd^{3+}, lu^{3+} co-doped $ky(wo_4)_2$:yb^{3+} planar waveguide lasers. *Laser Physics Letters*, 6(11):800–805, 2009. — p.5, 26.

[45] C.N. Borca, V. Apostolopoulos, F. Gardillou, H.G. Limberger, M. Pollnau, and R.-P. Salathe. Buried channel waveguides in Yb-doped $KY(WO_4)_2$. *Applied Surface Science*, (253):8300–8303, 2007. — p.5.

[46] Dimitri Geskus, Jonathan D. Bradley, Shanmugam Aravazhi, Kerstin Wörhoff, and Markus Pollnau. Poor man's channel waveguide laser: $Ky(wo_4)_2$:yb. In *Conference on Lasers and Electro-Optics/Quantum Electronics and Laser Science Conference and Photonic Applications Systems Technologies*, page CTuS4. Optical Society of America, 2008. — p.5.

[47] F.M. Bain, A.A. Lagatsky, R.R. Thomson, N.D. Psaila, N.V. Kuleshov, A.K. Kar, W. Sibbett, and C.T.A. Brown. Ultrafast laser inscribed yb:$kgd(wo_4)_2$ and yb:$ky(wo_4)_2$ channel waveguide lasers. *Optics Express*, 17(25):22417–22422, 2009. — p.5.

[48] Florent Gardillou, Yaroslav E. Romanyuk, Camelia N. Borca, Rene-Paul Salathe, and Markus Pollnau. Lu, gd codoped $KY(WO_4)_2$: Yb epitaxial layers: towards integrated optics based on $KY(WO_4)_2$. *Optics Letters*, 32(5):488–490, March 2007. — p.5, 19.

[49] D. Geskus, S. Aravazhi, C. Grivas, K. Wörhoff, and M. Pollnau. Microstructured $ky(wo_4)_2$:gd^{3+}, lu^{3+}, yb^{3+} channel waveguide laser. *Optics Express*, 18(9):8853–8858,

April 2010. — p.6, 67.

[50] Dimitri Geskus, Shanmugam Aravazhi, Kerstin Wörhoff, and Markus Pollnau. High-power, broadly tunable, and low-quantum-defect $kgd_{1-x}lu_x(wo_4)_2$:yb^{3+} channel waveguide lasers. *Optics Express*, 18(25):26107–26112, Dec 2010. — p.6.

[51] D. Geskus, E. H. Bernhardi, K. van Dalfsen, S. Aravazhi, and M. Pollnau. Highly efficient yb^{3+}-doped channel waveguide laser at 981 nm. *Optics Express*, 21(11):13773–13778, Jun 2013. — p.6, 52, 66.

[52] S. Aravazhi, D. Geskus, K. van Dalfsen, S. A. Vázquez-Córdova, C. Grivas, U. Griebner, S. M. García-Blanco, and M. Pollnau. Engineering lattice matching, doping level, and optical properties of $ky(wo_4)_2$:gd, lu, yb layers for a cladding-side-pumped channel waveguide laser. *Applied Physics B*, 111(3):433–446, May 2013. — p.6, 21.

[53] Western Bolaños, Joan J. Carvajal, Xavier Mateos, Ganapathy Senthil Murugan, Ananth Z. Subramanian, James S. Wilkinson, Eugenio Cantelar, Daniel Jaque, Ginés Lifante, Magdalena Aguiló, and Francisco Díaz. Mirrorless buried waveguide laser in monoclinic double tungstates fabricated by a novel combination of ion milling and liquid phase epitaxy. *Optics Express*, 18(26):26937–26945, Dec 2010. — p.6, 7, 64.

[54] S. V. Borisov and R. F. Klevtsova. Crystal structure of $KY(WO_4)_2$. *Soviet Physics, Crystallography*, 13:420–421, 1968. — p.6.

[55] Alexander A. Kaminskii, Ludmila Li, Andre V. Butashin, Vladimir S. Mironov, Alexsei A. Pavlyuk, Sergei N. Bagayev, and Ken ichi Ueda. New stimulated emission channels of pr^{3+} and tm^{3+} ions in monoclinic $kr(wo_4)_2$ type crystals with ordered structure (r=y and gd). *Japanese Journal of Applied Physics*, 36(Part 2, No. 2A):L107–L109, 1997. — p.6.

[56] S.N. Bagaev, S.M. Vatnik, A.P. Maiorov, A.A. Pavlyuk, and D.V. Plakushchev. The spectroscopy and lasing of monoclinic $tm:ky(wo_4)_2$ crystals. *Quantum Electronics*, 30(4):310–314, 2000. — p.6, 52, 53, 72.

[57] L. E. Batay, A. N. Kuzmin, A. S. Grabtchikov, V. A. Lisinetskii, V. A. Orlovich, A. A. Demidovich, A. N. Titov, V. V. Badikov, S. G. Sheina, V. L. Panyutin, M. Mond, and S. Kück. Efficient diode-pumped passively q-switched laser operation around 1.9 mu m and self-frequency raman conversion of tm-doped $ky(wo_4)_2$. *Applied Physics Letters*, 81(16):2926–2928, 2002. — p.6.

[58] V. Petrov, F. Guell, J. Massons, J. Gavalda, R.M. Sole, M. Aguilo, F. Diaz, and U. Griebner. Efficient tunable laser operation of $tm:kgd(wo_4)_2$ in the continuous-wave regime at room temperature. *IEEE Journal of Quantum Electronics*, 40(9):1244–1251, Sept. 2004. — p.6, 46, 47.

[59] Jianfeng Wu, Zhidong Yao, Jie Zong, and Shibin Jiang. Highly efficient high-power thulium-doped germanate glass fiber laser. *Optics Letters*, 32(6):638–640, Mar 2007. — p.6.

[60] Stuart D. Jackson. Cross relaxation and energy transfer upconversion processes relevant to the functioning of 2 m tm3+-doped silica fibre lasers. *Optics Communications*, 230(1–3):197–203, 1 2004. — p.6, 42.

[61] D. Y. Shen, A. Abdolvand, L. J. Cooper, and W. A. Clarkson. Efficient ho : Yag

laser pumped by a cladding-pumped tunable tm : silica-fibre laser. *Applied Physics B*, 79(5):559–561, 2004. — p.6.

[62] W. L. Gao, J. Ma, G. Q. Xie, J. Zhang, D. W. Luo, H. Yang, D. Y. Tang, J. Ma, P. Yuan, and L. J. Qian. Highly efficient 2μm tm:yag ceramic laser. *Optics Letters*, 37(6):1076–1078, Mar 2012. — p.6.

[63] Maxim Gaponenko, Nikolay Kuleshov, and Thomas Südmeyer. Efficient diode-pumped tm:kyw 1.9-µm microchip laser with 1 w cw output power. *Optics Express*, 22(10):11578–11582, May 2014. — p.6.

[64] Josep Maria Serres, Xavier Mateos, Pavel Loiko, Konstantin Yumashev, Nikolai Kuleshov, Valentin Petrov, Uwe Griebner, Magdalena Aguiló, and Francesc Díaz. Diode-pumped microchip tm:klu$(wo_4)_2$ laser with more than 3 w of output power. *Optics Letters*, 39(14):4247–4250, Jul 2014. — p.6.

[65] P. Loiko, J. M. Serres, X. Mateos, K. Yumashev, N. Kuleshov, V. Petrov, U. Griebner, M. Aguiló, and F. Díaz. In-band-pumped ho:klu$(wo_4)_2$ microchip laser with 84% slope efficiency. *Optics Letters*, 40(3):344–347, Feb 2015. — p.6.

[66] P. Loiko, X. Mateos, S. Y. Choi, F. Rotermund, J. M. Serres, M. Aguiló, F. Díaz, K. Yumashev, U. Griebner, and V. Petrov. Vibronic thulium laser at 2131 nm q-switched by single-walled carbon nanotubes. *Journal of the Optical Society of America B*, 33(11):D19–D27, 2016. — p.6.

[67] M. Gaponenko, N. Kuleshov, and T. Südmeyer. Passively q-switched thulium microchip laser. *IEEE Photonics Technology Letters*, 28(2):147–150, 2016. — p.7.

[68] D. P. Shepherd, D. J. B. Brinck, J. Wang, A. C. Tropper, D. C. Hanna, G. Kakarantzas, and P. D. Townsend. 1.9-µm operation of a tm:lead germanate glass waveguide laser. *Optics Letters*, 19(13):954–956, Jul 1994. — p.7.

[69] S. Rivier, X. Mateos, V. Petrov, U. Griebner, Y. E. Romanyuk, C. N. Borca, F. Gardillou, and M. Pollnau. Tm:ky$(wo_4)_2$ waveguide laser. *Optics Express*, 15(9):5885–5892, 2007. — p.7, 64.

[70] A. Rameix, C. Borel, B. Chambaz, B. Ferrand, D. P. Shepherd, T. J. Warburton, D. C. Hanna, and A. C. Tropper. An efficient, diode-pumped, 2 [mu]m tm:yag waveguide laser. *Optics Communications*, 142(4-6):239 – 243, October 1997. — p.7.

[71] J.I. Mackenzie, S.C. Mitchell, R.J. Beach, H.E. Meissner, and D.P. Shepherd. 15 w diode-side-pumped tm:yag waveguide laser at 2 mu;m. *Electronics Letters*, 37(14):898 –899, July 2001. — p.7.

[72] Western Bolaños, Florent Starecki, Abdelmjid Benayad, Gurvan Brasse, Vivien Ménard, Jean-Louis Doualan, Alain Braud, Richard Moncorgé, and Patrice Camy. Tm:liyf4 planar waveguide laser at 1.9 µm. *Optics Letters*, 37(19):4032–4034, Oct 2012. — p.7.

[73] E. Cantelar, J. A. Sanz-Garcia, G. Lifante, F. Cusso, and P. L. Pernas. Single polarized tm^{3+} laser in zn-diffused $linbo_3$ channel waveguides. *Applied Physics Letters*, 86(16):161119, 2005. — p.7.

[74] Amol Choudhary, Pradeesh Kannan, Jacob I. Mackenzie, Xian Feng, and David P. Shepherd. Ion-exchanged tm^{3+}:glass channel waveguide laser. *Optics Letters*, 38(7):1146–1148, Apr 2013. — p.7.

[75] D. G. Lancaster, S. Gross, A. Fuerbach, H. Ebendorff Heidepriem, T. M. Monro, and M. J. Withford. Versatile large-mode-area femtosecond laser-written tm:zblan glass chip lasers. *Optics Express*, 20(25):27503–27509, Dec 2012. — p.7.

[76] S.A. Payne, L.L. Chase, L.K. Smith, W.L. Kway, and W.F. Krupke. Infrared cross-section measurements for crystals doped with er^{3+}, tm^{3+}, and ho^{3+}. *IEEE Journal of Quantum Electronics*, 28(11):2619–2630, Nov 1992. — p.7.

[77] A.A. Lagatsky, F. Fusari, S.V. Kurilchik, V.E. Kisel, A.S. Yasukevich, N. V. Kuleshov, A.A. Pavlyuk, C.T.A. Brown, and W. Sibbett. Optical spectroscopy and efficient continuous-wave operation near 2 μm for a Tm,Ho:KYW laser crystal. *Applied Physics B*, 2009. — p.8.

[78] K. Scholle, S. Lamrini, P. Koopmann, and P. Fuhrberg. *2μm Laser Sources and Their Possible Applications, Frontiers in Guided Wave Optics and Optoelectronics*. InTech, February 2010. — p.8.

[79] K Scholle, E Heumann, and G Huber. Single mode tm and tm,ho:luag lasers for lidar applications. *Laser Physics Letters*, 1(6):285, 2004. — p.8.

[80] Terence H. Risby and Frank K. Tittel. Current status of midinfrared quantum and interband cascade lasers for clinical breath analysis. *Optical Engineering*, 49(11):111123, 2010. — p.8.

[81] Björn Timmer, Wouter Olthuis, and Albert van den Berg. Ammonia sensors and their applications–a review. *Sensors and Actuators B: Chemical*, 107(2):666 – 677, 2005. — p.8.

[82] Jane Hodgkinson and Ralph P Tatam. Optical gas sensing: a review. *Measurement Science and Technology*, 24(1):012004, 2013. — p.8.

[83] L.R. Narasimhan, William Goodman, C. Patel, and N. Kumar. Correlation of breath ammonia with blood urea nitrogen and creatinine during hemodialysis. *Proceedings of the National Academy of Sciences of the United States of America*, 98(8):4617–4621, 04 2001. — p.8.

[84] DavidJ. Kearney, Todd Hubbard, and David Putnam. Breath ammonia measurement in helicobacter pylori infection. *Digestive Diseases and Sciences*, 47(11):2523–2530, 2002. — p.8.

[85] D. D. Arslanov, M. Spunei, J. Mandon, S.M. Cristescu, S.T. Persijn, and F.J.M. Harren. Continuous-wave optical parametric oscillator based infrared spectroscopy for sensitive molecular gas sensing. *Laser and Photonics Reviews*, pages 188–206, 2012. — p.9.

[86] Denis D. Arslanov, Koen Swinkels, Simona M. Cristescu, and Frans J. M. Harren. Real-time, subsecond, multicomponent breath analysis by optical parametric oscillator based off-axis integrated cavity output spectroscopy. *Optics Express*, 19(24):24078–24089, Nov 2011. — p.9.

[87] K. Krzempek, R. Lewicki, L. Nähle, M. Fischer, J. Koeth, S. Belahsene, Y. Rouillard, L. Worschech, and F. K. Tittel. Continuous wave, distributed feedback diode laser based sensor for trace-gas detection of ethane. *Applied Physics B*, 106(2):251–255, 2012. — p.9.

[88] Matthias Fill, Pierluigi Debernardi, Ferdinand Felder, and Hans Zogg. Lead-chalcogenide mid-infrared vertical external cavity surface emitting lasers with improved threshold:

Theory and experiment. *Applied Physics Letters*, 103(20):201120, 2013. — p.9.

[89] William W. Bewley, Chadwick L. Canedy, Chul Soo Kim, Mijin Kim, Charles D. Merritt, Joshua Abell, Igor Vurgaftman, and Jerry R. Meyer. High-power room-temperature continuous-wave mid-infrared interband cascade lasers. *Optics Express*, 20(19):20894–20901, Sep 2012. — p.9.

[90] J.-P. Besson, S. Schilt, E. Rochat, and L. Thévenaz. Ammonia trace measurements at ppb level based on near-ir photoacoustic spectroscopy. *Applied Physics B: Lasers and Optics*, 85:323–328, 2006. — p.9.

[91] Michael E. Webber, Michael Pushkarsky, and C. Kumar N. Patel. Fiber-amplifier-enhanced photoacoustic spectroscopy with near-infrared tunable diode lasers. *Applied Optics*, 42(12):2119–2126, Apr 2003. — p.9.

[92] Duarte Viveiros, João Ferreira, SusanaO. Silva, Joana Ribeiro, Deolinda Flores, JoséL. Santos, Orlando Frazão, and JoséM. Baptista. Ammonia sensing system based on wavelength modulation spectroscopy. *Photonic Sensors*, 5(2):109–115, 2015. — p.9.

[93] Yabai He, Ruifeng Kan, Florian V. Englich, Wenqing Liu, and Brian J. Orr. Simultaneous multi-laser, multi-species trace-level sensing of gas mixtures by rapidly swept continuous-wave cavity-ringdown spectroscopy. *Optics Express*, 18(19):20059–20071, Sep 2010. — p.9.

[94] J. Wang, W. Zhang, L. Li, and Q. Yu. Breath ammonia detection based on tunable fiber laser photoacoustic spectroscopy. *Applied Physics B: Lasers and Optics*, pages 1–7, April 2011. 10.1007/s00340-011-4550-z. — p.9.

[95] Michael E. Webber, Ricardo Claps, Florian V. Englich, Frank K. Tittel, Jay B. Jeffries, and Ronald K. Hanson. Measurements of nh_3 and co_2 with distributed-feedback diode lasers near 2.0 µm in bioreactor vent gases. *Applied Optics*, 40(24):4395–4403, Aug 2001. — p.9.

[96] G. Rieker, J. Jeffries, and R. Hanson. Measurements of high-pressure co_2 absorption near 2.0 m and implications on tunable diode laser sensor design. *Applied Physics B: Lasers and Optics*, 94:51–63, 2009. — p.9.

[97] S. N. Andreev, E. S. Mironchuk, I. V. Nikolaev, V. N. Ochkin, M. V. Spiridonov, and S. N. Tskhai. High precision measurements of the $^{13}co_2/^{12}co_2$ isotope ratio at atmospheric pressure in human breath using a 2 µm diode laser. *Applied Physics B*, 104(1):73–79, 2011. — p.9.

[98] Dimitri Geskus. *Channel waveguide lasers and amplifiers in single-crystalline Ytterbium-doped potassium double tungstates*. PhD thesis, University of Twente, Enschede, The Netherlands, November 2011. — p.13, 31, 33.

[99] A.A. Kaminskii, A. Konstantinova, V. Orekhova, A. Butashin, R. Klevtsova, and A. Pavlyuk. Optical and nonlinear laser properties of the $\chi^{(3)}$-active monoclinic α-$KY(WO_4)_2$ crystals. *Crystallography Reports*, 46(4):665–672, 07 2001. — p.13, 14, 23.

[100] M.C. Pujol, X. Mateos, A. Aznar, X. Solans, S. Suri nach, J. Massons, F. Díaz, and M. Aguiló. Structural redetermination, thermal expansion and refractive indices of $KLu(WO_4)_2$. *Journal of Applied Crystallography*, 39(2):230–236, 2006. — p.13, 14, 20.

[101] M. C. Pujol, M. Rico, C. Zaldo, R. Solé, V. Nikolov, X. Solans, M. Aguiló, and F. Díaz. Crystalline structure and optical spectroscopy of er^{3+}-doped $kgd(wo_4)_2$ single crystals. *Applied Physics B: Lasers and Optics*, 68(2):187–197, 02 1999. — p.13, 14.

[102] M.C. Pujol, X. Mateos, R Solé, J. Massons, Jna. Gavalda, F. Díaz, and M Aguiló. Linear thermal expansion tensor in $kre(wo_4)_2$ (re=gd, y, er, yb) monoclinic crystals. *Mater. Sci. Forum*, 378-381:710–717, 2001. — p.20.

[103] O Silvestre, A Aznar, R Solé, M C Pujol, F Díaz, and M Aguiló. Lattice mismatch and crystal growth of monoclinic $ky_{1x}yb_x(wo_4)_2$ /$ky(wo_4)_2$ layers by liquid phase epitaxy. *Journal of Physics: Condensed Matter*, 20(22):225004, 2008. — p.20.

[104] M.C. Pujol, R Solé, J. Massons, Jna. Gavalda, X. Solans, C. Zaldo, F Díaz, and M. Aguiló. Structural study of monoclinic $kgd(wo_4)_2$ and effects of lanthanide substitution. *Journal of Applied Crystallography*, 34(1):1–6, 2001. — p.20.

[105] M T Borowiec, V P Dyakonov, K Woźniak, Ł Dobrzycki, M Berkowski, E E Zubov, E Michalski, A Szewczyk, M U Gutowska, T Zayarnyuk, and H Szymczak. Crystal structure and magnetic properties of potassium erbium double tungstate $ker(wo_4)_2$. *Journal of Physics: Condensed Matter*, 19(5):056206, 2007. — p.20.

[106] M. T. Borowiec, T. Zayarnyuk, M. C. Pujol, M. Aguiló, F. Díaz, E. E. Zubov, A. D. Prokhorov, M. Berkowski, W. Domuchowski, A. Wisniewski, R. Puzniak, J. Pietosa, V. P. Dyakonov, M. Baranski, and H. Szymczak. Magnetic properties of $kre(wo_4)_2$ (re=gd, yb, tm) single crystals. *Physica B: Condensed Matter*, 405(23):4886–4891, 12 2010. — p.20.

[107] Yaroslav E. Romanyuk. *Liquid-phase epitaxy of doped $KY(WO_4)_2$ layers for waveguide lasers*. PhD thesis, Ecole Polytechnique Federale de Lausanne, 2005. — p.20.

[108] K. H. Hellwege and A. M. Hellwege, editors. *Numerical Data and Functional Relationships in Science and Technology*, volume III/7 of *Landolt-Börnstein series*. Springer-Verlag, 1977. — p.20.

[109] L. Vegard. Die konstitution der mischkristalle und die raumfüllung der atome. *Zeitschrift für Physik*, 5(1):17–26, 1921. — p.20.

[110] R. Guerin and P. Caillet. Phases of the potassium tungstate-tungsten (vi) oxide system and their reduction by potassium vapor. *Comptes Rendus de l'Académie des sciences*, Ser. C 271:814–817, 1970. — p.24.

[111] D. Geskus, K. van Dalfsen, S. Aravazhi, K. Wörhoff, and M. Pollnau. Yb^{3+} and Tm^{3+} doped $KGd_xLu_yY_{1-x-y}(WO_4)_2$ channel waveguide lasers. In *Conference on Lasers and Electro-Optics*, volume Technical Digest, page paper CWP4, Baltimore, Maryland, May 2011. Optical Society of America. — p.32.

[112] Robert E. Lee. Microfabrication by ion-beam etching. *Journal of Vacuum Science and Technology*, 16(2):164–170, Mar 1979. — p.36.

[113] O. Auciello. Ion interaction with solids: Surface texturing, some bulk effects, and their possible applications. *Journal of Vacuum Science and Technology*, 19(4):841–867, Nov 1981. — p.36.

[114] E. R. Rose. Rare earths of the grenville sub-province ontario and quebec. *GSC Report Number 59-10. Ottawa: Geological Survey of Canada Department of Mines and Technical Surveys*, 1960. — p.39.

[115] D. Powell. Rare earth elements plentiful in ocean sediments. *ScienceNews*, July 2011. — p.39.

[116] G. H. Dieke and H. M. Crosswhite. The spectra of the doubly and triply ionized rare earths. *Applied Optics*, 2(7):675–686, 1963. — p.40.

[117] V. Petrov, M.C. Pujol, X. Mateos, O. Silvestre, S. Rivier, M. Aguiló, M. Sole, J. Liu, U. Griebner, and F Díaz. Growth and properties of $klu(wo_4)_2$, and novel ytterbium and thulium lasers based on this monoclinic crystalline host. *Laser and Photonics Reviews*, 1(2):179 – 212, May 2007. — p.41, 42, 49.

[118] D. E. McCumber. Einstein relations connecting broadband emission and absorption spectra. *Physical Review*, 136(4A):A954–A957, Nov 1964. — p.44.

[119] Robert C. Hilborn. Einstein coefficients, cross sections, f values, dipole moments, and all that. *American Journal of Physics*, 50(11):982–986, 1982. — p.44.

[120] W. Beall Fowler and D. L. Dexter. Relation between absorption and emission probabilities in luminescent centers in ionic solids. *Phys. Rev.*, 128:2154–2165, Dec 1962. — p.44.

[121] C. B. Layne, W. H. Lowdermilk, and M. J. Weber. Multiphonon relaxation of rare-earth ions in oxide glasses. *Physical Review B*, 16:10–20, Jul 1977. — p.48.

[122] Frank Träger, editor. *Springer Handbook of Lasers and Optics*. Springer New York, 2007. — p.48.

[123] G. Rustad and K. Stenersen. Modeling of laser-pumped tm and ho lasers accounting for upconversion and ground-state depletion. *IEEE Journal of Quantum Electronics*, 32(9):1645–1656, Sep 1996. — p.49, 53, 91.

[124] A. J. Silversmith, W. Lenth, and R. M. Macfarlane. Green infraredpumped erbium upconversion laser. *Applied Physics Letters*, 51(24):1977–1979, 1987. — p.50.

[125] D. A. Zubenko, M. A. Noginov, V. A. Smirnov, and I. A. Shcherbakov. Different mechanisms of nonlinear quenching of luminescence. *Physical Review B*, 55:8881–8886, Apr 1997. — p.50.

[126] Walter J. C. Grant. Role of rate equations in the theory of luminescent energy transfer. *Physical Review B*, 4:648–663, Jul 1971. — p.50.

[127] L. D. Zusman. Kinetics of luminescence damping in the hopping mechanism of quenching. *Soviet Journal of Experimental and Theoretical Physics*, 46:347, August 1977. — p.50.

[128] L. Agazzi. *Spectroscopic excitation and quenching processes in rare-earth-ion-doped Al_2O_3 and their impact on amplifier and laser performance*. PhD thesis, University of Twente, Enschede, September 2012. — p.50.

[129] Pavel Loiko and Markus Pollnau. Stochastic model of energy-transfer processes among rare-earth ions. example of al2o3:tm3+. *The Journal of Physical Chemistry C*, 120(46):26480–26489, 11 2016. — p.50.

[130] O. Svelto. *Principles of Lasers fourth edition*. Plenum Press London, 1998. — p.53, 56.

[131] W. P. Risk. Modeling of longitudinally pumped solid-state lasers exhibiting reabsorption losses. *Journal of the Optical Society of America B*, 5(7):1412–1423, 1988. — p.57, 58.

[132] Takunori Taira, William M. Tulloch, and Robert L. Byer. Modeling of quasi-three-level lasers and operation of cw yb:yag lasers. *Applied Optics*, 36(9):1867–1874, 1997. — p.57.

[133] D.C. Hanna, R.G. Smart, P.J. Suni, A.I. Ferguson, and M.W. Phillips. Measurements of fibre laser losses via relaxation oscillations. *Optics Communications*, 68(2):128 – 132, 1988. — p.59.

[134] J. R. Salcedo, J. M. Sousa, and V. V. Kuzmin. Theoretical treatment of relaxation oscillations in quasi-three-level systems. *Applied Physics B: Lasers and Optics*, 62:83–85, 1996. — p.59.

[135] Laura Agazzi, Edward H. Bernhardi, Kerstin Worhoff, and Markus Pollnau. Impact of luminescence quenching on relaxation-oscillation frequency in solid-state lasers. *Applied Physics Letters*, 100(1):011109–3, 01 2012. — p.59, 60.

[136] F. Guell, Jna. Gavalda, R. Sole, M. Aguilo, F. Diaz, M. Galan, and J. Massons. 1.48 and 1.84 µm thulium emissions in monoclinic kgd$(wo_4)_2$ single crystals. *Journal of Applied Physics*, 95(3):919–923, 2004. — p.72, 74.

[137] O. Silvestre, M. C. Pujol, M. Rico, F. Güell, M. Aguiló, and F. Díaz. Thulium doped monoclinic klu$(wo_4)_2$ single crystals: growth and spectroscopy. *Applied Physics B: Lasers and Optics*, 87(4):707–716, 06 2007. — p.74.

[138] E. W. Duczynski, G. Huber, V. G. Ostroumov, and I. A. Shcherbakov. cw double cross pumping of the $^5i_7$–$^5i_8$ laser transition in ho^{3+}doped garnets. *Applied Physics Letters*, 48(23):1562–1563, 1986. — p.75.

List of publications

Peer-reviewed journal articles

[1] K. van Dalfsen, S. Aravazhi, C. Grivas, S. M. García-Blanco, and M. Pollnau, "Thulium channel waveguide laser with 1.6 W of output power and ~80% slope efficiency," *Optics Letters* **39**, 4380 (2014).

[2] D. Geskus, E. H. Bernhardi, K. van Dalfsen, S. Aravazhi, and M. Pollnau, "Highly efficient Yb^{3+}-doped channel waveguide laser at 981 nm," *Optics Express* **21**, 13773 (2013).

[3] S. Aravazhi, D. Geskus, K. van Dalfsen, S. A. Vázquez-Córdova, C. Grivas, U. Griebner, S. M. García-Blanco, and M. Pollnau, "Engineering lattice matching, doping level, and optical properties of $KY(WO_4)_2$:Gd, Lu, Yb layers for a cladding-side-pumped channel waveguide laser," *Applied Physics B* **111**, 433 (2013).

[4] K. van Dalfsen, S. Aravazhi, C. Grivas, S. M. García-Blanco, and M. Pollnau, "Thulium channel waveguide laser in a monoclinic double tungstate with 70% slope efficiency," *Optics Letters* **37**, 887 (2012).

[5] K. van Dalfsen, S. Aravazhi, D. Geskus, K. Wörhoff, and M. Pollnau, "Efficient $KY_{1-x-y}Gd_xLu_y(WO_4)_2$:$Tm^{3+}$ channel waveguide lasers," *Optics Express* **19**, 5277 (2011).

[6] J. Yang, K. van Dalfsen, K. Wörhoff, F. Ay, and M. Pollnau, "High-gain Al_2O_3:Nd^{3+} channel waveguide amplifiers at 880 nm, 1060 nm, and 1330 nm," *Applied Physics B* **101**, 119 (2010).

Contributions to international conferences

[7] M. Pollnau, K. van Dalfsen, and P. Loiko, "Spectroscopy and highly efficient lasing in Tm-doped waveguides," *International Conference on Lasers, Applications, and Technologies*, Minsk, Belarus, paper LMB2, ***invited paper*** (2016).

[8] K. van Dalfsen, S. Aravazhi, C. Grivas, S. M. García-Blanco, and M. Pollnau, "1.84-µm thulium-doped channel waveguide laser approaching the theoretical limit of 86% slope efficiency," *International Conference on Luminescence*, Wroclaw, Poland (2014).

[9] K. van Dalfsen, S. Aravazhi, C. Grivas, S. M. García-Blanco, and M. Pollnau, "1.6-W, highly efficient laser at 2 µm in a potassium double tungstate channel waveguide," *European Conference on Integrated Optics*, Nice, France (2014).

[10] K. van Dalfsen, S. Aravazhi, C. Grivas, S. M. García-Blanco, and M. Pollnau, "Thulium-doped channel waveguide laser with 1.6 W of output power and exceeding 80% slope efficiency," *Advanced Solid-State Lasers Congress, ASSL 2013*, Paris, France (2013).

[11] K. van Dalfsen, S. Aravazhi, C. Grivas, S. M. García-Blanco, and M. Pollnau, "Thulium-doped channel waveguide laser with 1.6 W of output power and exceeding 80% slope efficiency," *Conference on Lasers and Electro-Optics Europe*, Munich, Germany, paper PD-A.4, ***post-deadline paper*** (2013).

[12] S. Aravazhi, D. Geskus, K. van Dalfsen, S. A. Vázquez-Córdova, C. Grivas, U. Griebner, S. M. García-Blanco, and M. Pollnau, "Engineering refractive index and doping level of $KY_{1-x-y-z}Gd_xLu_yYb_z(WO_4)_2$ layers for a cladding-side-pumped channel waveguide laser," *Conference on Lasers and Electro-Optics Europe*, Munich, Germany, paper CE-6.1, ***invited paper*** (2013).

[13] K. van Dalfsen, S. Aravazhi, C. Grivas, S. M. García-Blanco, and M. Pollnau, "Highly efficient channel waveguide lasers at 2 µm," *International Conference on Transparent Optical Networks*, Cartagena, Spain, ***invited paper*** (2013).

[14] K. van Dalfsen, D. Geskus, S. M. García-Blanco, and M. Pollnau, "Highly efficient channel waveguide lasers at 1 µm and 2 µm in refractive-index-engineered potassium double tungstates," *LASE: Photonics West Conference*, San Francisco, USA, paper 8599/2 (2013).

[15] M. Pollnau, K. van Dalfsen, E. H. Bernhardi, D. Geskus, K. Wörhoff, R. M. de Ridder, and S. M. García-Blanco, "Fabrication, operation, and applications of efficient dielectric waveguide lasers", *International Conference on Advanced Laser Technologies*, Thun, Switzerland, paper Tu-1B-2-IN, ***invited paper*** (2012).

[16] K. van Dalfsen, H. A. G. M. van Wolferen, M. Dijkstra, S. Aravazhi, E. H. Bernhardi, S. M. García-Blanco, and M. Pollnau, "Towards integrated channel waveguide lasers in monoclinic double tungstates", *EPS-QEOD Europhoton Conference on Solid-State, Fibre, and Waveguide Coherent Light Sources*, Stockholm, Sweden, Europhysics Conference Abstract **34C**, paper ThP.30 (2012).

[17] M. Pollnau, J. D. B. Bradley, E. H. Bernhardi, L. Agazzi, D. Geskus, K. van Dalfsen, J. Yang, A. Driessen, S. M. García-Blanco, K. Wörhoff, and R. M. de Ridder, "On-chip integrated amplifiers and lasers utilizing rare-earth-ion activation", *Nano-TR-VIII Nanoscience and Nanotechnology Congress*, Ankara, Turkey, ***plenary lecture*** (2012).

[18] M. Pollnau, D. Geskus, E. H. Bernhardi, K. van Dalfsen, K. Wörhoff, and R. M. de Ridder, "Highly efficient solid-state waveguide lasers", *Advanced Solid-State Photonics*

Conference, San Diego, USA, (Optical Society of America, Washington, DC), paper AM5A.1, ***invited paper*** (2012).

[19] K. van Dalfsen, S. Aravazhi, C. Grivas, S. M. García-Blanco, and M. Pollnau, "Thulium channel waveguide laser with 69.7% efficiency," *Conference on Advanced Solid-State Photonics*, San Diego, USA, paper AM5A.3 (2012).

[20] K. van Dalfsen, S. Aravazhi, C. Grivas, S. M. García-Blanco, and M. Pollnau, "Highly efficient $KY_{1-x-y}Gd_xLu_y(WO_4)_2$:$Tm^{3+}$ channel waveguide lasers," *Conference on Lasers and Electro-Optics: Science and Innovations*, San José, USA, paper CTu2D.5 (2012).

[21] K. van Dalfsen, S. Aravazhi, C. Grivas, S. M. García-Blanco, and M. Pollnau, "Thulium channel waveguide laser with 70% slope efficiency in a monoclinic double tungstate," *European Conference on Integrated Optics*,Sitges/Barcelona, Spain, paper 118 (2012).

[22] K. van Dalfsen, D. Geskus, F. Ay, K. Wörhoff, S. Aravazhi, and M. Pollnau, "High-power Yb- and Tm-doped double tungstate channel waveguide lasers," *International Quantum Electronics Conference and Conference on Lasers and Electro-Optics Pacific Rim*, Sydney, Australia, paper 5420-CT-4 (2011).

[23] S. M. García-Blanco, D. Geskus, K. van Dalfsen, S. Aravazhi, and M. Pollnau, "Rare-earth-ion-doped double tungstates: a promising gain material for integrated optics," *International Symposium on Modern Optics and its Applications*, Bandung, Indonesia, ***invited paper*** (2011).

[24] K. van Dalfsen, D. Geskus, F. Ay, K. Wörhoff, S. Aravazhi, and M. Pollnau, "High-power Yb- and Tm-doped double tungstate channel waveguide lasers," *International Laser Physics Workshop*, Sarajevo, Bosnia and Herzegovina, paper 4.4.4 (2011).

[25] S. M. García-Blanco, D. Geskus, K. van Dalfsen, F. Ay, S. Aravazhi, and M. Pollnau, "Monoclinic double tungstate waveguide amplifiers and microlasers," *International Conference on Transparent Optical Networks*, Stockholm, Sweden, ***invited paper*** (2011).

[26] K. van Dalfsen, S. Aravazhi, D. Geskus, K. Wörhoff, and M. Pollnau, "Efficient Tm^{3+} lasers in double tungstate channel waveguides," *International Conference on Luminescence*, Ann Arbor, United States, paper ThII2 (2011).

[27] S. Aravazhi, D. Geskus, K. van Dalfsen, D. Günther, and M. Pollnau, "Growth and characterisation of highly Yb^{3+}-doped $KY(WO_4)_2$ thin layers," *Conference on Lasers and Electro-Optics*, Baltimore, United States, paper CE3.2 (2011).

[28] D. Geskus, K. van Dalfsen, S. Aravazhi, K. Wörhoff, F. Ay, and M. Pollnau, "Yb^{3+} and Tm^{3+} doped $KGd_xLu_yY_{1-x-y}(WO_4)_2$ channel waveguide lasers," *Conference on Lasers and Electro-Optics*, Baltimore, United States, paper CWP4 (2011).

[29] K. van Dalfsen, S. Aravazhi, D. Geskus, K. Wörhoff, F. Ay, and M. Pollnau, "Efficient Gd^{3+}, Lu^{3+} co-doped $KY(WO_4)_2$:Tm^{3+} channel waveguide lasers," *Conference on Lasers and Electro-Optics Europe*, Munich, Germany, paper CA1.5 (2011).

[30] K. van Dalfsen, S. Aravazhi, D. Geskus, K. Wörhoff, F. Ay, and M. Pollnau, "Lattice matching and microstructuring of Gd^{3+}, Lu^{3+} co-doped $KY(WO_4)_2$:Tm^{3+} channel waveguide lasers," *European Workshop on Double Tungstate Lasers*, Hamburg, Germany, ***invited paper*** (2010).

[31] J. Yang, K. van Dalfsen, K. Wörhoff, F. Ay, and M. Pollnau, "High-gain Al_2O_3:Nd^{3+} integrated waveguide amplifiers, *European Materials Research Society Meeting, Symposium K: "Rare-Earth Doped Materials for Optical Based Technologies"*, Strasbourg, France, session 14, paper 4 (2010).

[32] K. van Dalfsen, J. Yang, F. Ay, K. Wörhoff, and M. Pollnau, "Nd-doped aluminium oxide integrated amplifiers at 880 nm, 1060 nm, and 1330 nm," *European Conference on Integrated Optics*, Cambridge, United Kingdom, paper ThP34 (2010).

Contributions to national conferences

[33] K. van Dalfsen, H. A. G. M. van Wolferen, M. Dijkstra, S. Aravazhi, E. H. Bernhardi, S. M. García-Blanco, and M. Pollnau, "Efficient channel waveguide lasers in monoclinic double tungstates: towards further integration with on-chip mirrors," *Annual Symposium of the IEEE Photonics Benelux Chapter*, Mons, Belgium, pp. 97-100 (2012).

[34] S. Aravazhi, D. Geskus, K. van Dalfsen, S. M. García-Blanco, and M. Pollnau, "Refractive-index engineering and diode-side-pumped lasing of a rare-earth-ion-doped channel waveguide," *Annual Symposium of the IEEE Photonics Benelux Chapter*, Mons, Belgium, pp. 215-218 (2012).

[35] K. van Dalfsen, D. Geskus, S. Aravazhi, M. Sefünç, Y. S. Yong, S. A. Vázquez-Córdova, M. Dijkstra, K. Wörhoff, S. M. García-Blanco, and M. Pollnau, "Lasers and amplifiers in double tungstate waveguide," *Annual symposium of MESA$^+$*, Enschede, The Netherlands (2012).

[36] M. Pollnau, D. Geskus, K. van Dalfsen, S. M. García-Blanco, and S. Aravazhi, "Highly efficient lasers and amplifiers in double tungstates," *Joint Annual Meeting of the Swiss Physical Society and Austrian Physical Society*, Lausanne, Switserland, paper 627 (2011).

[37] K. van Dalfsen, S. Aravazhi, D. Geskus, S. M. García-Blanco, K. Wörhoff, and M. Pollnau, "Efficient channel waveguide lasers based on thulium-doped double tungstates," *Annual Symposium of the IEEE Photonics Benelux Chapter*, Ghent, Belgium, pp. 25-28 (2011).

[38] K. van Dalfsen, E. H. Bernhardi, L. Agazzi, D. Geskus, R. M. de Ridder, S. M. García-Blanco, K. Wörhoff, and M. Pollnau, "Ultra-high-gain amplifiers, highly-efficient and ultra-narrow-linewidth lasers in waveguide geometry," *Annual Symposium of MESA*$^+$, Enschede, The Netherlands (2011).

[39] K. van Dalfsen, S. Aravazhi, D. Geskus, K. Wörhoff, and M. Pollnau, "Efficient double tungstate channel waveguide lasers at 2 µm: toward early disease detection in human breath," *Fotonica event*, Nieuwegein, The Netherlands (2011).

[40] K. van Dalfsen, J. Yang, F. Ay, K. Wörhoff, and M. Pollnau, "Neodymium-doped Al_2O_3 channel waveguide amplifiers," *Annual Symposium of the IEEE Photonics Benelux Chapter*, Brussels, Belgium, pp. 149-152 (2009).

Dankwoord

Het schrijven van de laatste pagina's van dit proefschrift is iets waar ik lang naar heb uitgezien. Deze aaneenschakeling van pagina's met technische inhoud is tot stand gekomen in een periode van acht enerverende, soms pittige, maar ook zegenrijke jaren.

After my graduation in the Integrated Optics and MicroSystems (IOMS) group in 2009 I got the opportunity to develop a microlaser in a rather new material: potassium double tungstate. A material that was unlike any of the other materials my colleagues had been using. Rather than being able to pick a sizeable wafer in the cleanroom and doing all sorts of fancy stuff with the fancy machines in the cleanroom, I soon learned that this new material was 1×1 cm^2 small, had to be 'grown' inside a liquid-phase epitaxy oven, and by the way...you could not take it in many of the cleanroom apparatus because it would likely contaminate these! Also some of the skills I had just learned on working with fibre setups were, although useful in general, not directly applicable to working with this material. Fortunately, also the benefits of this material soon came to light: it was hard to destroy even with high power from a Ti:Sa laser hitting directly on it and the gain in this material was enormous!

I would like to thank my promotor Markus Pollnau for giving me the opportunity to work on the thulium 2-µm laser development. You had the belief in me after my graduation that I could successfully work toward a Ph.D, and entrusted me with this project. During this period I have learned a lot from you on how to do research, write a good scientific story, and present the results in a good way in person at conferences. Even after my time at the University of Twente had come to an end, you took the time to work together on some additional publications and advising on my thesis.

I also would like to thank my promotor Jennifer Herek for letting me stay at the Optical Sciences (OS) group when I was working on some publications or the thesis, in early 2014, when the Integrated Optics and MicroSystems group ceased to exist and we got scattered among the different optics research groups. Also I would like to thank you for your advice during the 'home stretch' of writing this thesis.

I would like to thank the committee members of my thesis for the invested time and effort of reading this thesis and their valuable input: prof. Klaus Boller, dr. Srirang Manohar, prof. Allard Mosk, prof. Andrea Fiore and dr. Christos Grivas.

There are a few special people with whom I worked closely during my time at

IOMS: the first is Dimitri Geskus who had started the work on his ytterbium-doped potassium double tungstate lasers. You showed me patiently every aspect of optical experiments in the lab, from working with the free-space Ti-Sa setup, the butt-coupling of dielectric mirrors and of course the lapping, polishing and micro-structuring of channel waveguides. What I remember most from you is your very positive attitude, gezelligheid (yes there is no real word for that in English), and ability to produce results with the most basic tools available: a bicycle light!

I spent countless hours together in the lab with 'Abu', dr. Aravazhi, when I needed again some samples from the oven, or needed to lap and polish them. We spent a lot of time talking about many things in life: family, religion, culture, food. I really cherish these times. Thank you for your patience and the good quality samples you've produced.

When the patterning of channel waveguides became impossible in Twente because of unavailability of an etching machine, Christos Grivas was kindly willing to help out, and to invest time and effort in the etching of these samples in Southampton. I would also like to express my gratitude for your valuable input when writing up the publications. Last but not least, thank you for the helpful input on experimenting during your time in Enschede.

To my former colleagues of the IOMS group I want to say "Thank you" for your friendliness and many talks about various things. The unique thing about this group was that, apart from many Dutch staff, the majority of the students were from different countries outside The Netherlands, which was very interesting indeed. In fact, Dimitri and myself were the only Dutch students. Initially I shared my office with Jing Yang, Fehmi Civitçi, Fei Sun, and Lasse Kauppinen. Later, in our much bigger 'lab'office in Carré, pretty much everyone could fit into this one office. I remember many good discussions about lasers and physics in general with Edward Bernhardi, but even more so about life, travel, sports, and forex! (I must admit I quit forex, but here's hoping your neutral networks made you a millionaire already!) Also I would like to name the others and thank them for the nice memories: Jonathan Bradley, Feridun Ay, Imran Akça, Nur Ismail, Chaitanya Dongre, Laura Agazzi, Marcel Hoekman, Saara-Maarit Reijn, So Van Pham, Sergio Vazquez-Cordóva, Yean-Sheng Yong, Lantian Chang, and Mustafa Akin Sefunç. Also thanks to the senior staff at IOMS for the many nice discussions, whether 'on-topic' or 'off-topic': Hugo Hoekstra, René de Ridder, Manfred Hammer, Kerstin Wörhoff and of course Sonia García-Blanco who joined our group to also work on double tungstates!

A big thanks also goes to the technicians of IOMS, I think all of you have in some way contributed to the work in this thesis, but apart from work we regularly had nice talks at the coffee table or in the laboratories: Anton Hollink (in remembrance), Meindert Dijkstra, Gabriel Sengo and Henk van Wolferen. Meindert, Gabriel, and Henk: many thanks for thinking along and spending

time with me in the cleanroom on the grating work. I also want to say thanks to Karen Munnink from the OS group for the help with the many documents to be made ready for the thesis defence, and for arranging access to the university network.

In 2014 begon ik mijn baan bij BDR Thermea, in het lab bij Remeha. Hoewel natuurlijk niet rechtstreeks betrokken bij dit proefschift merkte ik wel snel dat er belangstelling van mijn nieuwe collega's was voor mijn onderwerp, en natuurlijk "wanneer het nou eens af zou zijn". Ik wil dan ook aan aantal van mijn huidige collega's bedanken voor hun getoonde interesse en daardoor ook hun aanmoediging: Klaas Ophoff, Gerrit Jan, Evert, Sander, Sibrecht, Han, Emiel, Jelmer, Michiel, Erik-Jan en Jöran. In het bijzonder wil ik mijn huidig leidinggevende, Dirk-Jan bedanken voor zijn begrip en soepelheid, bijv. toen ik eind 2016 opeens wel erg veel dagen begon vrij te nemen terwijl er nog heel veel werk te doen was.

Een speciale vermelding is er natuurlijk voor mijn ouders, Ben en Jennie, voor hun liefde en niet-aflatende belangstelling voor alles, en ook zeker dit proefschrift. Jullie hadden een druk jaar en hoewel de afstand naar Apeldoorn groot is in combinatie met het gezin, bredere familie en natuurlijk het bedrijf, hebben jullie toch vaak voor ons klaargestaan, binnen en buiten de verbouwing. Mijn schoonouders Frans en Margreeth moeten in één adem genoemd worden op deze plek: wat hebben jullie om Esther, mijzelf en de kinderen heengestaan tijdens dit lange schrijfproces, en met name in het afgelopen jaar tijdens de hele zware renovatie van ons huis, de geboorte van ons derde kind en de 'normale dingen' daar nog bij. Frans, ongelooflijk hoe je telkens, echt letterlijk elke zaterdag, je tijd opofferde om mij 'uit de brand' te helpen tijdens de verbouwing: wat hebben we veel tijd met z'n tweeën in dat huis doorgebracht en telkens zag je het zitten! Mijn (schoon-)broers/zussen wil ik ook van harte bedanken voor de belangstelling en de hulp die we hebben ervaren.

Ik heb niet genoeg woordenschat om mijn lieve vrouw Esther te bedanken. We zijn samen gezegend met drie prachtige kinderen. En ik ben gezegend met jullie allemaal. Jij hebt van meest dichtbij het hele schrijfproces meegemaakt. Ik denk dat het jou minimaal net zoveel energie heeft gekost als mijzelf, bijvoorbeeld denkend aan al die avonduren, vrije- en vakantiedagen die hiervoor opgeofferd werden terwijl jij het gezin draaide. Zonder jou had ik dit niet kunnen doen. Ik hou van je!

De laatste regels van dit proefschrift wil ik gebruiken om mijn Schepper, de Heere God te bedanken, Die ook deze wondere wereld heeft gemaakt. Ik heb er een klein stukje van mogen onderzoeken, terwijl Hij mij gezondheid, inzicht, en doorzettingsvermogen gaf. Het aantal vragen is niet minder geworden, maar het uitzicht is adembenemend!

Marko K. van Dalfsen
Apeldoorn, februari 2017